POLITECNICO DI MILANO

Physics Department

PhD School in Physics

Cycle XXX

Comb-Assisted Cavity-Enhanced Molecular Spectroscopy at High Precision and Sensitivity

---

Supervisor: Dr. Davide GATTI

Tutor: Prof. Marco MARANGONI

The Chair of the Doctoral Program: Prof. Paola TARONI

Doctoral Dissertation of:

Riccardo GOTTI

February 2018

Abstract

The thesis focuses on the development and application of two near-infrared spectrometers operating with extreme sensitivity and precision on molecular samples in the gas phase at low pressures. The sensitivity is achieved by introducing the gas in an optical cavity with very high finesse, whereas the precision as well as an absolute calibration of the optical frequency axis is obtained by referring the probe laser to an optical frequency comb.

The first spectrometer has been developed to maximize the intra-cavity power and achieve the conditions for Doppler-free spectroscopy in a saturation regime at low pressures. Since it covers a broad range, from 1.5 to 1.63 μm, it is suitable to access a large variety of transitions for several molecules of interest. The spectrometer is based on the Pound-Drever-Hall locking of the laser to the cavity relying for the first time on a single feedback loop which employs a single sideband modulator as an ultra-fast frequency actuator. With a locking bandwidth of 5 MHz, the fluctuations of the transmitted power are reduced to less than 0.1% and the gas absorption is read out in a purely DC regime. Lamb dip acquisitions over 10 MHz, with 100 spectral points and a measurement time of 2 s per scan, have been performed with a sensitivity of $2.5{\cdot}10^{-11}$ cm^{-1} and an uncertainty on the line-centre frequency of $8{\cdot}10^{-12}$ (1.5 kHz) at 200 s (corresponding to the average of 100 spectra), comparable to the best values reported so far. The accuracy has been tested on well-studied acetylene lines of the 10100-00000 band reported by several metrological institutes, whereas the sensitivity and saturation capability have been checked on the P15e line of the 01120-00000 band, featuring a line intensity and an electric-dipole-moment among the weakest ever observed.

The second spectrometer has been developed to minimize the acquisition time and optimize the signal-to-noise ratio of Doppler broadened spectra to infer a highly accurate value of their Doppler width, and in turn of the absolute gas temperature, for Doppler-Broadening Thermometry. It is based on cavity-ring-down-spectroscopy with an innovative frequency scan procedure, exploiting the large bandwidth of an optical single sideband modulator to probe 4.2 GHz wide absorption transitions with 3200 points within a measurement lasting less than 7 s. Investigations of an isolated near-infrared line of carbon dioxide, the P12e line of the 30012-00001 band, have been performed at thermodynamic equilibrium in the pressure range from 0.5 to 7 Pa. The spectrometer has shown a state-of-the-art sensitivity of $2.1{\cdot}10^{-12}$ cm^{-1} and a frequency uncertainty on the centre-frequency of 2.1 kHz over ten minutes. A refined multiple fitting procedure applied to an ensemble of 35 spectra has allowed the determination of the gas temperature with an unprecedented level of accuracy and precision, combined in a global uncertainty of 14 parts-per-million (10^{-6}) for a measurement lasting almost 5 hours, ranking the system at the first place among optical methods.

Contents

List of Figures

List of Tables

Introduction

Motivations

Molecular absorption spectroscopy in the Near-InfraRed (Near-IR) is a powerful tool in several fields, spanning from physics and chemistry to trace gas sensing for applications such as pollution monitoring, breath analysis, industrial process control and so on.

In the majority of these fields, one of the main goals was the achievement of very high sensitivities to detect given molecular species down to the few parts per billion level or beyond. To reach those sensitivity levels on the vertical axis of the measurement, the employment of high finesse cavities, that may enhance the absorption path from their geometrical length of a few tens of centimetres to several tens of kilometres, was highly beneficial.

Inspired by the availability of high finesse cavities, several cavity based techniques have been developed, such as direct Cavity Enhanced Absorption Spectroscopy (CEAS) [1] and Continuous-Wave (CW) Cavity Ring Down Spectroscopy (CRDS) [2], which are those applied in this thesis. In CEAS a continuous wave laser is tuned to some cavity resonances and the transmitted output is recorded to probe the absorption of the sample enclosed in the cavity. CEAS measurements are strongly affected not only by the amplitude noise of the laser but also by its frequency noise due to the frequency-to-amplitude conversion given by the typically narrow profiles of the cavity resonances. Instead, in CW-CRDS a continuous wave laser is tuned to a cavity resonance and, when a build-up intensity threshold is reached, the laser is quickly switched off. This triggers an exponential decay of the transmitted light whose time constant represents the photon cavity lifetime. The latter is reduced in the presence of an absorbing medium inside the cavity and the time decay change may be exploited to infer the absorption coefficient without any need for calibration of the effective interaction length. A strength of the approach is its intrinsic immunity to the laser amplitude and frequency noise.

Before the advent of frequency combs, the frequency axis of most measurements was calibrated recurring to etalons of well-known Free-Spectral-Ranges (FSRs). In this respect, a leap forward in terms of precision, accuracy, spectral resolution and reproducibility was given nearly 20 years ago by the development of Optical Frequency Combs (OFCs). OFCs are synthesised by mode-locked lasers, invented since the 70s, which are characterised by repeated pulses as short as few optical cycles. Traditionally, pulsed lasers were used in time-resolved spectroscopy to achieve high temporal resolution, but only at the end of the 90s their spectral counterpart has been deeply investigated. Indeed in the spectral domain the phase coherence of the pulse train results in a spectrum composed of evenly spaced narrow modes, referred to as a frequency comb. Since their first implementation, frequency combs have represented a powerful spectral tool because of the reproducible structure and of the chance to stabilise it against primary microwave standards, such as Caesium clocks. This provides a link between the optical and the radio frequency domain and enables the measurement of optical frequencies, with accuracies limited only by the microwave reference.

The adoption of optical frequency combs in molecular spectroscopy, combined with the employment of high finesse cavities, has lead to the development of spectrometers with high sensitivity in the vertical axis, and high precision and accuracy on the horizontal axis of the measurements. For the first time weak transitions or even relatively strong transitions at very low pressures were probed with frequency uncertainties on the line positions reaching few parts over 10^{11}: on the one hand thanks to the enhanced absorption signal given by the cavity, on the other hand thanks to the benefit of averaging multiple spectra that shares the same comb-defined frequency axis. The low uncertainty level achieved facilitates the traceability of spectroscopic determinations as it allows the comparison of spectroscopic data recorded in different laboratories, times and conditions. Sensitivity and precision reveal highly useful also to achieve a deep physical insight on the absorption line shapes, leading to the determination of spectroscopic parameters of high metrological quality. Among those parameters, a great interest is provided by the Doppler width, which is an indicator of the thermal energy of molecules and can be exploited, for instance, for the determination of the Boltzmann constant from the accurate observation of the molecular absorption profile of a gas at thermodynamic equilibrium and at known temperature. A closely related topic, namely the realization of a primary thermometer based on Doppler-Broadened-Thermometry (DBT), makes part of the thesis activity. Other fundamental applications span from the testing of *ab-initio* quantum-mechanical calculations of the energy levels for simple light diatomic molecules [3] to the refinement of available spectroscopic databases thanks to the provided parameters of high metrological quality.

Fuelled by the previous motivations, this thesis has been focused on the development of two Comb-Assisted spectrometers characterised by high sensitivity, high precision and accuracy. A first spectrometer is based on Comb-Assisted CEAS, with an innovative tight locking of a continuous-wave laser to a high finesse cavity through the Pound-Drever-Hall technique, to be employed for the saturation of a large variety of absorption lines at pressures of few Pascal. Thanks to the use of a single sideband modulator as an ultra-fast high-dynamic-range frequency actuator, our system was the first relying on a single feedback loop to achieve a steady and efficient locking of the probe laser to the cavity. The high bandwidth of the feedback loop of about 5 MHz, one of the highest reported so far for semiconductor lasers, and the capture range of 150 MHz made the locking tight enough to quench the fluctuations of the transmitted power to less than 0.1% and to enable the read out the gas absorption in a purely DC regime with an equivalent sensitivity of about $2{\cdot}10^{-10}$ cm^{-1} Hz$^{-1/2}$. This translated into a Signal-to-Noise Ratio (SNR) of about 10000 on acetylene Lamb dips with a contrast of about 10% for a measurement lasting 200 s. The retrieved uncertainty on the line-centre frequency was $8{\cdot}10^{-12}$ (1.5 kHz), comparable to the best values reported so far. The accuracy of the spectrometer has been tested on well-known C_2H_2 lines of the 10100-00000 band, used as references in the Telecommunication band and reported by several metrological institutes [4–6], whereas the sensitivity and saturation capability have been demonstrated on the P15e line of the 01120-00000 band, featuring a line intensity below 10^{-23} cm/molecule and an electric-dipole-moment of only 5 mHz, among the weakest ever investigated.

The second spectrometer makes use of Comb-Assisted CRDS, with a novel frequency scan procedure to acquire highly dense Doppler-broadened spectra in the few Pascal pressure range with very short acquisition times. We employed the spectrometer for accurate measurements of the absorption profile of carbon-dioxide for Doppler-Broadening primary Thermometry (DBT) applications. Thanks to the combination of CW-CRDS and a cavity-dithering-locking, we developed an innovative frequency scan procedure exploting the large bandwidth of an optical Single Sideband Modulator (SSM) to probe the gas absorption over 3200 spectral points with a measurement time shorter than 7 s. Such a fast measurement enables the spectrometer to overcome any degradation due to the drifting of the experimental conditions and to reach one of the highest sensitivity level of about $4.4{\cdot}10^{-12}$ cm^{-1} at 1 s. As the probe laser frequency remains calibrated against a frequency comb during the spectral scans, our spectrometer lends itself to the acquisition of high quality spectra on both the horizontal and vertical axis of the measurements. It has been applied to the investigation of an isolated Near-IR line of carbon dioxide, the P12e line of the 30012-00001 band, at thermodynamic equilibrium in the pressure range from 0.5 to 7 Pascal, to retrieve its Doppler width and thus the absolute gas temperature. With a refined multiple fitting procedure applied to an ensemble of 35 spectra, the temperature determination reached a global uncertainty of 14 parts over 10^6 in a measurement time of almost 5 hours, which is almost a factor of two better than the best previous determination [7]. Our system ranks at the first place among optical methods and paves the way towards the optical determination of the thermodynamic temperature with a global uncertainty of 1 part over 10^6, which is an ultimate target for primary thermometry methods.

Overview of the Thesis

The thesis is organized in five chapters: Chapters 1-3 provide an introduction to the relevant fields covered by this thesis, namely molecular spectroscopy, frequency combs and cavity enhanced based techniques. Chapters 4-5 concern the specific activity of the thesis, with the design, realization and characterisation of the two spectrometers and their application to spectroscopic investigations.

The first chapter is an introduction to molecular spectroscopy, starting from the basis of light-matter interaction to the description of absorption properties of molecular gases, focusing in particular on the broadening mechanisms and on the non-linear effect of saturation. A general overview of molecular energy levels and transitions in the Near-IR, namely the rovibrational transitions, is provided at the end of the chapter.

The second chapter concerns optical frequency combs and starts with an analytical description of their operation principle and of their peculiar frequency structure. It then discusses the state of the art of frequency comb synthesisers and gives an overview on their main applications, with a specific focus on Comb-Assisted and Direct-Comb spectroscopy.

The third chapter treats in details the two groups of cavity enhanced techniques for high sensitivity measurements adopted in this thesis. Firstly it reports a description about optical cavities showing their transmission spectrum and their enhancement factor, with a particular emphasis to high finesse optical resonators. Then it gives a general overview of the techniques adopted in this thesis, namely CEAS and CRDS, also highlighting their state of the art.

The last two chapters focus on the experimental configurations of the two Comb-Assisted Near-IR spectrometers developed in this thesis. Chapter 4 describes the details of the CEAS system and shows its performances in terms of sensitivity, precision and accuracy for the spectral acquisitions of Lamb-dips of acetylene lines.

Chapter 5 regards the CRDS spectrometer. It starts with the description of the innovative acquisition procedure developed to conjugate speed, dense frequency grid and absolute frequency calibration. Then it shows the performances of the spectrometer as a Doppler-Broadened primary Thermometer over an isolated CO_2 line in the low pressure regime. Finally it reports an Allan-Werle analysis of the reproducibility of the line centre frequency determinations.

Chapter 1

Molecular Spectroscopy: an Introduction

This chapter is an introduction to the field of molecular spectroscopy and aims at giving a theoretical background to the PhD research activity. The chapter comprises four sections: the first treats the interaction of a light beam with an absorbing medium following the semi-classical approach and the density matrix formalism. The purpose is to retrieve the absorption coefficient for a two-level system and the absorption properties of molecular gases, which are the media of interest in this thesis. The second section surveys the main mechanisms leading to the broadening of absorption lines with an emphasis on the Doppler and collisional broadening. In the third section the focus is on the non-linear regime of saturation which is particularly useful to overcome the spectral resolution limit given by Doppler broadening and enhance the precision and accuracy of a spectroscopic measurement addressed to the line centre frequency. The last section describes molecular energy levels and transitions, taking into account rotational and vibrational levels excited by IR electromagnetic fields.

1.1 Light-Matter Interaction

This section deals with the interaction between an electromagnetic field of a light source and an ensemble of particles (atoms or molecules) through the semi-classical theory, with the purpose to obtain an expression of the absorption coefficient of a given medium as a function of frequency. The following discussion regards an electric dipole interaction, but the general formalism can be applied also to other kinds of transitions.

First of all, let us start from a phenomenological description. A light beam is a travelling electro-magnetic wave with an electric component represented by the expression:

$$\vec{E}(z,t) = E_0 \cos(\omega t - \vec{k} \cdot \vec{r}) \tag{1.1}$$

where ω is the frequency of the oscillation and $\vec{k} = (\omega n)/c\vec{u_z}$ is the propagation wave-vector. The mean intensity is:

$$I = \frac{1}{2}c\epsilon_0 E_0^2 \tag{1.2}$$

During light propagation through a sample of atoms or molecules, the intensity decreases according to the Lambert-Beer law [8, 9]:

$$I(z) = I_0 e^{-\alpha z} \tag{1.3}$$

where I_0 is the input intensity in W/m^2 and α is the absorption coefficient in cm^{-1}. The absorption is a frequency dependent quantity that can be written proportional to the particle concentration n (cm^{-3}) and to an effective absorption area σ (cm^2) called cross-section:

$$\alpha(\omega) = n\sigma(\omega) \tag{1.4}$$

The rigorous approach for the determination of the the absorption properties of an ensemble of particles implies the quantization of both the medium and the electromagnetic field. But a good modelling can also be obtained by the so-called semi-classical approach, which treats the particles from a quantum-mechanical point of view whereas the electromagnetic field of the light source is described by photons, that behave both as waves and particles, without specifying their quantum nature [10]. The formalism considers that the electrons of atoms or molecules can perform transitions to other energy levels in the presence of absorption or stimulated emission of a photon. Spontaneous emission and non-radiative processes are neglected and have to be added *a posteriori*. Thanks to the semi-classical approach it is possible to retrieve the transition probabilities and the population density changes induced by the interaction between the electrons in the medium and the field.

The starting point is the perturbation theory, where the effects of the interacting field are considered as perturbation terms to be added to the unperturbed condition. The electron distributions in the medium are treated with their perturbed wave-functions. They can be written in Dirac's notation as linear combinations of the wave-functions of the eigen-states in the unperturbed condition, $|\psi_n\rangle$, with time-dependent weighting factors $C_n(t)$ due to the perturbation field:

$$|\Psi(t)\rangle = \sum_n C_n(t)|\psi_n\rangle \tag{1.5}$$

The interaction between the electrons of the medium and the electromagnetic field is added as a perturbation term H' to the unperturbed Hamiltonian H_0:

$$H = H_0 + H' \tag{1.6}$$

The unperturbed Hamiltonian provides the eigen-state wave-functions $|\psi_n\rangle$ by the Schrödinger's equation [11]:

$$H_0|\psi_n\rangle = i\hbar\frac{\partial|\psi_n\rangle}{\partial t} \tag{1.7}$$

whereas the perturbation, in the weak-field approximation, can be calculated as the scalar product between the dipole moment of the medium and the electric field:

$$H' = -\vec{\mu}\cdot\vec{E} \tag{1.8}$$

The total interaction Hamiltonian is an hermitian operator, which means that it is equal to its eigen-operator $H^\dagger$ defined as

$$\langle\psi|H|\phi\rangle = \langle\phi|H^\dagger|\psi\rangle^* \tag{1.9}$$

For this kind of operators, the diagonal matrix elements are real numbers $H^\dagger_{ii} = H^*_{ii} = H_{ii}$ (related to physical observables) and the off-diagonal elements are complex conjugated $H^\dagger_{ij} = H^*_{ji} = H_{ij}$. Usually the description begins with the case of two-level systems, where the electrons of the medium perform transitions from the ground to the excited state level.

In general, two different approaches can be followed: the first is to write the rate equations of the population densities of the two levels and solve them to obtain the joint density of states in the presence of emission and absorption processes. The second is to exploit the properties of a quantum mechanical operator, the density matrix, applied to the interaction Hamiltonian. The last formalism is considered more versatile and is explained in the following subsection. For a complete treatment about this procedure the reader is referred to [10, 12].

1.1.1 Density Matrix Approach for a Two-Level System

The density matrix describes the state of a quantum mechanical system in an alternative way than the wave-function, with some practical advantages regarding the treatment of time-evolution of the system. The density matrix is defined as:

$$\rho \equiv |\Psi(t)\rangle\,\langle\Psi(t)| \tag{1.10}$$

It is possible to demonstrate that the density matrix operator is hermitian and that its trace, when applied to a physical quantity A, gives the expectation value of that quantity:

$$\langle A\rangle = Tr(\rho A) \tag{1.11}$$

Eq.(1.11) is the "bridge" between the classical point of view ($\langle A\rangle$ is a classical observable) and quantum mechanics (ρ is a quantum mechanical operator). Considering a system in a pure state characterised by a single wave-function, the quantity $\langle\psi_n|\rho|\psi_n\rangle$ represents the probability of finding the system in that particular $|\psi_n\rangle$ state. In the presence of a perturbed system described by the perturbed wave-functions $|\Psi(t)\rangle = \sum_n C_n(t)|\psi_n\rangle$, the density matrix elements are:

$$\rho_{nm} = \langle\psi_n|\rho|\psi_m\rangle = \sum \langle\psi_n|\Psi(t)\rangle\,\langle\Psi(t)|\psi_m\rangle = C_n(t)C_m^*(t) \tag{1.12}$$

where the diagonal elements $\rho_{nn} = C_nC_n^* = p_n > 0$ represent the probability of the system to be in the particular state $|\psi_n\rangle$, whereas the off-diagonal elements $\rho_{nm} = C_n(t)C_m^*(t) = C_nC_m^*e^{-i\omega_{nm}t}$ are complex and have a phase-dependent factor and describes the coherent superposition between the two states $\psi_n\rangle$ and $\psi_m\rangle$.

A fundamental property of the density matrix operator is related to its partial derivative over time $\frac{\partial\rho}{\partial t}$, which is directly proportional to the commutator of the density matrix and another operator, in our case the interaction Hamiltonian:

$$\frac{\partial\rho}{\partial t} = \frac{i}{\hbar}[H,\rho] = \frac{i}{\hbar}(H\rho - \rho H) \tag{1.13}$$

Consider now the basic case of the two levels system, with energies ε_1 and ε_2 and with a total electron population density of N. An electron transition is possible if the incoming photon possesses a frequency close to the resonance condition $\omega \approx \omega_0$ where $\omega_0 = (\varepsilon_2 - \varepsilon_1)/\hbar$. The system is supposed to be in a quasi-equilibrium situation, i.e. in a condition where both the ground-state and the excited state levels are populated. This circumstance can be obtained by pumping mechanisms, for example by electrical or optical pumping. The density matrix operator for the two-level system is:

$$\begin{pmatrix}\rho_{11} & \rho_{12}\\ \rho_{21} & \rho_{22}\end{pmatrix} \tag{1.14}$$

where $\rho_{12} = {\rho_{21}}^*$. The population of the ground state level is $N_1 = N\rho_{11}$ and of the excited state is $N_2 = N\rho_{22}$. The population density difference is then obtained as $\Delta N = N(\rho_{22} - \rho_{11})$. The interaction Hamiltonian is the sum of two contributions, the first coming from the unperturbed Hamiltonian:

$$H_0 = \begin{pmatrix}\varepsilon_1 & 0\\ 0 & \varepsilon_2\end{pmatrix} \tag{1.15}$$

and the second from the perturbation Hamiltonian:

$$H' = -\vec{\mu}\cdot\vec{E} = -\mu E = \begin{pmatrix}0 & -\mu_{12}E\\ -\mu_{21}E & 0\end{pmatrix} \tag{1.16}$$

which depends on the dipole moment that for N particles is defined as $\overrightarrow{\mu} = \sum_{i=1}^{N} q_i(\overrightarrow{r_i} - \overrightarrow{r_C})$, where q_i is the electric charge and $\overrightarrow{r_i} - \overrightarrow{r_C}$ is the distance of the i^{th}-particle from the molecular centre of mass. Since the dipole moment is an even operator, the perturbation Hamiltonian contains only the off-diagonal elements $\mu_{12}E = \mu_{21}^* E = \mu E$. By using Eq.(1.11), the expectation value of the dipole moment $\langle\mu\rangle$ results:

$$\langle\mu\rangle = Tr(\rho\mu) = \mu(\rho_{12} + \rho_{21}) = \mu(\rho_{21}^* + \rho_{21}) = 2\mu Re(\rho_{21}) \tag{1.17}$$

The term ρ_{21} regards the degree of coherence of the oscillation of the dipole moment, which translates macroscopically in the polarization $P = N\langle\mu\rangle = 2N\mu Re(\rho_{21})$.

The density matrix formalism consists in exploiting Eq.(1.13) to obtain the evolution of the matrix elements, representing the population densities of the two level and the degree of coherence of the dipole moment oscillation. The quantum mechanical commutator between the density matrix and the Hamiltonian operator is:

$$[\rho, H] = \begin{pmatrix} \rho_{11} & \rho_{21}^* \\ \rho_{21} & \rho_{22} \end{pmatrix} \begin{pmatrix} \varepsilon_1 & -\mu_{21}^* E \\ -\mu_{21}E & \varepsilon_2 \end{pmatrix} - \begin{pmatrix} \varepsilon_1 & -\mu_{21}^* E \\ -\mu_{21}E & \varepsilon_2 \end{pmatrix} \begin{pmatrix} \rho_{11} & \rho_{21}^* \\ \rho_{21} & \rho_{22} \end{pmatrix} \tag{1.18}$$

which, after some algebra, becomes:

$$\begin{pmatrix} (\rho_{21} - \rho_{21}^*)\mu E & -\rho_{21}^*(\varepsilon_1 - \varepsilon_2) - \mu E(\rho_{11} - \rho_{22}) \\ \rho_{21}^*(\varepsilon_1 - \varepsilon_2) + \mu E(\rho_{11} - \rho_{22}) & (\rho_{21}^* - \rho_{21})\mu E \end{pmatrix} \tag{1.19}$$

The previous matrix and the property of the partial derivative of ρ (Eq.(1.13)) leads to the three equations:

$$\frac{\partial\rho_{21}}{\partial t} = \frac{i}{\hbar}[\rho_{21}(\varepsilon_1 - \varepsilon_2) + \mu E(\rho_{11} - \rho_{22})] \tag{1.20}$$

$$\frac{\partial\rho_{11}}{\partial t} = \frac{i}{\hbar}\mu E(\rho_{21} - \rho_{21}^*) \tag{1.21}$$

$$\frac{\partial\rho_{22}}{\partial t} = -\frac{i}{\hbar}\mu E(\rho_{21} - \rho_{21}^*) \tag{1.22}$$

$$\tag{1.23}$$

that can be grouped in two equations and also simplified introducing $(\varepsilon_1 - \varepsilon_2) = -\hbar\omega_0$:

$$\frac{\partial\rho_{21}}{\partial t} = -i\omega_0\rho_{21} + \frac{i\mu E}{\hbar}(\rho_{11} - \rho_{22}) \tag{1.24}$$

$$\frac{\partial(\rho_{11} - \rho_{22})}{\partial t} = 2i\frac{\mu E}{\hbar}(\rho_{21} - \rho_{21}^*) \tag{1.25}$$

The first equation, when the perturbation is not present (i.e. $E = 0$), has the solution $\rho_{21}(t) = \rho_{21}(0)\exp(-i\omega_0 t)$, which means that the coherent oscillation continues indefinitely. Since this result is not physically possible because of the spontaneous decay from the excited state, a decay term

$-\rho_{21}/T$ has to be inserted *a posteriori*, where T is the time constant related to spontaneous emission events that bring the system back to the quasi-equilibrium condition. When other decay processes are present, such as collisions between particles for instance, the time constant T decreases, but in the following description let us consider the simpler case where only spontaneous emission is the cause of the loss of coherence. As a sake of simplicity, non-radiative decays are neglected. The second equation poses a similar issue since for $E = 0$ the difference in the population densities $\Delta N = N(\rho_{11} - \rho_{22})$ has to go back to the starting quasi-equilibrium condition $\Delta N_{eq} = N(\rho_{11} - \rho_{22})_{eq}$ with a time constant τ, where typically $\tau >> T$. Thus a decay term $-[(\rho_{11} - \rho_{22}) - (\rho_{11} - \rho_{22})_{eq}]/\tau$ has to be inserted in the equation.

Let us rewrite the term ρ_{21} as:

$$\rho_{21} = \sigma_{21} e^{-i\omega t} \tag{1.26}$$

where the quantity σ_{21} varies slowly with time and $e^{-i\omega t}$ represents the oscillation of the dipole moment. This is equivalent of retaining the $e^{-i\omega t}$ term only in the expression of the electric field:

$$E(t) = E_0 \cos(\omega t) = \frac{E_0}{2}(e^{i\omega t} + e^{-i\omega t}) \sim \frac{E_0}{2} e^{i\omega t} \tag{1.27}$$

Introducing the decay terms and Eq.(1.26), Eq.(1.24) and Eq.(1.25) become:

$$\frac{\partial \sigma_{21}}{\partial t} = i(\omega - \omega_0)\sigma_{21} + i\frac{\mu E_0}{2\hbar} - \frac{\sigma_{21}}{T} \tag{1.28}$$

$$\frac{\partial(\rho_{11} - \rho_{22})}{\partial t} = i\frac{\mu E_0}{\hbar}(\sigma_{21} - \sigma_{21}^*) - \frac{(\rho_{11} - \rho_{22}) - (\rho_{11} - \rho_{22})_{eq}}{\tau} \tag{1.29}$$

In the stationary condition that we are interested in, one can set $\partial(\rho_{11} - \rho_{22})/\partial t = 0$ and obtain the following system:

$$i(\omega - \omega_0)\sigma_{21} + i\frac{\mu E_0}{2\hbar} - \frac{\sigma_{21}}{T} = 0 \tag{1.30}$$

$$i\frac{\mu E_0}{\hbar}(\sigma_{21} - \sigma_{21}^*) - \frac{(\rho_{11} - \rho_{22}) - (\rho_{11} - \rho_{22})_{eq}}{\tau} = 0 \tag{1.31}$$

with solutions:

$$Re(\sigma_{21}) = \frac{\Omega T^2(\omega_0 - \omega)(\rho_{11} - \rho_{22})_{eq}}{1 + (\omega - \omega_0)^2 T^2 + \Omega^2 T\tau} \tag{1.32}$$

$$Im(\sigma_{21}) = \frac{\Omega T(\rho_{11} - \rho_{22})_{eq}}{1 + (\omega - \omega_0)^2 T^2 + 4\Omega^2 T\tau} \tag{1.33}$$

$$(\rho_{11} - \rho_{22}) = (\rho_{11} - \rho_{22})_{eq} \frac{1 + (\omega - \omega_0)^2 T^2}{1 + (\omega - \omega_0)^2 T^2 + \Omega^2 T\tau} \tag{1.34}$$

where the quantity Ω is defined as $(\mu E_0)/(\hbar)$ and is called Rabi frequency. The population difference ΔN may be then deduced as:

$$\Delta N = N(\rho_{11} - \rho_{22}) = \Delta N_{eq} \frac{1 + (\omega - \omega_0)^2 T^2}{1 + (\omega - \omega_0)^2 T^2 + \Omega^2 T \tau} \tag{1.35}$$

According to Eq.(1.17), the electric dipole moment takes the form:

$$\langle \mu \rangle = 2\mu Re(\rho_{21}) = 2\mu(Re(\sigma_{21})\cos(\omega t) + Im(\sigma_{21})\sin(\omega t)) \tag{1.36}$$

and this results in a polarization:

$$P = N\langle \mu \rangle = \frac{\mu^2 \Delta N_{eq} T}{\hbar} E_0 \frac{\sin(\omega t) + (\omega_0 - \omega) T \cos(\omega t)}{1 + (\omega - \omega_0)^2 T^2 + 4\Omega^2 T \tau} \tag{1.37}$$

P contains all the information of the interaction between the medium and the field and is also a classical physical observable. In the approximation of weak field the term $\Omega^2 \sim (\mu E_0)^2$ can be considered negligible.

Comparing Eq.(1.37) with the macroscopic definition of polarisation as a function of the linear susceptibility χ:

$$P = Re(\epsilon_0 \chi E_0 e^{i\omega t}) = Re[\epsilon_0(\chi' - i\chi'')E_0(\cos(\omega t) + i\sin(\omega t))] \tag{1.38}$$

it is possible to determine the real χ' and imaginary part χ'', in particular the first is related to dispersion effects and the second to absorption effects:

$$\chi'(\omega - \omega_0) = -\frac{\mu^2 \pi}{\epsilon_0 \hbar} T \Delta N_{eq}(\omega - \omega_0) \left\{ \frac{T}{\pi[1 + (\omega - \omega_0)^2 T^2]} \right\} \tag{1.39}$$

$$\chi''(\omega - \omega_0) = \frac{\mu^2 \pi}{\epsilon_0 \hbar} \Delta N_{eq} \left\{ \frac{T}{\pi[1 + (\omega - \omega_0)^2 T^2]} \right\} \tag{1.40}$$

The function between parenthesis is a Lorentzian function usually indicated as $g(\omega - \omega_0)$ with normalized area $(\int_{-\infty}^{+\infty} g(\omega - \omega_0) d(\omega) = 1)$. Notice that $g(\omega - \omega_0)$ acts as a source of broadening of the transition, as this can be driven also when $\omega \neq \omega_0$.

To retrieve the absorption coefficient of the medium, let us recur to the definition of the relative dielectric constant of the medium, related both to the resonant $\chi(\omega)$ and non-resonant χ_{nr} susceptibility by:

$$\epsilon_r = 1 + \chi_{nr} + \chi(\omega - \omega_0) = n^2 + \chi(\omega - \omega_0) = n^2 \left[1 + \frac{\chi(\omega - \omega_0)}{n^2}\right] = n_T^2 \tag{1.41}$$

with n being the refractive index and n_T the total refractive index. Under the assumption $\chi(\omega - \omega_0)/n^2 << 1$ the total refractive index may be approximated by $n_T = n[1 + \frac{\chi(\omega)}{2n^2}]$ and the total wave-vector, since $\omega - \omega_0 << \omega_0$ even considering all the de-phasing sources, is expressed as:

$$k_T \approx \frac{\omega_0 n_T}{c} = \frac{\omega_0 n}{c}\left[1 + \frac{\chi(\omega - \omega_0)}{2n^2}\right] = \frac{\omega n}{c}\left[1 + \frac{\chi'}{2n^2} - i\frac{\chi''}{2n^2}\right] = k' + k'' \tag{1.42}$$

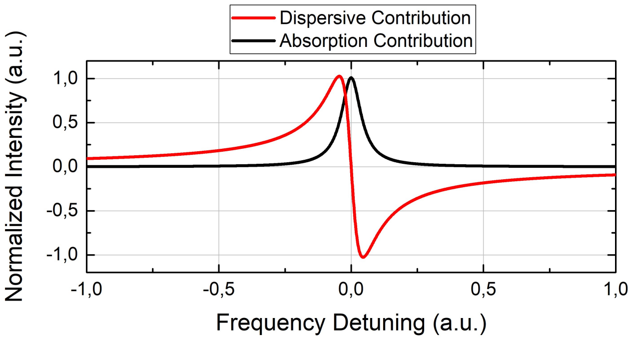

Figure 1.1: Normalized dispersion and absorption terms of the Susceptibility as a function of the frequency detuning from the resonance condition $\omega - \omega_0$. The first (red trace) is an even dispersive function whereas the second (black trace) is Lorentzian curve.

From Eq.(1.42), the electromagnetic field inside the medium after a propagation distance z may be written as:

$$E = E_0 e^{i(\omega t - k_T z)} = E_0 e^{i(\omega t - k' z)} e^{-k'' z} \tag{1.43}$$

where the term $e^{-k''z}$ accounts for an exponential decay of the field amplitude with a decay rate $\alpha = -2k''$ given by

$$\alpha(\omega - \omega_0) = k\frac{\chi''(\omega)}{n^2} = k\frac{\mu^2 \pi}{\epsilon_0 \hbar}\Delta N_{eq} g(\omega - \omega_0) = \frac{\omega_0}{c}\frac{\mu^2 \pi}{\epsilon_0 \hbar}\Delta N_{eq} g(\omega - \omega_0) \tag{1.44}$$

which depends on the square of the transition dipole moment μ^2 and the total population difference $\Delta N = \Delta N_{eq} g(\omega - \omega_0)$.

Typically the absorption coefficient is written in the form

$$\alpha(\omega - \omega_0) = \sigma(\omega - \omega_0)\Delta N_{eq} \tag{1.45}$$

where $\sigma(\omega - \omega_0)$ is called absorption cross-section, taking the role of the effective absorption area used in the phenomenological description. By doing the modulus square of $E = E_0 e^{i(\omega t - k' z)} e^{-\frac{\alpha z}{2}}$ to obtain the intensity during propagation through the medium, the Lambert-Beer law is retrieved.

$g(\omega - \omega_0)$ is an intrinsic broadening of the transition line, representing the loss of coherence between the oscillation of the dipole moment and the electromagnetic field due to spontaneous emission, called Natural broadening. When other mechanisms are present, $g(\omega - \omega_0)$ comprises them resulting in a broader profile, as shown in the next subsection.

1.1.2 Absorption Strengths of Molecular Gases

The following subsection treats the absorption properties of molecular gases, explaining the relevant parameters related to their absorption line intensity.

Considering a transition between two levels of a molecular gas sample, the absorption coefficient is usually written taking into account the molecular density n expressed in molecules/cm^3, the line strength S in cm/molecules and the normalized line-shape function $g(\omega - \omega_0)$ in cm:

$$\alpha(\omega - \omega_0) = nSg(\omega - \omega_0) \tag{1.46}$$

Equation (1.46) can be easily related to (1.44), indeed the difference in the population density of electrons ΔN is proportional to the density of molecules n, as it is going to be shown below, the line strength S is the intensity of the spectrum including all the transition parameters and the normalized line-shape profile $g(\omega - \omega_0)$ which accounts for all the broadening mechanisms.

The electron population density of the i-energy level at equilibrium is expressed through the Boltzmann distribution:

$$N_i = p_i(T) n e^{-\frac{\varepsilon_i}{k_B T}} \tag{1.47}$$

where T is the sample temperature and $p_i(T)$ is a statistical weight of the ensemble partition function at the temperature T, as discussed in Refs. [13, 14]. The focus in this thesis is to point out the direct proportionality between N_i and n. From Eq.(1.47), the difference in the population densities of a two level system is:

$$\Delta N = n \left[p_1(T) e^{-\frac{\varepsilon_1}{k_B T}} - p_2(T) e^{-\frac{\varepsilon_2}{k_B T}} \right] = n f(T) \tag{1.48}$$

The line strength S is a fundamental parameter of the transition. It contains the function $f(T)$ present in Eq.(1.48), which means that it is temperature dependent, and include all the informations about the transition (photon energy required, if it is an electric-dipole or electric-quadrupole transition and so on). Without describing the full analytical procedure, reported elsewhere [15], a complete expression of the line strength is deduced from the rate equations of the population densities introducing the Einstein A_{21} coefficient:

$$S = A_{21} \frac{\pi p_2(T)}{2c\omega_0^2} e^{\frac{hc\varepsilon_1}{k_B T}} \left[1 - e^{\frac{\hbar c \omega_0}{k_B T}} \right] \tag{1.49}$$

The use of the Einstein A coefficient in the expression for the line strength gives independence from the type of transition, electric-dipole, magnetic-dipole or electric quadrupole. In particular, since the spectroscopic investigations presented in this thesis regards electric-dipole transitions, it is useful to write the explicit dependence of μ_{21} as a function of the Einstein A coefficient:

$$\mu_{21} = \sqrt{\frac{A_{21} 3\epsilon_0 h c^3}{2\omega_0^3}} \tag{1.50}$$

In the HITRAN database, line strength coefficients are tabulated for different molecules and isotopes for T =296 K. If the experimental temperature deviates from the standard value, a conversion formula exists to retrieve S at a specific T [15]. An experimental way to determine the line strength consists in the integration of the absorption coefficient to obtain the integrated absorption *Area* (defined as the area below the absorption curve) and dividing the value by the molecular density:

$$S = \frac{\int_{-\infty}^{+\infty} \alpha(\omega - \omega_0) d\omega}{n} = \frac{Area}{n} \tag{1.51}$$

As said before, the last term of Eq.(1.46) is the function $g(\omega - \omega_0)$ which takes in account all the broadening mechanisms causing a deviation from the δ-function of the line-shape as stated before and is going to be treated in details below.

1.2 Line Broadening Mechanisms

The section regards some of the physical mechanisms regarding the broadening of the absorption line-shapes of gaseous samples. Broadening mechanisms are divided in two classes: homogeneous mechanisms which enlarges the width of the line-shape of every atom or molecule of the ensemble in the same way and are characterised by a Lorentzian line-shape, and inhomogeneous mechanisms which distributes the effective resonance frequencies of the ensemble around a centring value ω_0 represented by Gaussian functions. These mechanisms are treated in detail in the following subsections.

1.2.1 Homogeneous Broadening Mechanisms

Eqs.(1.44) and (1.46) of Section 1.1 comprise the Natural broadening of the absorption spectrum due to spontaneous decays of an excited state. These events causes a loss of coherence between the oscillations of the dipole moments and the interacting external field.

Natural broadening can be understood considering the model of a dumped oscillator. A dumped oscillator is represented by the differential equation:

$$\frac{d^2x}{dt^2} + \frac{1}{T}\frac{dx}{dt} + \omega_0^2 x = 0 \tag{1.52}$$

where T is the decay time constant called natural lifetime. The previous equation admits the solution:

$$x(t) = x_0 \cos(\omega_0 t + \varphi_0) e^{-\frac{1}{T}} \tag{1.53}$$

where x_0 and φ_0 are the starting position and the phase. The Fourier transform of Eq.(1.53) is not a δ-peak but a broadened profile with a Lorentzian shape centred at ω_0 represented by the term:

$$g(\omega - \omega_0) = \frac{T}{\pi[1 + (\omega - \omega_0)^2 T^2]} \tag{1.54}$$

with Full Width at Half Maximum (FWHM) equal to $\Delta\omega = \dfrac{1}{T}$ or $\Delta\nu = \dfrac{1}{2\pi T}$ converted in regular frequencies. Natural broadening affects the line-shape of every atom or molecule of the ensemble in the same way and places an insurmountable lower limit to the spectral linewidth.

A second homogeneous broadening mechanism comes from elastic collisions between atoms or molecules of the ensemble, called Collisional or Pressure broadening. An analytical treatment of Collisional broadening assumes that collisions happens at time instants $t_1, t_2, t_3, ...$ spaced by intervals of duration τ. τ is an aleatory variable with expected value τ_c and probability distribution $\frac{1}{\tau_c}\exp\left(-\frac{\tau}{\tau_c}\right)$. The collisions are supposed to be elastic, which means that after every collision the transition probability undergoes random phase jumps. Under the previous assumptions, the interaction between the electric field and the colliding molecules is equivalent to the interaction with a monochromatic field that undergoes random phase jumps with an ensemble where no collisions are present. In this case the electric field has a phase that varies randomly at every τ interval:

$$E(t) = E_0 \cos(\omega_0 t + \varphi(t)) = \frac{E_0}{2}\left(e^{i\omega_0 t + \varphi(t)} + e^{-i\omega_0 t + \varphi(t)}\right) \tag{1.55}$$

In particular $\varphi(t)$ is a constant function within the time intervals where no collisions happen. The mean time between collisions τ_c can be obtained using the simple model of the kinetic theory of a gases where atoms and molecules are represented by rigid spheres with a certain mass m and radius r. For a particular temperature T and pressure p, τ_c is:

$$\tau_c = \frac{\sqrt{m k_B T}}{16\sqrt{\pi} a^2 p} \tag{1.56}$$

The other fundamental effect of collisions is associated with a shift $\delta\omega$ of the absorption distribution with respect to the the central value ω_0. This change in the observed centre frequency can be explained in terms of the inter-particle interaction, indeed two moving molecules are affected by their electrons distributions and their energy levels shift accordingly to the molecular distance [16].

The broadening function $g(\omega - \omega_0)$ deduced in this situation, with the density matrix formalism for instance, is the convolution of two Lorentzian contributions: the first coming from the natural lifetime (with FWHM $\gamma_n = 1/T$) and the second from collisions (with FWHM $\gamma_c = 2/\tau_c$). As a consequence, the spectral profile in the presence of both natural and has the following expression:

$$g(\omega-\omega_0)=\frac{\left(\frac{\gamma_n}{2}+\frac{\gamma_c}{2}\right)^2}{\pi\left[\left(\frac{\gamma_n}{2}+\frac{\gamma_c}{2}\right)^2+(\omega-\omega_0+\delta\omega)^2\right]} \tag{1.57}$$

It is important to point out that the self-broadened collisional linewidth FWHM$_c$=$1/\tau_c$ is directly proportional to the gas pressure by means of a constant, called C_p [17], and for every molecular sample it can be written as $\gamma_c = C_p p$. A reduction of the self-induced collisional broadening thus can be controllable regulating the sample pressure p. Collisional broadening of molecular samples typically makes negligible the Natural broadening.

A third homogeneous broadening is caused by particle collisions with the wall of the containing cell, called Wall-collision broadening. This broadening is analysed with the kinetic theory of gases and the Maxwell-Boltzmann distribution of the molecular speed. It can be demonstrated that the FWHM of the function $g(\omega-\omega_0)$ increases by the factor:

$$\gamma_w=\frac{\bar{v}}{2\pi D} \tag{1.58}$$

where $\bar{v}=\sqrt{\frac{8k_BT}{\pi m}}$ is the averaged speed and D is the cell diameter. This broadening can be controlled easily since it is inversely proportional to the diameter D.

The last broadening mechanism usually included in the homogeneous class is due to the finite interaction time of molecules and the light beam, called Transit-time broadening. If the spontaneous lifetime T of a transition is longer than $\tau_t=\frac{a}{\bar{v}}$ (a being the beam diameter) which is the time of the interaction between moving molecules and the light beam, the transition linewidth is increased because of the fundamental indetermination law between energy (and thus frequency) and time. The transit time effect can be represented by an electric field oscillation that suddenly stops when interacting with the molecular sample with a resulting FWHM of [12]:

$$\gamma_t=\frac{\bar{v}}{2\pi a} \tag{1.59}$$

It has to be noticed that the Transit-time broadening is an homogeneous broadening mechanism with a Lorentzian shape only at a first order approximation, i.e. when the velocity distribution may be assumed peaked around the mean value and the interacting beam is simplified with a planar wave front. When the curvature of the phase front of the light beam and the Maxwell-Boltzmann velocity distribution are taken into account, the Transit-time broadening is inhomogeneous and characterised by an asymmetric and distorted Lorentzian shape [18]. Indeed molecules have different interaction times with the beam depending on their velocity distribution, in particular with its absolute value and direction. This fact has been treated deeply since the 1970's, the interested reader can refers to the paper of Bordé *et al.* [18].

1.2.2 Inhomogeneous Broadening: The Doppler Broadening

The main broadening mechanism limiting the resolution of spectroscopic measurements when treating gas samples is caused by the thermal motions of the particles, called the Doppler broadening.

The Doppler broadening is an inhomogeneous broadening mechanism that acts differently from molecule to molecule and is a function of the temperature T. Other inhomogeneous mechanisms are present in general, but in the gas phase they can be neglected and only the Doppler broadening remains as the dominant inhomogeneous process. The Doppler broadening effect regards molecules that possess a kinetic energy when interacting with the electric field.

Consider for example an electric field propagating in the z-direction of a three-dimensional space with an angular frequency ω. If a molecule is moving in the same direction of the propagating field, it experiences a different angular frequency ω' given by the relation:

$$\omega' = \omega\left(1 - \frac{v_z}{c}\right) \tag{1.60}$$

where c is the speed of light and the molecular velocity $v_z << c$. For a two-level system, this implies that absorption occurs when $\omega' = \omega_0$ leading to an effective transition angular frequency ω_0' expressed as:

$$\omega_0' = \frac{\omega_0}{\left(1 - \frac{v_z}{c}\right)} \approx \omega_0\left(1 + \frac{v_z}{c}\right) \tag{1.61}$$

which means that the particle has a shifted resonance condition from $\omega_0 = (E_2 - E_1)/\hbar$ due to its velocity.

Treating all molecules of the ensemble, the probability distribution of the velocity component v_z for a gas at thermodynamic equilibrium is:

$$f(v_z) = \sqrt{\frac{m}{2\pi k_B T}} e^{-\frac{mv_z^2}{2k_B T}} \tag{1.62}$$

The density of particles at a velocity comprised between v_z and $v_z + dv_z$ is expressed by:

$$dN(v_z) = Nf(v_z)dv_z \tag{1.63}$$

where N is the total molecular density, and the resonance frequency of those atoms is in the interval $\omega_0', \omega_0' + d\omega_0'$ being $d\omega_0' = \frac{\omega_0}{c}dv_z$. $dN(v_z)$ can be expressed then as:

$$dN(v_z) = Ng^*(\omega_o' - \omega_0)d\omega_0' \tag{1.64}$$

where $g^*(\omega_o' - \omega_0)$ is is the Doppler broadening line-shape function:

$$g^*(\omega_o' - \omega_0) = \frac{dv_z}{d\omega_0'} f(v_z) = \frac{c}{\omega_0}\sqrt{\frac{m}{2\pi k_B T}} e^{-\frac{mc^2(\omega_0'-\omega_0)^2}{2k_B T\omega_0^2}} \tag{1.65}$$

after rewriting $v_z = \frac{c(\omega_0'-\omega_0)}{\omega_0}$. $g^*(\omega_0' - \omega_0)$ is a Gaussian function with FWHM:

$$\Delta\omega = 2\omega_0\sqrt{\frac{2k_B T log(2)}{Mc^2}} \Rightarrow \Delta\nu = 2\nu_0\sqrt{\frac{2k_B T log(2)}{mc^2}} \tag{1.66}$$

This FWHM is the dominant contribution when considering low pressure gas samples.

Eq.(1.66) is of particular relevance because it links the linewidth of the optical absorption to the thermal energy $k_B T$, enabling the determination of the Boltzmann constant k_B fixing the temperature or vice-versa; this is the principle of Doppler-Broadened-Thermometry.

1.2.3 Voigt Profile and Beyond

This subsection gives a picture of the line-shape models when multiple broadening mechanism come into play combined with collisional effects; detailed treatments of molecular absorption profiles are given in Refs. [19, 20].

In the underlying assumption where the Doppler broadening gives the dominant contribution, it can be treated independently from collisional effects. Thus the distribution of the emitters with a particular velocity is still described by the Gaussian function arising from the Maxwell-Boltzmann distribution which is convolved with the Lorentzian contribution providing the so-called Voigt profile:

$$g_{tot}(\omega - \omega_0) = g_L(\omega - \omega_0) \otimes g_G^*(\omega_0' - \omega_0) = \int_{-\infty}^{+\infty} g(\omega - \omega_0')g^*(\omega_0' - \omega_0)d\omega_0' \tag{1.67}$$

which takes into account both the Lorentzian g_L and the Gaussian g_G widths and the pressure-induced shift of the centre frequency.

Eq.(1.67) neglects the correlation between collisional effects and the speed of the molecules, but in reality, as pressure increases, velocity changes due to collisions cannot be neglected. Dicke demonstrated that these changes caused by collisions reduce the linewidth of the Doppler profile for a given temperature and this effect is called Dicke-narrowing [21]. Two models takes into account velocity changing collisions depending on the kind of colliding particles with the absorbing molecules, usually referred to as emitters. If the strength of the collisions is such that the emitter's velocity after the impact is totally uncorrelated from the previous one and follows again the Maxwell-Boltzmann distribution, then the regime is called hard-collisions.

Typically this happens when the masses of the emitters are much lower then the masses of the perturbing colliding particles. The Rautian (RP) [22] and the Nelkin-Ghatak (NGP) [23] profiles are the models considering this hard collision regime. Instead, if several collisions are required to completely change the particle's velocity, the regime is called soft-collisions. In this case the individual collisions are negligible, but the overall amount of them causes the emitters motion to become a Brownian motion. This regime is reached when the masses of the emitters are higher than those of the colliding particles. The Galatry (GP) profile [24] deals with this kind of collisional effect within the Doppler broadened profile.

Also the hypothesis that the Doppler effect is uncorrelated from molecular collisions is not always valid, because the relaxation decay rates are affected by speed dependent effects caused by collisions at a given temperature T. When the correlation between collisions and the Doppler broadening has to be taken into account the speed-dependent Voigt Profile (SDVP) [25] is provided, also the speed-dependent versions of the GP and NGP profiles have been developed when the previous correlation and velocity changing collisions have to be considered.

In 2014 the IUPAC Task Group has recommended the adoption of the partially Correlated quadratic-Speed-dependent Hard-Collision (pCqSD-HC) profile, usually referred to as the Hartmann-Tran Profile (HTP), as the appropriate model for high-resolution spectroscopy. This profile takes into account various collisional perturbations to the absorption line-shape [20], also it requires small computational times thanks to the implementation provided by Ngo *et al.* [26], thus it can be easily integrated into a fitting routine. The HT profile has been adopted for the analysis of the absorption profiles to extract their Doppler-widths and perform Doppler-Broadening Primary Thermometry, as it is going to be discussed in 5.2.2. In particular, we used the HTP form obtained under the quadratic approximation for the collisional width (Γ) and shift (Δ). The latter considers the complex dephasing collision frequency $\Gamma + i\Delta$ as a function of the square of the molecular speed v:

$$\Gamma(v) + i\Delta(v) = (\Gamma_0 + i\Delta_0) + (\Gamma_2 + i\Delta_2)\left[\left(\frac{v}{\overline{v}}\right)^2 - \frac{3}{2}\right] \tag{1.68}$$

where Γ_0 and Δ_0 are the average of the collisional width and shift over all molecular speed, Γ_2 and Δ_2 are the quadratic contributions linearly related to Γ_0 and Δ_0 with linear coefficients a_W and a_S, rspectively, depending on the intermolecular potential considered [27], and $\overline{v}$ is the most probable speed. In the previous approximation the normalized HTP formula is the following:

$$HTP(\omega) = \frac{1}{\pi} Re \left\{ \frac{A(\omega)}{1 - \left[\beta - \eta\left(C_0 - 2C_2/2\right)\right] A(\omega) + \left(\eta C_2/\overline{v}^2\right) B(\omega)} \right\} \tag{1.69}$$

where β is the frequency of velocity-changing collisions quantifying the impact of Dicke narrowing, η is the temporal correlation between velocity-changing collisions and dipole-dephasing collisions, C_0 and C_2 are $\Gamma_0 + i\Delta_0$ and $\Gamma_2 + i\Delta_2$ respectively, whereas $A(\omega)$ and $B(\omega)$ are given by the integrals:

$$A(\omega) = \int \frac{f_{MB}(\mathbf{v})}{i\left(\omega - \omega_0 - \mathbf{k}\ \mathbf{v}\right) + (1-\eta)\left\{C_0 + C_2\left[\left(\frac{v}{\overline{v}}\right)^2 - \frac{3}{2}\right]\right\} + \beta} d\mathbf{v} \tag{1.70}$$

$$B(\omega) = \int \frac{v^2 f_{MB}(\mathbf{v})}{i\left(\omega - \omega_0 - \mathbf{k}\ \mathbf{v}\right) + (1-\eta)\left\{C_0 + C_2\left[\left(\frac{v}{\overline{v}}\right)^2 - \frac{3}{2}\right]\right\} + \beta} d\mathbf{v} \tag{1.71}$$

where $f_{MB}(v)$ is the Maxwell-Boltzmann distribution. The absorption coefficient is obtained from Eq.(1.69) multiplied by the integrated absorbance. By fixing some parameters of the HT profile to specific values related to the physics of the collisional processes, it is possible to retrieve most of the aforementioned profiles. For instance, fixing β and η to zero lead to the SDVP, which are the constraint posed in the spectra analysis described in 5.2.2.

1.3 Non-Linear Absorption Effects: The Saturation Regime

In the previous section the broadening mechanisms of molecular absorption line shapes have been described. The major broadening is imposed by the Doppler effect, which dominates by more than three order of magnitudes with respect to the others broadening mechanisms. To overcome this limit, one possible approach is to exploit non-linear effects of the absorption.

Several non-linear techniques have been developed since the 1960's to achieve ultra-high resolution and precise optical spectroscopy, the most known are Saturation Spectroscopy, Two-photon spectroscopy and Spectroscopy of trapped particles. Two-photon spectroscopy consists in the compensation of the Doppler effect by simultaneous absorption of two photons of counter propagating beams, Spectroscopy of trapped particles consists in reducing the motions of atoms or molecules employing high intensity light beams; this is the principle of laser cooling and the interested reader is referred to [28, 29] for instance.

The next subsections focus on the saturation of the absorption, firstly in the case of homogeneous broadening mechanisms and then including the inhomogeneous Doppler broadening.

1.3.1 Saturation of a Homogeneously Broadened Profile

The following analysis regards the saturation regime in the presence of homogeneous broadening. To understand the effect of saturation, the starting point is to refer to the variation of the density population $\Delta N = N(\rho_{11} - \rho_{22})$ in the simple case where only natural broadening is present. Here we have to consider the general case in which the interaction between the medium and the electric field is no more weak and no approximation can be done in the expression of ΔN.

Recurring to the nomenclature of the decay-time constant for off-diagonal element as T, the population relaxation decay constant as τ and the Rabi oscillation frequency as $\Omega = (\mu E_0)/(\hbar)$, we are going to use the complete expression of ΔN, provided for instance in Ref. [30], that is:

$$\Delta N = N(\rho_{11} - \rho_{22}) = \Delta N_{eq} \left(1 + \frac{(\omega - \omega_0)^2 T^2}{1 + (\omega - \omega_0)^2 T^2 + \Omega^2 T \tau} \right)^{-1} \tag{1.72}$$

In the approximation of a weak interaction, Eq.(1.72) becomes equal to Eq.(1.34) of Subsection1.1.1:

$$\Delta N = N(\rho_{11} - \rho_{22}) = \Delta N_{eq} \left(1 - \frac{(\omega - \omega_0)^2 T^2}{1 + (\omega - \omega_0)^2 T^2 + \Omega^2 T \tau} \right) \tag{1.73}$$

Eq.(1.72) can be rewritten as:

$$\Delta N = \Delta N_{eq} \left(1 + \frac{G \Gamma^2}{1 + (\omega - \omega_0)^2 + \Gamma \gamma} \right)^{-1} \tag{1.74}$$

after introducing the decay rates $\gamma = 1/\tau$,$\Gamma = 1/T$ and the so-called saturation parameter G defined as:

$$G = \frac{\Omega^2}{\gamma \Gamma} \tag{1.75}$$

Without loosing generality, the relaxation rate of the population density can be considered of the same order of magnitude of the decay rate of the off-diagonal elements: $\gamma \sim \Gamma$ and $\gamma \Gamma \approx \Gamma^2$. It is possible to show that for strong electric fields $G >> \frac{\Gamma^2}{1+(\omega-\omega_0)^2+\Gamma^2}$ and the difference in the population density is approximated at a first order by:

$$\Delta N = \frac{\Delta N_{eq}}{1 + G} \tag{1.76}$$

The absorption coefficient can be obtained from Eq.(1.76) as:

$$\alpha(\omega - \omega_0) = \frac{\alpha_0}{1 + G} \tag{1.77}$$

where α_0 is the absorption coefficient derived in the case of a weak interaction in Eq.(1.45) with the expression:

$$\alpha_0 = \sigma(\omega - \omega_0)\Delta N_{eq} \tag{1.78}$$

To better understand the meaning of the saturation parameter G, it can be expressed as the intensity ratio:

$$G = \frac{I}{I_S} \tag{1.79}$$

where I is the intensity of the electric field and I_S is the so-called intensity saturation defined as:

$$I_S = \frac{\epsilon_0 c \hbar^2 \Gamma^2}{\mu^2} \tag{1.80}$$

For intensities $I >> I_S$ the population difference ΔN decreases toward zero, meaning that the majority of the electrons are in the excited state. In this situation the absorption coefficient deviates from the linear behaviour with respect to ΔN_{eq} and reaches an asymptote value.

Consider now the case where the homogeneous broadening is not caused only by spontaneous emission. Indeed the dominant contributions comes from collisions and the transit-time effect. In this general case the decay rate is expressed as a function of the collisional rate $C_p p$ and to the transit-time rate $C_t = \gamma_t$, with C_p and C_t respectively expressed in MHz/torr and MHz. Taking into account the randomness of the collisions (the scalar product $\vec{\mu} \cdot \vec{E} = \mu E/3$) and the Maxwellian distributions of velocities, the saturation intensity expression is with good accuracy:

$$I_S = \frac{3\epsilon_0 c h^2}{\mu^2} 10^{12} \left(C_p p + C_t\right)^2 \tag{1.81}$$

The factor 10^{12} is due to the unit conversion to obtain I_S in W/cm^{-2} [30].

To reach the saturation intensity expressed in Eq.(1.81) it is possible to employ high intensity beams and working at low sample pressure, working conditions that are the typical reached when focusing the laser beam into the cell containing the molecular gas at low pressure.

It is worth noticing that the saturation intensity depends on homogeneous broadening parameters and is independent of inhomogeneous broadening.

1.3.2 Saturation of an Inhomogeneously Broadened Profile

Until now the advantage of reaching the saturation regime has not yet been shown, indeed it becomes evident when including the inhomogeneous Doppler broadening. The following description takes into account the saturation of a Doppler broadened profile from an analytical point of view, focusing in particular on the phenomenon of spectral "hole" burning and generation of the so-called Lamb dip. For the a detailed treatment of this non-linear regime the reader is referred to [12].

Consider an ensemble of particles in the simple case of two level systems, respectively the ground and the excited state, with resonant frequencies ω_0' centred at ω_0 with a Gaussian distribution $g^*(\omega_0' - \omega_0)$ caused by Doppler broadening. The saturation condition within a Doppler broadened absorption profile can be achieved only with two interacting beams, the first called pump, with frequency Ω and intensity I which is the higher among the two beams, and the second called probe, with frequency ω. We are not going to include the intensity of the probe beam in the mathematical expressions. Let us introduce the fraction of the population density of the ground level with resonance condition within $(\omega_0', \omega_0' + d\omega_0')$ and referred to it as $dN_1(\omega_0')$, together with the fraction of the population density of the excited level $dN_2(\omega_0')$ and the homogeneous cross section centred at ω_0' $\sigma^{hom}(\omega - \omega_0')$. The contribution to the absorption $d\alpha(\omega)$ due to the particles of the ensemble with resonance frequencies within $(\omega_0', \omega_0' + d\omega_0')$ is:

$$d\alpha(\omega - \omega_0) = \sigma^{hom}(\omega - \omega_0')[dN_1(\omega_0') - dN_2(\omega_0')] \tag{1.82}$$

The absorption coefficient for the probe beam due to the overall ensemble of atoms or molecules is then $\alpha(\omega) = \int d\alpha(\omega)$. Exploiting the density matrix formalism with analogues mathematical passages described for the homogeneous case it is possible to retrieve the difference of the fractional population densities as:

$$dN_1(\omega_0') - dN_2(\omega_0') = \frac{dN_{eq}(\omega_0')}{1 + \left(\frac{2I\sigma^{hom}(\Omega - \omega_0')}{\hbar\omega_0'\Gamma}\right)} \tag{1.83}$$

remembering that I and Ω are the intensity and the frequency of the pump beam respectively and Γ is the decay rate of decay representing the loss of coherence in the oscillation.

The complete absorption profile is thus deduced integrating Eq.(1.82):

$$\alpha(\omega - \omega_0) = \int \frac{\sigma^{hom}(\omega - \omega_0')\Delta N_{eq} g^*(\omega_0' - \omega_0)}{1 + \left(\frac{2I\sigma^{hom}(\Omega - \omega_0')}{\hbar\omega_0\Gamma}\right)} d\omega_0' \tag{1.84}$$

where σ^{hom} contains the Lorentzian contribution due to the homogeneous broadening.

It can be demonstrated that for $I = 0$, meaning no pump is present, the absorption profile is proportional to the convolution of $g^*(\omega_0' - \omega_0)$ with $g(\omega - \omega_0')$ which is a Voigt profile in the simplest case where no collisional or speed dependent effects are considered. Whereas when the pump is present, a "hole" is formed for $\omega \approx \Omega$ with an FWHM proportional to the homogeneous one $\Gamma_B = \Gamma\sqrt{1+G}$ and with a depth that increases as a function of pump intensity I. This phenomenon is called Spectral Hole Burning and the hole in the absorption profile is called Bennett's hole, in honour to the scientist that have studied their generation [31]. Figure 1.2 shows a picture of a Bennett hole.

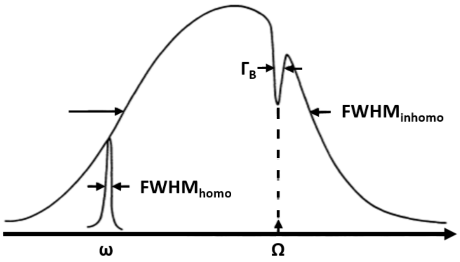

Figure 1.2: Spectral hole burning and generation of the Bennett hole in the absorption coefficient when the probe frequency ω is tuned at the pump frequency Ω.

Spectral hole burning can be explained qualitatively in an easy way as following: when the pump beam interacts with the sample, if the intensity is high enough it "burns" a hole in the population density N_1 and also causes an increment in N_2. Then if the probe beam is counter-propagating with respect to the pump and interacts with the sample within a temporal interval shorter than the decay time, it experiences less absorption when lying in the frequency interval $(\omega_0' + d\omega_0')$ because of the "hole" in the absorbing population N_1 generated by the pump.

In molecular spectroscopy, it is possible to exploit in a very useful way the effect of hole burning to overcome the limitation in the resolution imposed by the Doppler effect. Indeed in the presence of two counter propagating beams forming a standing wave condition, for example in an optical cavity containing the gas sample, the hole burning effect is generated at the centre of the Doppler profile. The molecular sample interacts with the two counter propagating waves by means of their effective resonance frequencies, that depends on the velocity projection of the particle onto the beam direction.

When the effective interaction frequencies of the two beams are located symmetrically about the centre frequency and the distance is larger than the characteristic Bennett FWHM, the two waves burns two independent holes in the difference of the population density distribution. In this case the Doppler profile shows no distortion. However, when the frequency of the laser is tuned to centre frequency of the Doppler profile, the effective frequency of the two counter propagating waves are at same value (which means that the interaction is with molecules that have no velocity component onto the beam direction and do not shift the real frequency of the interacting beam) a resonant dip, called Lamb dip [32], is generated.

Using the density matrix formalism in this case when the interacting electric field is represented by a standing wave, it is possible to obtain an equation for the saturated absorption coefficient in the presence of inhomogeneous broadening. The analytical passages are reported in Ref. [12] for instance, here let us remark the most important results. The total absorption coefficient is expressed as:

$$\alpha(\omega-\omega_0)=\alpha_0\frac{\left(1+\dfrac{A}{B}\right)}{\sqrt{(\omega-\omega_0)\Gamma[(A+B)^2-4(\omega-\omega_0)^2]}} \tag{1.85}$$

where $\alpha_0=\Delta N_{eq}\sigma$ is the absorption for weak field, $A=((\omega-\omega_0)^2+\Gamma^2)^{\frac{1}{2}}$ and $B=[(\omega-\omega_0)^2+\Gamma^2(1+2G)]^{\frac{1}{2}}$.

Far from resonance the two holes in the population densities do not overlap, and Eq.(1.85) can be approximated by:

$$\alpha(\omega-\omega_0)=\frac{\alpha_0}{\sqrt{1+G}} \tag{1.86}$$

whereas on resonance:

$$\alpha(\omega-\omega_0)=\frac{\alpha_0}{\sqrt{1+2G}} \tag{1.87}$$

which represent the so-called Lamb dip. The dip is centred at the frequency ω_0, with a likely Lorentzian shape, if the Transit-Time broadening is negligible, and with a FWHM expressed as:

$$\Gamma\sqrt{1+G} \tag{1.88}$$

In the presence of a non negligible Transit-time broadening, the shape of the dip is no more Lorentzian and becomes asymmetric [18].

The relative dip depth is obtained from the difference of Eq.s(1.86)−(1.87) and dividing for α_0 leading to:

$$h_{dip}=\frac{1}{\sqrt{1+G}}-\frac{1}{\sqrt{1+2G}} \tag{1.89}$$

This quantity corresponds to the effective signal-to-noise ratio of the saturation feature, fundamental for spectroscopic determinations.

A simplified version of the complete absorption profile (1.85) is available for weak saturation condition ($G << 1$) and was firstly retrieved by Lamb [32]:

$$\alpha(\omega-\omega_0)=\alpha_0\left[1-\frac{G}{2}\left(1+\frac{\Gamma^2}{\Gamma^2+(\omega-\omega_0)^2}\right)\right] \tag{1.90}$$

which takes into account the presence of the dip at the centre of the Doppler broadened profile and lead to a good estimation of the dip depth, but does not fully describe the deformation of the Doppler broadened profile.

In the weak saturation regime, the width of the dip is close to the homogeneous broadened one (since $G << 1$ in Eq.(1.88)) and spectroscopic investigations of the Lamb dip are no more limited in resolution by the Doppler broadening but only by the homogeneous broadening. Thus the retrieval of the line centre frequency is more precise leading to statistical uncertainties at the kHz level (since the homogeneous FWHM is few hundreds of kHz) over a total Doppler broadened profile with typical width of the order of hundreds of MHz. Also, the dip contains information related to the homogeneous processes affecting the molecular sample which can be studied without the limitation imposed by the Doppler broadening, paving the way to analysis of the Collisional and Transit-time broadening effects for molecular ensembles at room temperature.

1.4 Molecular Energy Levels and Transitions in the IR Region

The previous sections have treated transitions in the approximation of two-level systems. The formalism can be extended to the case of molecular gases transitions, where the two energy levels involved in the absorption processes are part of a complex structure made by several energy levels, usually referred as energy band. This section gives a picture of the molecular energy levels structure, focusing on the group of transitions excited by IR electric fields, those investigated in this thesis.

In the quantum theory of molecules developed by Born and Oppenheimer [33], the Hamiltonian describing molecular motion can be divided in four main terms:

$$H = H_{electronic} + H_{vibration} + H_{rotation} + H_{translation} \tag{1.91}$$

related to the electronic, vibrational, rotational motions and translations respectively. Typically the translational term is neglected because it does not participate in the interaction with light beams. The dominant energetic contribution comes from the electronic motions, where a transition between electronic levels requires the absorption of a photon with energies between 1 and 10 eV, i.e. visible and ultraviolet photons. Vibrational transitions are excited by photons with energies between 0.1 and 1 eV, i.e. near-IR and Mid-IR photons. Rotational transitions needs photon energies bewteen 0.0001 and 0.1 eV possessed by microwave photons.

The subject of this thesis is near-IR molecular spectroscopy of gas samples, where both vibrational and rotational transitions combined are present. For the novice reader, detailed essays can be found elsewhere [34–36] for instance. Following the Born-Oppenheimer approximation [33], during an energy level transition the nuclei of atoms are considered stationary respect to the electrons which are lighter. Energy levels are then calculated considering the nuclei at fixed arbitrary positions, with no kinetic energy but with a potential energy that depends on the internuclear separation. This potential energy is represented by the Morse potential function [37], as shown in Figure 1.3.

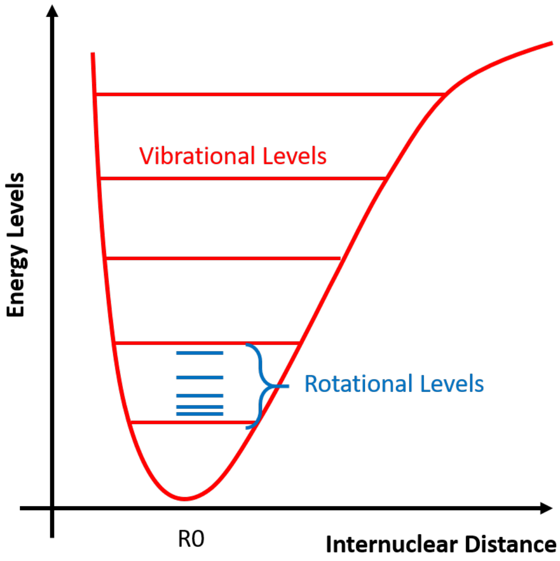

Figure 1.3: Rovibrational energy levels as a function of the internuclear distance. Rotational levels are coloured in blue, whereas vibrational are coloured in red.

The solution of the Schrödinger equation for electrons where the potential energy curve is the one cited above leads to the retrieval of the quantized energy levels as shown next.

1.4.1 Rotational Energy Levels

Molecules are ensembles of atoms bound together at stable distances. In this kind of discrete systems it is possible to define the moment of inertia I as:

$$I = \sum_{i=1}^{N} m_i r_i^2 \tag{1.92}$$

where m_i is the mass and r_i is the distance of the i-atom with respect to a rotational axis passing through the centre of mass of the system. The moment of inertia of the electrons is small with respect to that possessed by the nuclei, thus it can be neglected.

Consider now the simple case of linear rotor molecules, a system in which the atoms are positioned on a straight line. This is the case of diatomic molecules or some polyatomic molecules, such as HCl, CO, CO_2 etc. For these molecules, it is useful to define the reduced mass:

$$\mu = \frac{\prod_{i=1}^{N} m_i}{\sum_{i=1}^{N} m_i} \tag{1.93}$$

and consider the system as a single particle with mass μ rotating at a distance r from the centre of mass. The moment of inertia is then $I = \mu r^2$. Classically the energy possessed by such a system rotating around a fixed axis, x for instance, is related to the moment of inertia I_x and the angular velocity ω_x of the centre of mass:

$$\varepsilon_x = \frac{1}{2} I_x \omega_x^2 = \frac{L_x^2}{2I_x} \tag{1.94}$$

The last equality introduces the angular moment $L = I\omega$.

The classical selection rule for rotational transitions is that the molecule has to possess a dipole moment μ, at least transiently during the interaction. Intense rotational lines are shown by strongly polar molecules, whereas rotational inactive molecules are homo-nuclear diatomic and symmetric linear molecules, CO_2 is an example. The right description follows quantum mechanics, where the system is represented by the rotational Hamiltonian:

$$H_x = \frac{\widehat{L}_x^2}{2I_x} \tag{1.95}$$

The angular moment operator can only take quantized values in terms of the rotational quantum number $l = 0, 1, 2, ...$:

$$\widehat{L^2} = \hbar^2 l(l+1) \tag{1.96}$$

The quantized eigen-values, solution of the time independent Schrödinger's equation, are:

$$\varepsilon_{rot} = \frac{\hbar^2}{2I} l(l+1) \tag{1.97}$$

Usually the term $\frac{\hbar^2}{2I}$ is included in a spectroscopic constant named B. Notice that the values of Eq.(1.97) are $(2l+1)$-fold degenerate.

The degeneracy can be lifted by applying a magnetic field, for instance, and the operator that lifts the degeneracy of energy levels is the projection of the angular moment to the vertical axis respect to the plane where the molecule lies, usually indicated with the letter z. $\widehat{L_z}$ can take only the following values:

$$\widehat{L_z} = m\hbar \tag{1.98}$$

where m is a quantum number spacing from $\pm l$.

Within an electric dipole interaction, selection rules for Eq.s(1.96) and (1.98) are obtained as:

$$\Delta l = \pm 1; \Delta m = 0, \pm 1 \tag{1.99}$$

where the expression on the left side shows that transitions can happen only between adjacent levels with different l. The selection rule on the right side shows how other transitions are possible after lifting the $(2l+1)$-fold degeneracy.

The rigid rotor model is a simplification of a real molecule. More sophisticated models considers the atom connected by elastic springs where distortions are included during the rotation of the system, in particular correction terms regards the effect of centrifugal forces. The rigorous treatment, reported for instance in Ref. [38], leads to a definition of the rotational energy levels as a series expansion of the term $l(l+1)$:

$$\varepsilon_{rot} = hc\left[Bl(l+1) - Dl^2(l+1)^2 + Hl^3(l+1)^3 + Ll^4(l+1)^4\right] \tag{1.100}$$

where letters refer to specific spectroscopic constants: D takes in account bond distortions, H and L regards high-order corrections.

The previous quantum mechanical formalism can be applied to other systems with different geometries, for example for symmetric rotor molecules, spherical rotor molecules and so on. The reader is referred to [35, 36] if interested in different geometries with respect to the linear rotor treated above.

1.4.2 Vibrational and Rovibrational Energy Levels

From Figure 1.3, the potential function possesses a minimum at an internuclear distance R_0 that is called equilibrium distance where the bond is stable. The Morse function is an approximation of the real potential function, because for values lower than R_0 it does not fully consider the nuclear repulsion interactions.

A simplified treatment to obtain the energy levels starts from the case of a quantum harmonic oscillator, which possesses a parabolic potential approximating the Morse function for internuclear distances close to R_0. The atomic bond is depicted as a spring which lets the atoms oscillate in the case of a transition from the ground to the excited state. A classical description of the harmonic oscillator does not lead to the quantization of the energy levels, this is correctly accounted by quantum mechanics.

With the quantum mechanical formalism, solving the Schrödinger equation for electrons within the harmonic potential gives the quantized energy levels as functions of the quantum number $v = 0, 1, 2, ...$:

$$\varepsilon_{vib} = \left(v + \frac{1}{2}\right) h\nu = \left(v + \frac{1}{2}\right) \hbar\omega \tag{1.101}$$

Interestingly, the system possesses a potential energy even for $v = 0$ called zero-point energy, which is a difference respect to the rotational energy levels and cannot be taken into account classically. The selection rule for a vibrational electric dipole transition is:

$$\Delta v = \pm 1 \tag{1.102}$$

It has to be noticed that the harmonic oscillator model is an approximation that holds correctly only for the first three energy levels represented Eq.(1.101). The inclusion of the not-harmonic behaviour of the potential function gives the correct energy levels expression. Also using the Morse potential function, selection rules for overtone transitions can be obtained as:

$$\Delta v = \pm 2, \pm 3, \ldots \tag{1.103}$$

These transitions, referred to as overtone transitions, are not comprised in the harmonic approximation and their intensities are several orders of magnitude lower than the fundamental ones. Overtone transitions are the main investigated in this thesis.

As depicted in Figure 1.3, rotational levels are included between vibrational levels. Vibrations slightly change the geometry of molecules, thus the rotational levels are functions of the vibrational level on which they lie. The interactions between vibrations and rotations have to be taken in account to fully describe the molecular spectra. The spectroscopic constants, introduced for rotational levels, become functions of the v quantum number. The levels, combinations of rotational and vibrational energy levels, are usually called rovibrational levels, with energies represented by:

$$\varepsilon_{rovib} = hc\left[G_v + B_v l(l+1) - D_v l^2(l+1)^2 + H_v l^3(l+1)^3 + L_v l^4(l+1)^4\right] \tag{1.104}$$

where G_v refers to the zero-point energy.

Figure 1.4 shows three main branches for transitions between rovibrational levels distinguished by the selection rule considered, in particular the P-branch is selected when $\Delta l = -1$, the R-branch when $\Delta l = +1$ and the Q-branch, that is excited only in the presence of additional electronic motions, when $\Delta l = 0$. In this work of thesis, the rovibrational transitions considered lies in the P-branches of CO_2 and C_2H_2.

The previous levels transitions are tabulated with their characteristic spectroscopic parameters for several different molecules and isotopes in the HITRAN database [17]. The readers is referred to the supplementary materials of Ref. [15] for an explanation of the quantities reported in the database and also for the complete nomenclature of the transitions of different branches.

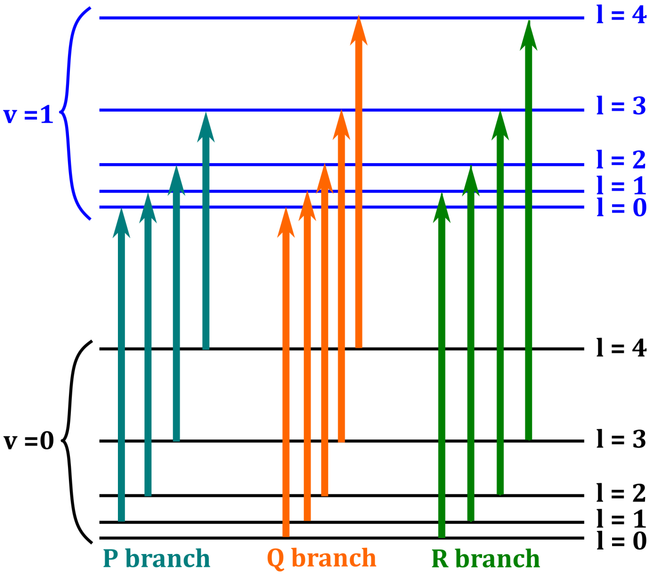

Figure 1.4: Rovibrational transitions between energy levels of a molecular system for the three branches P, Q and R.

Chapter 2

Optical Frequency Combs for Molecular Spectroscopy

The following chapter concerns optical frequency combs. Thanks to their peculiar frequency structure, frequency combs enabled a revolutionary advancement in several fields, such as optical metrology, precision spectroscopy and attosecond science to name a few. In this thesis an optical frequency comb has provided absolute calibration of the frequency axis for molecular spectroscopy measurements. The chapter is divided into three main sections: the first section gives the time and frequency-domain picture of optical frequency combs together with an analysis of the noise sources affecting the linewidth of the comb modes. The second section surveys different types of frequency comb synthesizers and their typical performances. The last section shows some of the most relevant applications of frequency combs, with a focus on Comb-Assisted Molecular Spectroscopy that is of main relevance for the PhD activity.

2.1 Frequency Combs: Operation Principle

Since the invention of mode-locked lasers in the early 1970s, their capability to generate optical pulses in the picosecond and femtosecond range was used in time-resolved spectroscopy measurements, reviewed in details in [39].

Only at the end of the 1990s the first frequency comb was implemented, achievement recognised by co-awarding Theodor W. Hansch and John L. Hall with the Nobel Prize for Physics in 2005. Thereafter, frequency combs paved the way to molecular spectroscopy with unprecedented levels of both precision and accuracy in absorption line detection. For instance, the field of trace gas sensing has seen tremendous improvements in terms of sensitivity, broad spectral coverage and high resolution when passive high-finesse optical cavities were conjugated with frequency combs used either as probe or as reference sources.

2.1.1 Time and Frequency Domain Representation

To better understand the spectral structure of frequency combs, which is at the basis of the enhancements listed before, this subsection describes analytically the electric field associated to these special laser sources.

In a mode-locked laser, an optical pulse train arises when a huge number of longitudinal modes ν_n oscillates in phase forced by a non-linear process, for example the non-linear optical Kerr effect. In a time domain representation, the coherent superposition of those modes produces a giant pulse circulating inside the optical cavity that gets partially transmitted every time it reaches the output mirror. This transmission happens at a period $T = \frac{2nL}{c}$ called pulse repetition rate, where L is the length of the optical cavity, n the refractive index and c the speed of light.

It is possible to mathematically express the electric field $E(t)$ emitted by a mode-locked laser as a convolution of an envelop function $A_0(t)$, giving the individual pulse profile, with a series of delta functions spaced by the period T:

$$E(t) = \left[A_0(t) \sum_{m=-\infty}^{m=+\infty} \delta(t - mT) \right] e^{i2\pi\nu_0 t} \tag{2.1}$$

where the phase term $e^{i2\pi\nu_0 t}$ originates from the underlying carrier frequency ν_0.

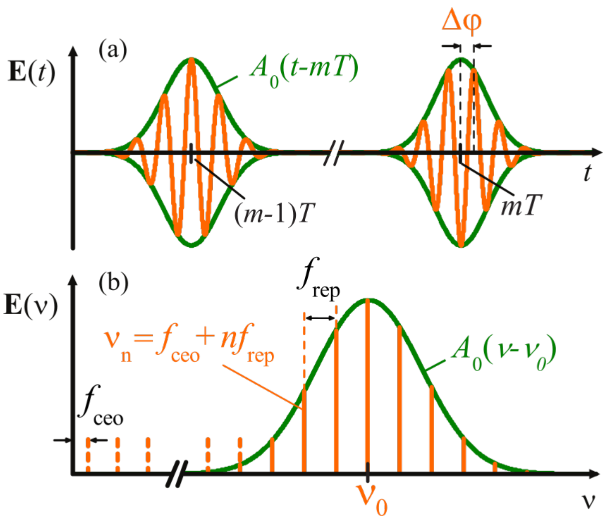

Figure 2.1: (a) Time domain representation of the electrical field profile of subsequent pulses (orange line) and the corresponding envelopes (green line). When moving from pulse to pulse, the carrier phase slips by $\Delta\varphi$ with respect to the envelope. (b) Frequency domain representation of an infinite pulse train: the spectrum is made up of a comb of modes separated by f_{rep} and offset by f_{ceo} with respect to integer multiples of f_{rep}.

As shown in Figure 2.1(a), the carrier frequency typically undergoes a phase slippage from pulse to pulse that breaks the periodicity of the waveform. The phase slippage is mainly caused by the difference between phase and group velocity in the laser resonator due to dispersion. Such a phase slippage impacts on the comb pattern in the frequency domain, as it is going to be shown next.

By Fourier transform of Eq.(2.1) the spectral counterpart $E(\nu)$ is obtained:

$$E(\nu) = \mathcal{F}[E(t)] = \left[A_0(\nu) \frac{1}{T} \sum_{k=-\infty}^{k=+\infty} \delta\left(\nu - \frac{k}{T}\right) \right] * \delta(\nu - \nu_0) \tag{2.2}$$

where $A_0(\nu)$ is the transform of $A_0(t)$. With the introduction of the laser repetition frequency $f_{rep} = \frac{1}{T}$, Eq.(2.2) is rewritten in the form:

$$E(\nu) = A_0(\nu - \nu_0) f_{rep} \sum_{k=-\infty}^{k=+\infty} \delta(\nu - \nu_0 - k f_{rep}) \tag{2.3}$$

The corresponding spectrum, shown in Figure 2.1(b), comprises different delta functions equally spaced by f_{rep}, whose amplitude are modulated by the $A_0(\nu - \nu_0)$ spectral envelope. Defining an integer number n_0 and a Radio-Frequency (RF) f_{ceo}, obeying the relation $\nu_0 = n_0 f_{rep} + f_{ceo}$ with the constraint $0 < f_{ceo} < f_{rep}$, and renumbering the sum in Eq.(2.3) with a new index $n = k + n_0$, it is possible to deduce a simple expression for the frequency domain spectrum:

$$E(\nu) = A_0(\nu - \nu_0) f_{rep} \sum_{n=-\infty}^{n=+\infty} \delta(\nu - n f_{rep} - f_{ceo}) = A_0(\nu_n - \nu_0) \tag{2.4}$$

where:

$$\nu_n = n f_{rep} + f_{ceo} \tag{2.5}$$

The last equation shows that the comb is made of different optical frequencies separated by f_{rep}, which gives the mode spacing, whereas f_{ceo} represents the offset of the optical modes respect to the origin of the frequency axis, as sketched in Figure 2.1(b). The number of constituting optical frequencies can be roughly estimated by the ratio of the pulse optical bandwidth divided by f_{rep}. Considering the case of a mode-locked laser with a spectral bandwidth of ~10 THz (pulses with a duration less than 100 fs) and f_{rep} of ~100 MHz, the number of optical modes is $\sim 10^6$.

The physical origin of f_{ceo}, where *ceo* is the acronym of carrier-envelope-offset, arises from the aforementioned phase slippage $\Delta\varphi$ between the carrier frequency and the pulse envelope. Following the procedure shown in Ref. [40], to quantify $\Delta\varphi$ and relate it to f_{ceo}, let us consider two time instants separated by a pulse repetition period T, $t_m = mT$ and $t_{m-1} = (m-1)T$, corresponding to the two adjacent envelope maxima in Figure 2.1(a) and also let us indicate with φ_m and φ_{m-1} the respective values of the absolute phase of their electric fields. The phase slippage $\Delta\varphi$ is the same from pulse to pulse and is given by the following relation:

$$\Delta\varphi = \varphi_m - \varphi_{m-1} = 2\pi\nu_0 T = \frac{2\pi(n_0 f_{rep} + f_{ceo})}{f_{rep}} = \frac{2\pi f_{ceo}}{f_{rep}} + \cancel{2\pi n_0} \tag{2.6}$$

which shows that the time-domain phase shift from pulse to pulse between the carrier and the envelope corresponds in the frequency domain to an offset f_{ceo} of the comb from simple integer multiples of f_{rep}.

Returning to Eq.(2.5), since f_{rep} and f_{ceo} lies in the RF range, they can be stabilized against a primary reference oscillator, such as a Cs clock. In this way the mode-locked laser becomes a frequency ruler called Optical Frequency Comb (OFC), with thousands of optical modes ν_n whose absolute values are known to an accuracy corresponding to the error propagation of f_{rep} and f_{ceo}. Therefore a frequency comb is also depicted as the superposition of thousands of lasers emitting in phase at specific and determined frequencies.

The stabilization of f_{rep} is relatively simple since the pulse repetition rate can be acquired by a fast photodetector and phase-locked to a primary reference by adjusting the cavity length of the oscillator, using a Piezo-Electric Transducer (PZT) mounted on one cavity mirror, or adjusting the phase by a fast intra-cavity Electro-Optic Modulator (EOM) [41]. On the other hand, detection of f_{ceo} remained the bottleneck for the realization of a frequency comb synthesizer until the end of the 1990's. An experimental solution was possible only in 1999, where it was found that femtosecond pulses maintain their phase-coherence when spectrally broadened in non-linear materials with a strong third order susceptibility $\chi^{(3)}$ [42]. The first direct optical-to-RF conversion was achieved using a complex scheme, with a frequency divider imposing fixed ratios and the superposition of the 3.5^{th} and 4^{th} harmonics of the mode-locked laser, as discussed in details in [40,43]. The task became strikingly simple with the advent of highly non-linear fibres, such as photonic crystal fibres, leading to the realization of an octave spanning spectrum [44], i.e. a frequency spectrum where the higher frequencies are a factor of two greater than the lower ones. Such a spectrally broadened laser allows for a direct measurement of f_{ceo} using a f-2f self-referencing scheme where only the direct output of the laser is needed [45, 46] without any frequency division. As it is shown in Figure 2.2, the superposition of a frequency doubled portion of the octave-spanning spectrum with the original spectrum on a photodetector generates a heterodyne beat-note signal between the $2\nu_n$ and the ν_m comb line, where $m = 2n$:

$$2\nu_n - \nu_m = 2(nf_{rep} + f_{ceo}) - (2nf_{rep} + f_{ceo}) = f_{ceo} \tag{2.7}$$

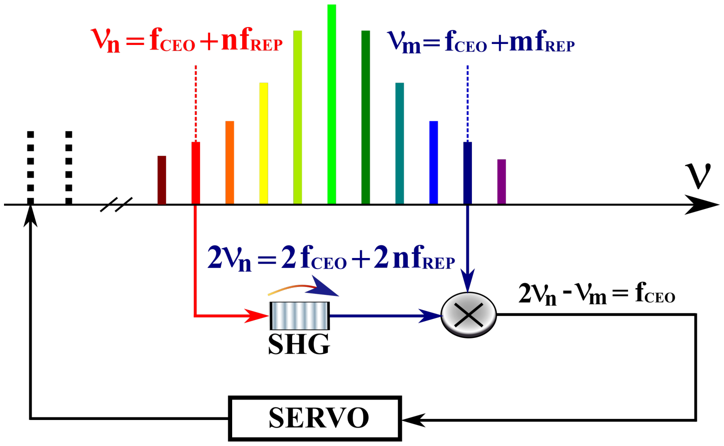

Figure 2.2: Self-referencing scheme of an octave broadened mode-locked laser. The f_{ceo} is extracted by frequency doubling the infrared spectral portion, using second harmonic generation (SHG), and mixing it with the visible part.

which corresponds directly to the carrier envelope offset frequency. f_{ceo} can be then phase-locked to a primary reference oscillator acting on the pump laser current [47] or tilting the high reflector mirror in solid-state femtosecond oscillators [44], which are two known ways to modify the intracavity dispersion and thus the phase slippage.

2.1.2 Noise properties

The previous treatment has been done in the ideal case where the laser pulses have an infinite coherence time t_c and consequently determine a spectrum composed of an ensemble of δ functions. In reality, several noise sources reduce the coherence time and the comb teeth exhibit a line-shape that has a non-negligible linewidth.

The different noise terms conditioning an OFC can be divided into two groups: extra-cavity noise sources, acting on the pulse train outside the laser cavity, and intra-cavity noise sources, affecting the pulse circulating inside the laser cavity. Extra-cavity noise includes path-length fluctuations, shot noise from the limited power per comb tooth and noise in the supecontinuum generation. Intracavity noise comprises Amplified Spontaneous Emission (ASE) driven noise, pump-induced noise and environmentally driven fluctuations in the cavity length and losses [48]. The same perturbation acts differently if it operates inside or outside the cavity. A typical example regards length changes, which inside the cavity shift the repetition rate and consequently all the portion of comb modes, whereas outside the cavity they modify only the phase of the electric field. Another example is the ASE, which inside the cavity causes frequency jitter of the comb modes, whereas outside the cavity mainly generates a white phase noise floor. In general, perturbations broadening the comb linewidth are mainly due by intra-cavity noise whereas perturbation decreasing the contrast and signal-to-noise-ratio of the comb modes are caused by extra-cavity noise.

As said in the previous section, a mode-locked laser becomes an OFC when the modes are stabilized at well-defined frequencies that can be expressed as $\nu_n = nf_{rep} + f_{ceo}$ which are functions of three parameters, respectively n, f_{ceo} and f_{rep}. Typically a frequency comb is synthesized acting on the noise sources affecting f_{ceo} and f_{rep}. For the following discussion it is useful to introduce the fixed-point formalism [49] to describe the intra-cavity noise sources. The basis of the formalism is that the different noise sources cause the comb to expand or contract about a single frequency, called fixed-point, in a breathing-like behaviour. As pump power noise has a fixed point at the carrier frequency, its impact due to the breathing mechanism around it is particularly severe for f_{ceo}. This has two main consequences: on the one hand the pump power noise can be monitored through f_{ceo} fluctuations, on the other hand pump power modulation is the most efficient actuator to control f_{ceo}, which explains why f_{ceo} is generally stabilized acting on the driving current of the laser pump diodes [50]. Differently, cavity length changes, for example due to mechanical and acoustic noise, are characterised by a fixed-point at nearly zero frequency and directly impact on f_{rep}. A first consequence is that f_{rep} variations are used to detect the presence of length-related noise sources, while the second is that changing the cavity length, by means of a PZT for instance, is an efficient way to modify and stabilize f_{rep} [51]. Actually, as cavity length noise affects the pulse repetition rate, and f_{rep} noise increases the high is the comb mode number n, the most efficient way to detect and suppress this noise is to lock a comb mode to a standard optical reference (characterised by a high mode number) instead of a RF standard (with mode number close to one), due to the favourable leverage in the comb tooth relation. Stabilization of the comb modes is possible acting on other parameters, such as cavity loss, fibre birefringence or cavity dispersion [48], but high dynamic ranges and high control bandwidths to achieve efficient phase-locking have been achieved by cavity length control and pump power modulation to stabilize respectively f_{rep} and f_{ceo}.

At the beginning of this section we said that intra-cavity noise sources mainly affect the tooth linewidth of the free-running comb. The two main causes determining the tooth linewidth are cavity length variations and pump power fluctuations, that is why the focus of the following discussion is on them. To understand their impact, let us consider the frequency noise Power Spectral Density (PSD), described in AppendixA for instance, of the different contributions, indeed the total PSD in the case of multiple uncorrelated noise is just the addition of the several PSD. Using the fixed-point formalism it is possible to relate the PSD of the fractional variation of the repetition rate fluctuation due to a noise contribution (X) $S_r^X(f)$ to the PSD of the n-th comb mode [48]:

$$S_{\nu n}^{X} = (\nu_n - \nu_{fix}^{X})^2 S_r^X(f) \tag{2.8}$$

where ν_{fix}^{X} is the fixed-point for the X contribution. So considering cavity length variations and pump power fluctuations the total PSD of the n-th comb modes is expressed as:

$$S_{\nu n} = (\nu_n - \nu_{fix}^{length})^2 S_r^{length}(f) + (\nu_n - \nu_{fix}^{pump})^2 S_r^{pump}(f) \tag{2.9}$$

Following Ref. [48], Figure 2.3 shows the total linewidth of the comb teeth across the optical frequencies. The pump noise contribution is negligible at the centre frequency ν_0 and increases almost linearly going to the wing of the spectrum, and from the $1/f$ noise deriving from cavity length fluctuations, which scales linearly as the n^{th}-mode number. The overall comb tooth linewidth has a minimum in the range of frequencies close to ν_0 and increases on both sides of the spectrum, in particular the linewidth obtained at 0 frequency is the linewidth of the f_{ceo}.

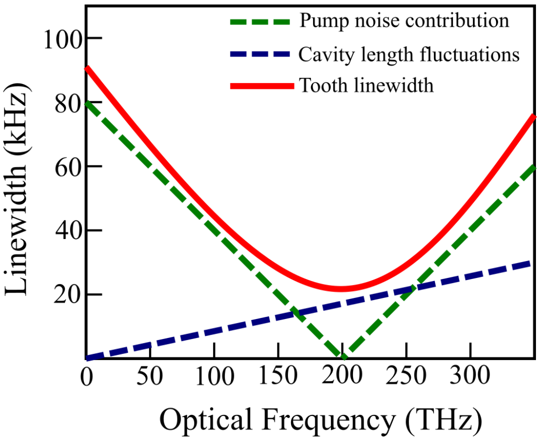

Figure 2.3: Linewidth of the comb modes of an Er:fibre comb as a function of the optical frequency (red curve), the two main contributions come from the pump noise (green-dashed curve) and the cavity length fluctuations (blue-dashed curve).

The previous behaviour is the one possessed by a frequency comb in the free-running condition. Phase locking of f_{rep} and f_{ceo} to radio-frequency standards lead to reduction of the tooth linewidth at the Hz-level. Now with the advent of intra-cavity electro-optical modulators, frequency combs can be stabilized by locking one comb tooth to a stable optical laser source transferring the phase properties of the reference to the comb, reaching the sub-Hz-level tooth linewidth. For instance a fibre frequency comb with low phase noise has been demonstrated firstly by narrowing the f_{ceo} [50] and then by phase-locking a single tooth to an optical reference [51].

2.2 Frequency Combs Synthesizers

In the last few decades, great achievements have been obtained in the realization of robust and reliable mode-locked laser sources to be used as frequency combs. This section gives a brief description of the most known OFC oscillators with their main characteristics, as summarized in Figure 2.4. For a broader overview the reader is referred to [52, 53].

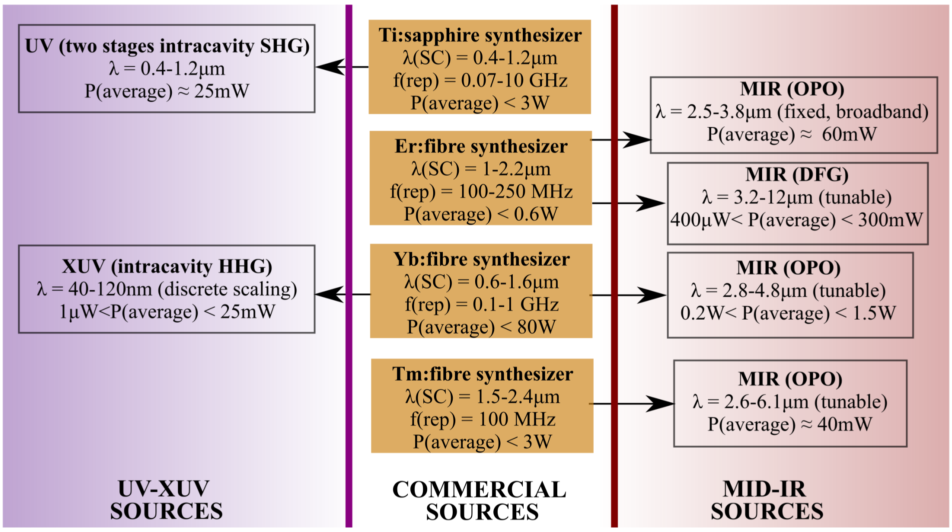

Figure 2.4: A viewgraph of OFCs in different spectral region starting from commercial sources (colored box). SC, SupeContinuum; SHG, Second Harmonic Generation; DFG, Difference Frequency Generation; OPO, Optical Parametric Oscillation; HHG, High Harmonic Generation.

2.2.1 Near-IR sources

The comb sources in the Near-IR region cover the spectral interval from 0.4 to 2.4 μm after supercontinuum (SC). They can be divided in two groups: solid-state and fibre-based sources.

The first generation of a frequency comb was achieved with a Ti:sapphire mode-locked femtosecond oscillator [46] Thanks to a wide oscillation bandwidth, enough to generate 10 fs pulses, an octave spanning spectrum for self-referencing was generated in a photonic crystal fibre. In the past decade also other solid-state based OFCs have been developed at a laboratory level from Cr:forsterite [54] and Er:Yb:glass [55]. Solid-state OFCs are mainly used in experiments that require short-term stability, because they exhibit lower frequency noise and narrower optical linewidths compared to their fibre-based counterparts described in the following. However, they need an engineered design of the cavity to reach a high level of stability, since they are typically based on free-space optics. Average free-running tooth linewidth of this kind of sources span from 1 kHz to 10 kHz and by active stabilization and referencing of a comb mode to an optical reference enabled the achievement of sub-kHz level linewidth [56].

After the first demonstration of an OFC, fibre-based frequency comb synthesizers have been intensely engineered because they offer some advantages such as size, efficiency and long term stability respect to their solid-state counterparts. From the beginning of the last decade, three gain media are widely used: Er-, Yb- and Tm-doped fibres. The first two media have seen a huge commercial spread and a high degree of system developments, whereas progresses for the last have grown only recently, driven by the purpose to extend the spectral coverage of fibre-based OFCs. Er:doped fibre oscillators with emission wavelength of 1.5 µm are the most diffuse because they can benefit from the highly implemented and low cost technology of the telecom range [57]. On the other hand, when high power are needed such as for non-linear processes, the best choices are Yb:fibre OFCs [58] reaching multi-Watt output powers. The most efficient sources in the 1.9 µm region are Tm:fibre based OFCs, reaching output powers at the Watt level [59]. With these highly versatile sources different amplification paths can be seeded with a single oscillator, multiplying the laser outputs. Since these outputs share the same f_{ceo}, when exploited in nonlinear Difference Frequency Generation (DFG), they can produce f_{ceo}-free combs in the Mid-IR region. Thus the knowledge of f_{rep} and the mode number n are enough for absolute calibration in spectroscopic measurements.

2.2.2 Beyond the Near-IR range

In the past few years, efforts have been spent to generate frequency combs in spectral regions not covered by the available Near-IR synthesizers, such as the Ultra-Violet (UV) and the Mid-IR. A picture of why these regions are so interesting for spectroscopy is given below. In the UV-XUV the attention is on the study of electronic transitions of single atoms, molecules and ions to test possible changing of fundamental constants over time [60] or for the development of new temporal references [61]. In the Mid-IR region, since a large number of molecules undergo strong characteristic individual or multiple rovibrational transitions, they are exploited for molecular detection and fingerprinting at trace level [62].

Reaching the UV and XUV ranges require non-trivial issues to be addressed. UV comb sources can be obtained through frequency doubling and quadrupling of Ti:sapphire lasers, achieving power of tens of mW with the use of enhancement cavities [63]. The XUV range has been reached thanks to a series of technical advancements in the efficient extraction of the XUV radiation generated by High-Harmonic Generation (HHG) in gas jet positioned within enhancement cavities pumped by Yb:fibre based combs [64].

Direct comb synthesis in the Mid-IR is a technological struggle due to the fact that no mode-locked lasers in that region provide an octave spanning spectrum. Thus, Mid-IR OFCs can be obtained mainly by non-linear approaches: Difference Frequency Generation (DFG) processes or Optical Parametric Oscillation (OPO).

Exploiting DFG between trains of phase-coherent pulses emitted by Er- or Yb-based oscillators allows the cancellation of the carrier envelope frequency and the generation of harmonic combs with no f_{ceo}. The latter is particularly useful when the comb source has not to be coupled in optical cavities, indeed in this case only f_{rep} remains as the sole parameter to achieve a stable and efficient coupling without recurring to other schemes. In Ref. [65] a Mid-IR frequency comb source covering the 3-10 µm region is generated in a GaSe crystal pumped by an Yb:fibre frequency comb, with averages power of 1.5 mW at 4.7 µm. Using shifted Raman solitons, from 1.76 to 1.93 µm, to seed the DFG process in GaSe from an Er:fibre oscillator lead to a wide tunability from 8 to 14 µm with an average power of 4 mW. Higher output powers reaching 120 mW are reported in Ref. [66], regarding the synthesis of a frequency comb covering the spectral region from 2.9 to 3.6 µm generated using an Er:fibre oscillator and DFG in a periodically poled MgO-doped lithium niobate crystal. More recently, Ref. [67] reports 60 mW in the region from 6-11 µm by DFG between erbium and thulium fibre amplifiers in orientation-patterned GaP.

By OPO, instead, it is possible to generate OFCs with output power overcoming the Watt level in the spectral region from 2.8 to 4.8 µm employing a periodically poled lithium noiobate crystal in a Singly-Resonant (SR) scheme [68]. Using SR-OPOs there is the possibility to control f_{ceo} at the price of quite complex schemes. Employing Doubly-Resonant (DR) OPO process makes the control of f_{ceo} and lead to the generation of broadband spectra, such as from 2.6 to 6.1 µm reported in Ref. [69] pumping an orientation patterned GaAs crystal with a femtosecond Tm-fibre and achieving 37 mW of average output power. With DR-OPO high power levels are difficult to achieve, also so broad spectra are difficult to couple within optical cavities due to the cavity dispersion and to the limited reflectivity bandwidth of the mirrors, that is why multipass cells are employed typically.

2.3 Applications of Frequency Combs

The generation of OFCs has paved the way to several technological advances spreading into different fields, thanks to their unique characteristic of a well-defined phase coherence over the optical spectrum. Figure 2.5 summarize briefly the main applications [53].

The following paragraphs reviews some of the major results obtained with frequency combs, while the next two subsections cover the fields of Comb-Assisted and Direct-Comb Molecular Spectroscopy, that are of main

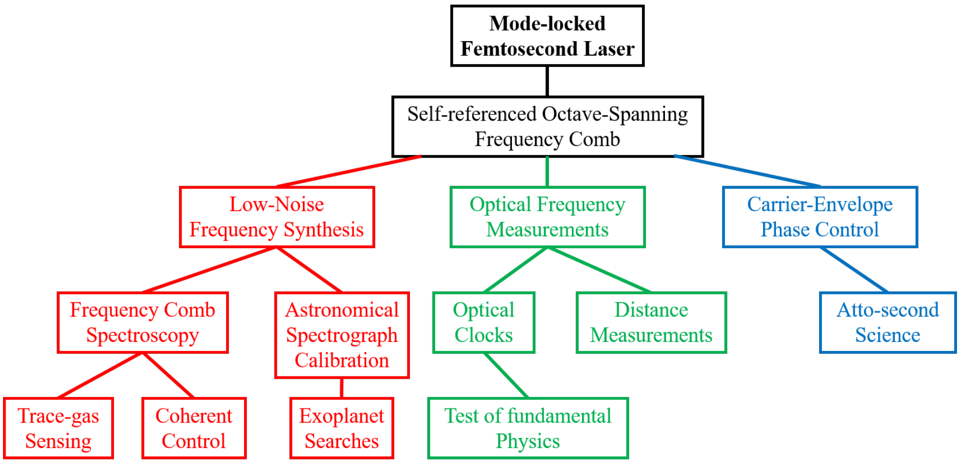

Figure 2.5: A scheme of the main applications of Frequency Combs developed over the past two decades.

interest for this thesis.

The primary field benefiting from the generation of OFCs was frequency metrology. Before the advent of OFCs, the experimental system to measure optical frequencies was the frequency multiplication chain where a precisely known frequency oscillator, such as a caesium clock, undergoes different nonlinear processes to generate harmonics of its frequency [70]. Through different steps was possible to reach the harmonic frequency necessary to obtain a beating signal between the probe laser, at an unknown frequency, and the reference laser from the optical chain. The complexity and the lack of compactness of the experimental configurations were the main limitations. With the availability of OFCs, absolute frequency measurements across spectral ranges from the UV to the Mid:IR became straightforward and also based, in most cases, on table-top commercial lasers. In just a decade, unprecedented levels of both precision and accuracy were obtained since the comb structure provides more than a million of optical narrow-linewidth modes with frequency positions known to better than 10^{15}. A milestone in this field was the determination of the Hydrogen 1S-2S transition frequency, performed by Niering et al. [71], at the $1.8{\cdot}10^{-14}$ level, achieved thanks to a high-stability Cs fountain clock, which has been improved few years ago to $4.2{\cdot}10^{-15}$ [72]. Such an ultra-precise spectroscopy stimulated various tests of fundamental physics, such as placing constraints on possible drifts of fundamental constants. Repeated measurements of the 1S-2S transition of Hydrogen at a distance of few years made possible to place an upper limit in the fractional temporal variation of the fine structure constant to $5.2{\cdot}10^{-17}$ year^{-1} limit in 2004 [73] that been shifted to $2.1{\cdot}10^{-17}$ year^{-1} in 2014 [74].

Another field strongly influenced by frequency combs regards optical atomic clocks. Traditional atomic clocks, such as the Cs clock, are based on microwave transitions where high-speed electronics count a defined number of cycles of the oscillator. Optical atomic clocks are based on the concept of using a frequency comb to count the optical frequency of an ultra-stable laser probing an ultra-narrow optical transition from either laser-cooled trapped ions or atoms [75] or optical lattice clocks [76]. With respect to microwave atomic clocks, optical clocks have the advantage of operating frequencies which are 10^5 times higher, enabling a more accurate division of the time scale. The first optical atomic clock was based on a trapped ^{199}Hg$^+$ ion with a fractional frequency instability of $7{\cdot}10^{-15}$ and was realized by Diddams et al. in 2001 [77]. From that moment the need of ultra-stable and ultra-narrow probe sources was the major necessity to further reduce the frequency instability of optical clocks. In this respect a remarkable result was the development of an ultra-narrow source with sub-40 mHz linewidth at 1.5 µm [78]. Employing a silicon single-crystal cavity operating at 124 K in a vibration-insensitive chamber, it was possible to reduce the effect of the Brownian thermodynamical noise achieving a fractional frequency instability of $1{\cdot}10^{-16}$ corresponding to the aforementioned sub-40 mHz linewidth. Recently the state of the art has been achieved using a three-dimensional strontium optical lattice clock yielding a measurement precision of $5{\cdot}10^{-19}$ over one hour [79].

Frequency combs favored several other improvements in fields which are not treated in this thesis, such as coherent control of quantum dynamic processes [80], distance measurements [81], exoplanet searches and calibration of astronomical telescopes [82]. Also fields related to extreme temporal resolution instead of spectral resolution have benefited by the generation of OFCs, such as time-resolved spectroscopy and attosecond science to which the reader is referred to Ref. [83].

The next two subsections regard the field of molecular spectroscopy, which is closer to the thesis subject. The first deals with Comb-Assisted Molecular Spectroscopy, where a CW laser is locked to the comb source to be used as the probe source for spectroscopic measurements. This is the approach adopted in this thesis. The second is devoted to a brief overview over Direct Comb Spectroscopy, where the frequency comb itself is the probe laser source.

2.3.1 Comb-Assisted Spectroscopy

Comb-Assisted spectroscopy identifies a kind of spectroscopy where the OFC acts as a coherent link between a given frequency standard and the probe laser interacting with the absorbing medium, as sketched in Figure 2.6. When the beat-note signal f_{beat} between the probe laser and the first comb tooth is acquired, absolute frequency calibration comes straightforward. For instance, absolute calibration of the probe laser at the line-centre frequency

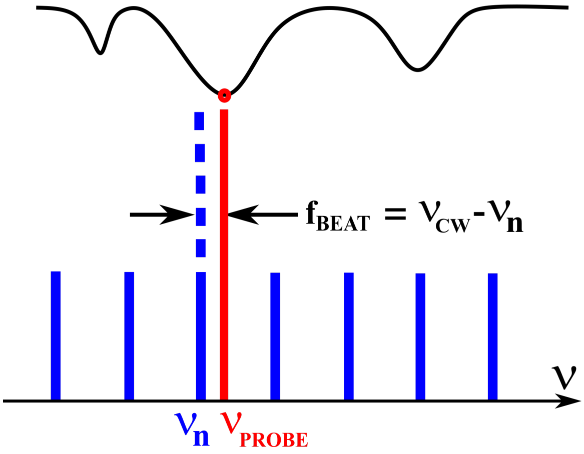

Figure 2.6: A sketch of the basic principle of Comb-Assisted Spectroscopy.

ν_0 of an absorption line is obtained by the following equation:

$$\nu_0 = nf_{rep} \pm f_{ceo} \pm f_{beat} \tag{2.10}$$

Eq.(2.10) shows the necessity in every comb-calibrated experiment to precisely know the order n of the comb mode, which can be identified using a commercial wavemeter with accuracy better than half of the comb mode spacing, and the correct signs of f_{ceo} and f_{beat}, that are determined by slightly varying f_{rep} and f_{ceo} and observing the shifts in f_{beat} in the free-running condition.

In Comb-Assisted spectroscopy, the OFC provides a stable absolute and repeatable frequency axis, enabling comparisons of spectroscopic data acquired in different laboratories at different times as well as with theoretical predictions and/or molecular databases. Nonetheless, the absolute calibration can be exploited for multiple spectra averaging to increase the Signal-to-Noise Ratio (SNR), ultimately affecting the precision of the retrieved spectroscopic parameters. Thanks to frequency combs for the first time accuracies at the kHz level in molecular absorption lines at environmental temperature have been achieved with simple and compact systems, whereas previous measurements where bound to accuracies of 10-100 MHz given by common wavemeters.

The most used approach to refer a measurement to a frequency comb consist in phase-locking the probe laser to the nearest comb mode. This offers the possibility of improving the spectral resolution transferring the temporal coherence of the comb, or of an ultra-stable master laser to which the comb is locked to, to a noisy laser. For instance, if the comb is equipped with an intra-cavity modulator it is possible to control its repetition frequency very fast [41], this enables the locking of the comb to a reference laser with ultra-high stability by means of a first phase-locking loop, enhancing the temporal coherence of the comb modes and thus reducing their linewidth. Then, with a second phase-locking loop, the coherence is transferred to the probe laser which inherits the properties of the master laser. In the previous schemes, the easiest way to tune the comb-referred probe laser is to tune the repetition rate of the comb, but this comes at the price of both limited tuning speed and range. Also changing the frequency offset of the phase-locking loops is not trivial, because of the the problem of aliasing when the beat-note between the probe laser and the nearest comb tooth overlaps the conjugated one. Schemes to solve the problem ambiguity has been proposed, such as the ones proposed by Jost *et al.* [84] or Schibli *et al.* [85], in particular the system proposed by Benkler *et al.* [86] removes this ambiguity in the "endless frequency shifting" approach where the carrier frequency of the comb is translated by an electro-optical crystal by programmed phase jump leaving the RF beat-note fixed. The latter solution is highly versatile, but comes at the price of a lesser accuracy of the frequency shift since does not depend on a RF synthesizer but to an applied voltage and the modulator response coefficient. A very elegant approach to tune the probe laser frequency is to exploit frequency actuators such as Electro-Optic Modulators (EOM) or Single-Sideband Modulators (SSM) to generate a tunable sideband of the laser that interacts with the absorbing sample, whereas the carrier is left fixed and phase-locked to the comb. The latter configurations are at the basis of very fast, accurate and sensitive schemes which are going to be described in Chapter 3, in particular the use of a SSM to tune the probe laser frequency is the approach adopted in this thesis for the spectroscopic investigations reported in Chapter 5.

The first absolute frequency measurements targeted transitions of molecular iodine and were performed in 2000 by Diddams et al. at JILA [46]. A femtosecond Ti:sapphire comb was used in conjunction with a He-Ne laser and a frequency doubled Nd:YAG laser to measure respectively the components of a_{13} of the 11-5 R(127) and a_{10} of the R(56) lines of $^{127}I_2$. Few months later Holzwarth et al. reported the first extensive study on the same molecule [87], using a widely tunable Nd:YAG laser which was locked on several I_2 saturated absorption lines. Absolute frequency measurements obtained exploiting a Ti:sapphire OFC a relative accuracy better than 10^{-11}. After those first applications other molecular targets have been chosen, for instance acetylene (C_2H_2). Accurate line centre retrieval for transition of this molecule have been selected as frequency standards in the 1.5 µm region, to be used by wavelength division multiplexing in telecommunication. Acetylene has several overtone bands in the region from 1530 nm to 1565 nm (the International Telecommunication Union C-band) where it shows a rather low sensitivity to effects causing frequency shifts, because of the linear and symmetric structure of the band itself. Thanks to the high intensity and the easiness of reaching the saturation condition of the acetylene lines, the $\nu_1 + \nu 3$ overtone band has become the most common frequency standard in the Near-IR. The first absolute frequency measurement of a C_2H_2 line was performed in 2003 by Hong et al. at the National Institute of Avanced Industrial Science (AIST) [88], where an acetylene stabilized diode laser was referred to a Ti:sapphire comb by frequency doubling the 1.5 μm radiation and the retrieved uncertainty on the centre frequency of the P(16) $\nu_1 + \nu 3$ line of $^{13}C_2H_2$ was at the 10^{-12} level.

Almost synchronously to the first molecular absolute frequency measurements, extensive and broad surveys have been performed assisted by frequency combs achieving unprecedented levels of accuracy over a large variety of molecular lines and samples. These surveys have the purpose to retrieve relevant spectroscopic constants of the absorption bands to increase the knowledge of the energy structure of molecules and redefine available spectroscopic databases, such as HITRAN [17]. Since most of the following investigation have used optical cavities to enhance the absorption signal, here a list is provided whereas details are given in the following chapters. The Doppler-free regime, in conjunction with the employment of a frequency comb, has been exploited for precise and accurate line centre frequency determinations. Measurements on quite intense lines have been reported in the Near-IR for the 10100-00000 band of acetilene [6], the 1010-0000 band of ammonia [89] and 101-000 band of water [90], for instance, and in the Mid-IR for the laser bands at 9 and 10 μm for carbon-oxide [91] and the 100-000 band of nitrous oxide [92]. For less intense lines, usually a linear absorption regime has been preferred, benefiting from the linear and repeatable frequency axis of the comb. Relevant examples are the absolute $^{12}C^{16}O_2$ transition frequency measurement of the 30013-00001 band from 1.6 to 7.8 μm with global uncertainties at the 10^{-11} level [93] and of the 3-0 band of CO near 1.57 μm with an accuracy better than 10^{-10} [94].

The OFC stable and reproducible frequency axis has been fundamental also for line-shape studies of the absorption profiles enabling testing of relativistic and quantum electrodynamic models. Indeed thanks to massive spectra averaging the SNR of absorption measurements is increased and possible departure from the commonly used Voigt profile, for instance due to collisional effects, can be analysed. An accurate recording and analysis of the line-shape profile is fundamental to retrieve spectroscopic parameters of high metrological quality, enabling, e.g., the comparison with *ab initio* calculations performed for light diatomic molecules such as H_2, HD and D_2. Those molecules in the Doppler-broadening regime are affected by line-shape effects, one way to avoid this is to measure the spectra at low pressure, but this is extremely challenging due to the typical low intensities of quadrupole transitions. The second approach is to record spectra at higher pressures and describe collisional effects with more sophisticated models than the Voigt profile [95]. Another important application requiring an accurate determination and analysis of the line-shape is Doppler-Broadening Thermometry (DBT). The Doppler effect links the line centre frequency of the absorption profile to the absolute thermodynamic temperature from the Doppler width [96]. This application is of main interest in this thesis and is going to be treated in details in Chapter 5.

To conclude this subsection, we report Comb-Assisted results obtained in the Mid:IR with Quantum-Cascade Lasers (QCLs), that have enabled the investigation of the region from 4 to 11µm, the fingerprinting region. Referencing a QCL to an OFC enables comb-assisted measurements, making possible absolute frequency measurements with high sensitivity for a tons of molecular transitions never tested before. The easiest approach to perform such measurements was to link a QCL to a visible or NIR comb using nonlinear optics. The link is obtained for example by SFG or using an OPO. An interesting example of SFG link is reported in Ref [97] where an Er:doped fibre OFC with two branches, one centred at 1.55 µm and the other a SC from 1 to 2.2 µm was used to generate SFG is between the QCL and the output of the OFC centred at 1.55 µm, synthesizing a frequency shifted comb around 1.14 µm. The shifted comb was made to beat with the SC branch of the original OFC with the advantage of being f_{ceo}-free. By tuning the repetition frequency of the comb by 29 kHz the QCL was made scanning nearly 20 GHz and the line centre frequencies of the different absorption lines retrieved show a kHz-level precision. Another example of Mid-IR Comb-Assisted absolute frequency measurements was performed for methane at 3.39 µm in the sub-Doppler regime [98] where a CW singly resonant OPO, pumped by a Nd:YAG laser at 1064 nm, synthesized an idler and a signal represented by the OPO relation $\nu_p = \nu_i + \nu_s$ where p stands for pump, s for signal and i for idler. From the resonant OPO, a widely tunable idler was generated in the Mid-IR maintaining the signal in the Near-IR region and referred to an OFC for absolute frequency calibration.

2.3.2 Direct-Comb Spectroscopy

The focus of this subsection is on the experimental configurations employing a frequency comb as the probe laser source for spectroscopic measurements, referred to as Direct-Comb Spectroscopy. In this kind of spectroscopy the advantage consists in the large bandwidth of OFCs covering a variety of spectral regions, some of them not yet covered by commercial lasers, enabling massive parallel detections useful for multiple trace gas detection, for instance.

One of the first experiments employing directly a mode-locked laser for Cavity Enhanced Absorption Spectroscopy was reported by Gherman and Romanini in Ref. [99]. Effective injections of the mode-locked laser into a cavity with finesse ∼420 have been studied. The spectrometer has been employed for a scan over a weak overtone band of acetylene with a span of 4 nm and 0.2 cm^{-1} spectral separation acquired in just 40 ms, which is the main strength of the approach coming at the price of a limited sensitivity.

After the previous demonstration, several techniques have been developed employing directly frequency combs and are summarized in this paragraph, they are namely: Spectrally Dispersed Detection, Fourier-Transform, Dual-Comb and Vernier spectroscopy.

In Spectrally Dispersed detection the various comb modes are dispersed onto a digital two-dimensional array camera by means of a particular etalon called Virtually Imagined Phased Array (VIPA). This kind of etalon spatially separates the different modes in one direction and, with the combination of a lower dispersion grating in the orthogonal direction, it is possible to capture a large bandwidth covering the region from 5 to 10 THz, within a single measurement. This technique enables single comb tooth resolution if the teeth are separated at least 1 GHz, achievable using filtering schemes such as Vernier filtering described below for instance. Spectrally Dispersed detection leads to fast and accurate spectroscopic determinations when conjugated with optical cavities. An example is the high-precision absorption measurement of $H^{13}C^{14}N$ near 1543 nm with absolute frequency accuracy of 2 kHz and SNR of ∼400 in a measurement time of 8.2 s [100].

In Fourier Transform spectroscopy an OFC is coupled into a high finesse optical cavity. The transmitted output is sent to a a fast-scanning Michelson interferometer and the two output beat-notes are collected by a balanced photodetector. The balancing enables the achievement of the quantum noise limit for broadband spectra as large as 30 nm and acquired in few seconds, as reported in Ref. [101]. Single tooth resolution has been demonstrated in Ref. [102] increasing the spectral resolution, but one of the main disadvantage of the technique is the system complexity mainly related to the mechanical fast-scanning interferometer.

Dual-Comb spectroscopy employs two OFCs with repetition rates slightly detuned from each other, for example by 1 kHz. One frequency comb acts as the probe laser interacting with the sample, whereas the other takes the role of the reference. The detune of the two OFCs enables the acquisition of the multiple heterodyne beating signals between the different pairs of each comb modes. By Fourier transform it is possible to obtain the amplitude and phase spectrum within a fast measurements that does not require any mechanical delay slits. While this technique provides a broadband and relatively fast measurement with single tooth resolution employing a single photodetector, its spectral resolution depends on the measurement time and also it cannot be easily conjugated with enhancement cavities. For a detailed review the reader is referred to Ref. [103], where the state of the art in the Near-IR is described, together with recent advancements in the Mid and Far-IR.

Vernier spectroscopy exploits an enhancement cavity, in which the sample under test is contained, to filter the frequency comb. This is done by an active stabilization of the mismatch between the comb repetition frequency and the cavity free spectral range, to let only a single tooth coupled inside the cavity in a chosen time interval. This technique is particularly useful when there is the necessity to filter actively the comb modes, increasing their frequency separation and giving the chance to resolve the single tooth. Recently, broadband spectra covering more than 2000 cm^{-1} around 12500 cm^{-1} with a high number of spectral points, more than 30000, acquired in the second time scale have been demonstrated and employed for the observation of the entire A-band of oxigen and the $3\nu+\delta$ band of water vapor near 800 nm in ambient air [104].

Chapter 3

Cavity Enhanced Techniques for High-Sensitivity Measurements

The chapter concerns cavity enhanced techniques for molecular absorption spectroscopy. It is divided into three sections: the first is a brief introduction to optical cavities, showing the fundamental enhancement properties that are useful in molecular spectroscopy. The second section regards Cavity Enhanced Absorption Spectroscopy (CEAS) techniques, giving an overview of the different approaches developed over the past few decades together with their relevant features. In particular it treats the direct cavity transmission CEAS where the laser is tightly locked to the optical cavity, approach that has been adopted in this thesis for Comb-Assisted CEAS, as presented in Chapter 4. The last section regards Cavity Ring Down Spectroscopy (CRDS), starting from the principles of the technique and then describing the different CRDS implementations and the state of the art. A CRD spectrometer has been employed in the thesis in combination with an optical frequency comb for absolute frequency determinations and Doppler-Broadening primary Thermometry, as shown in Chapter 5.

3.1 Optical Cavities: An Introduction

Molecular absorption spectroscopy has been deeply used over the past few decades for trace gas sensing, namely for the detection of molecular samples at very low concentration levels, down to the few parts per million level. Because low concentrations imply low absorption signals, one way to increase it is to exploit the enhancement in the interaction length provided by multi-pass cells or optical cavities. Typically, multi-pass cells increase the interaction length up to two orders of magnitude, whereas with optical cavities up to five orders of magnitude have been demonstrated. To properly describe cavity enhanced techniques, it is fundamental to give a detailed analysis of optical cavities.

Optical cavities are usually referred to as optical resonators because the incoming light excites the electromagnetic (e.m.) field inside the cavity only at specific frequencies, called resonances. At those frequencies the intracavity field is significantly amplified, thus giving the chance to study nonlinear regimes of interaction between the gas and light. The properties of these cavities can be derived from the theory of Fabry-Perot interferometers, indeed they are usually referred to as Fabry-Perot optical resonators.

The following discussion is divided in three subsections: the first retrieve the transmission spectrum of an optical cavity, the second is focused on the enhancement factors in both the absorption interaction length and intracavity power and the last describes the cavity response time and injection efficiency.

3.1.1 Steady-state Coupling

We begin the analytical treatment considering the steady-state condition, and as a sake of simplicity, an empty (refractive index $n_0 = 1$) and symmetric linear cavity made of two mirrors at a distance L_C aligned along a z optical axis, as represented in Figure 3.1. A complete and general treatment about passive optical resonators of different geometries is given in [105], for instance.

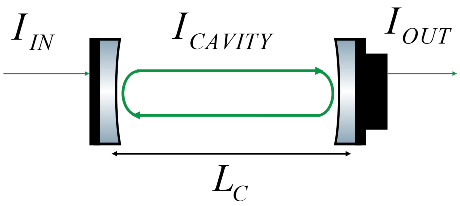

Figure 3.1: Schematic of a symmetric linear optical cavity made of two mirrors facing each other at a distance L_C.

The cavity admits only electromagnetic fields which fulfil the boundary conditions imposed by the cavity mirrors, those fields are called Transverse Electro-Magnetic modes TEM$_{mn}$ (where the labels m and n are positive integers) and possess a spatial distribution that corresponds to a linear combination of Gauss-Hermite modes. The electric field amplitude, as calculated for instance in Ref. [106], reads as follows:

$$E_{mn} = E_0 \frac{w_0}{w(z)} H_m\left(\frac{\sqrt{2}x}{w(z)}\right) H_n\left(\frac{\sqrt{2}y}{w(z)}\right) e^{-\frac{r^2}{w(z)^2}+i\frac{kr^2}{2R(z)}-i(m+n+1)\arctan\frac{z}{z_R}+i(kz-\omega t)} \tag{3.1}$$

where z is the optical axis, x and y are the transversal coordinates related by the mirror radius of curvature $r^2 = x^2+y^2$, $H_{m,n}$ are the m, n-order Hermite polynomials, $R(z) = z\left(1 + \left(\frac{z_R}{z}\right)^2\right)$ is the curvature radius of the wavefront and $w(z) = w_0\sqrt{1+\left(\frac{z}{z_R}\right)^2}$ is the beam radius. z_R is called Rayleigh range and is determined by the boundary condition that requires the curvature radius R of the wavefront at the mirror's position to be equal to the radius of curvature r of the mirror itself:

$$R\left(\frac{L_C}{2}\right) = \frac{L_C}{2}\left(1 + \frac{4z_R^2}{L_C^2}\right) = r \tag{3.2}$$

so that:

$$z_R = \frac{L_C}{2}\sqrt{\frac{2r}{L_C} - 1} \tag{3.3}$$

At a distance $z = z_R$ the beam waist is $\sqrt{2}w_0$. The beam waist w_0 is then deduced from the Rayleigh range:

$$w_0 = \sqrt{\frac{\lambda z_R}{\pi}} \tag{3.4}$$

Notice that Eq.(3.3) has a real solution if $L_C \leq 2r$ which is a condition for stable light propagation inside the resonator.

We are interested in obtaining the cavity transmission as a function of frequency from a steady-state condition of the light inside the resonator, which corresponds to the establishment of a standing wave between the two mirrors. Let us proceed with the case of a cavity where the TEM$_{00}$ mode is excited by an incoming monochromatic e.m. field propagating along the z direction:

$$E_{in}(x, y, z, t) = E_0(x, y, z)e^{i(\omega t - kz)} \tag{3.5}$$

where $E_0 = (x, y, z)$ is a Gaussian profile, that is typical for TEM$_{00}$. The TEM$_{00}$ mode, and in general every TEM$_{nm}$ mode, maintains the same spatial distribution after propagations and reflections inside the cavity, except for a small loss transmitted at every mirror bounce that happens after a round-trip distance $2L_C$. Considering only the temporal dependence of the electric field at a position $z > L_C$, we can write the transmitted output of the empty cavity after n round-trip reflections as:

$$E_{out} = \sum_{k=0}^{n} \mathbf{t}^2\mathbf{r}^{2k} E_{in}(t - kt_0) \tag{3.6}$$

where t_0 is a retardation factor defined as $t_0 = \frac{2L_C}{c}$ corresponding to the round-trip time and $\mathbf{r}$ and $\mathbf{t}$ are the field reflection and transmission coefficient respectively. By Fourier transform of Eq.(3.6) and using the intensity coefficients R and T (where $R = \mathbf{r}^2$ e $T = \mathbf{t}^2$), the frequency spectrum is given by:

$$\begin{aligned} E_{out}(\omega) &= \int_{-\infty}^{+\infty} \sum_{k=0}^{n} TR^k E_{in}(t - kt_0) e^{-i\omega t} dt \\ &= \sum_{k=0}^{n} TR^k e^{-ik\omega t_0} E_{in}(\omega) \\ &= TE_{in}(\omega) \sum_{k=0}^{n} (Re^{i\omega t_0})^k \end{aligned} \tag{3.7}$$

where the geometric series for $n \to +\infty$ can be rewritten as:

$$\sum_{k=0}^{n} (Re^{i\omega t_0})^k = \frac{1}{1 - Re^{-i\omega t_0}} \tag{3.8}$$

since $R \leq 1$. The transmitted intensity spectrum is then obtained from the modulus square $|E_{out}(\omega)|^2$:

$$I_{out}(\omega) = \left\{ \frac{T^2}{(1-R)^2 + 4R \sin^2\left(\frac{\omega t_0}{2}\right)} \right\} I_{in}(\omega) \tag{3.9}$$

where the function between parenthesis is the Airy function corresponding to the cavity transfer function. At resonance the phase term ωt_0 is a multiple of 2π and the transmitted intensity is:

$$I_{out,res}(\omega) = \frac{T^2}{(1-R)^2} I_{in}(\omega) \tag{3.10}$$

which, in the ideal case where the mirror losses are negligible ($T \simeq 1 - R$), shows that the cavity transmission may approach 100%. The description can be easily generalized to the case of mirrors with different reflectivity placing $R = \sqrt{R_1 R_2}$ and $T = \sqrt{T_1 T_2}$.

Equation 3.9 represents a series of evenly spaced maxima, forming a comb-like structure, referred to as cavity modes, depicted in Figure 3.2 for different R values. The maxima occurs when the condition $\omega t_0 = 2l\pi$ is fulfilled, where l is an integer number, leading to the the expression for the resonant frequencies:

$$\nu_l = l \frac{c}{2L_C} \tag{3.11}$$

spaced by the so-called cavity Free-Spectral-Range (FSR):

$$FSR = \frac{c}{2L_C} \tag{3.12}$$

The integer l in Eq.(3.11) is the order of the resonant mode and stands for longitudinal, it represents how many wavelengths are in a round-trip.

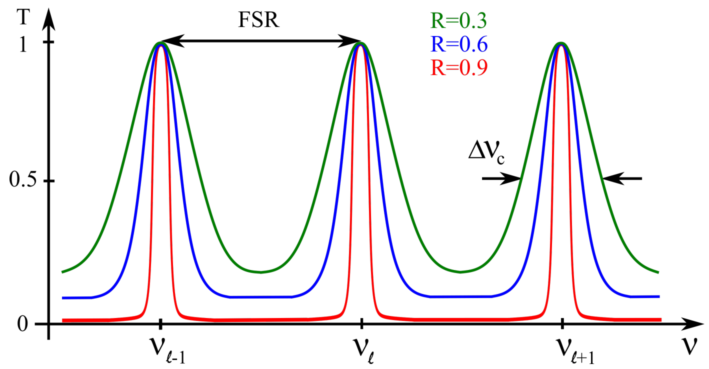

Figure 3.2: Transmitted intensity from the cavity for different R values. The mode spacing is given by the Free-Spectral-Range (FSR) and the mode full-width is represented by $\Delta\nu_C$.

The resonance condition corresponds to the establishment of a stading wave inside the cavity and is possible if $2L_C = l\lambda$, which means that the mirror distance has to be an integer multiple of half the wavelength $L_C = l\lambda/2$. Close to a resonance maximum, the transmitted intensity profile is well approximated by a Lorentzian function and the Full Width at Half Maximum (FWHM) of the cavity mode has the following expression:

$$\Delta\nu_C = \frac{c}{2\pi L_C}\frac{1-R}{\sqrt{R}} = \frac{FSR}{\pi}\frac{1-R}{\sqrt{R}} \tag{3.13}$$

The optical cavity acts as a frequency filter until a value f_C equal to half of its FWHM:

$$f_C = \frac{\Delta\nu_C}{2} \tag{3.14}$$

This cavity can be sketched in an electric-like picture as a low-pass filter adding a pole at frequency f_C.

Is possible to define the cavity Finesse F as:

$$F = \frac{FSR}{\Delta\nu_C} = \frac{\pi\sqrt{R}}{1-R} \tag{3.15}$$

which is an indicator of how the cavity modes are narrow compared to the mode separation, in particular the higher is the mirrors reflectivity the narrower are the cavity modes and the higher is the finesse. When light is coupled efficiently inside the optical resonator, the intra-cavity power builds up and the maximum circulating power is estimated by the product of the incident power and the cavity finesse:

$$I_{cavity} \simeq I_{in}F \tag{3.16}$$

Together with the finesse, another parameter used to compare optical cavities is the quality factor Q defined as:

$$Q = \frac{\nu}{\Delta\nu_C} = \frac{\nu}{FSR}F \tag{3.17}$$

The quality factor, in general, is a parameter of every resonant system and represents the degree of energy stored in the resonator with respect to the energy lost per round-trip. Indeed it is defined as Q=[2π(energy stored)]/[energy lost per round-trip].

The previous treatment was based on a perfect mode-matching of the input light beam with the fundamental TEM$_{00}$ cavity. Unfortunately this condition is not always achieved in reality and higher transverse modes are excited by the input beam at different frequencies with respect to the fundamental resonances. In particular the following expression is valid for the frequencies of the different transverse modes:

$$\nu_{lmn} = \frac{c}{2L_C}\left[l + \frac{m+n+1}{\pi}\arccos\left(1 - \frac{L_C}{r}\right)\right] \tag{3.18}$$

where in this case r stands for the radius of curvature of the mirrors. Experimentally high order transverse modes excitation is clearly visible when the alignment of the incoming beam is not perfectly mode matched with the fundamental TEM$_{00}$.

Another important fact to be pointed out regards the cavity free spectral range. In the previous description it has been derived as a constant separation value for the different longitudinal modes: this is true only in the absence of dispersion. Actually, dispersion occurs in every cavity because of the mirrors coating and of the frequency dependent refractive index of the gas medium, the two lead to a frequency dependent $FSR(\omega)$. The reader is referred, e.g., to Ref. [107] for an experimental characterisation of $FSR(\omega)$ using an optical frequency comb.

3.1.2 Cavity Enhancement Factor

The main reason to resort to an optical cavity is due to the enhancement of the interaction length between the resonating light and any absorbing medium inside the cavity. Intra-cavity absorption happens at each round-trip and can be calculated using the Lambert-Beer law for every propagation interval. The analytical description for the transmitted intensity given in the previous subsection can be extended to the case of an absorbing medium present inside the cavity by multiplying the intensity reflection coefficient R by the factor $e^{-\alpha(\omega)L_C}$, which accounts for the medium absorption as a function of frequency. The purpose of this analysis is to quantify the enhancement factor for the interaction length. Including intra-cavity absorption, Eq.(3.9) becomes:

$$I_{out}(\omega) = \frac{T^2 e^{-\alpha(\omega)L_C}}{\left(1 - Re^{-\alpha(\omega)L_C}\right)^2 + 4Re^{-\alpha(\omega)L_C}\sin^2\left(\frac{\omega t_0}{2}\right)} I_{in}(\omega) \tag{3.19}$$

At resonance ($\omega t_0 \propto 2\pi$) the transmitted intensity is:

$$I_{out,res}(\omega) = \frac{T^2 e^{-\alpha(\omega)L_C}}{\left(1 - Re^{-\alpha(\omega)L_C}\right)^2} I_{in}(\omega) \tag{3.20}$$

In the approximation of weakly absorbing media $\alpha(\omega)L_C << 1$ the Lambert-Beer law can be linearised in $1 - \alpha(\omega)L_C$. Then it is possible to evaluate the relative intensity variation as:

$$\frac{\Delta I}{I_{in}} = \frac{I_{in} - I_{out}}{I_{in}} = 1 - \frac{T^2}{(1-R)^2}\left(1 - \frac{2\alpha L_C}{1-R}\right) \simeq \frac{2\alpha L_C}{1-R} \tag{3.21}$$

where negligible mirror losses have been supposed so that $T \simeq 1 - R$.

The cavity enhancement factor is clearly visible in the case of high finesse cavities, where the mirror reflectivity approaches 1, and $\frac{1}{1-R} \approx F$. Eq.(3.21) can be rewritten as:

$$\frac{\Delta I}{I_{in}} \simeq \alpha L_C \frac{2F}{\pi} = \alpha L_{eff,res} \tag{3.22}$$

where an effective interaction length as a function of the finesse has been introduced:

$$L_{eff,res} = \frac{2F}{\pi} L_C \tag{3.23}$$

As compared to the single pass between the two mirrors at a distance L_C, the interaction length is increased by a factor that is close to the finesse value. For a finesse of more than 10^4, achievable with high reflectivity mirrors in the visible and Near-IR regions, and cavity lengths close to 1 m the effective interaction length reaches the km scale. Let us point out that the interaction length enhancement factor $2F/\pi$ can be achieved only when a sufficiently monochromatic source is actively locked to the maximum of the cavity mode so as to exhibit a linewidth well below $\Delta\nu_C$. When the input source is highly BroadBand (BB) such as a LED or a lamp it is possible to demonstrate that the effective absorption interaction length is enhanced by a factor that is half that of Eq.(3.23) [108], namely by:

$$L_{eff,BB} = \frac{1}{1-R} L_C \simeq \frac{F}{\pi} L_C = \frac{L_{eff,res}}{2} \tag{3.24}$$

In between the two limit cases of a pure monochromatic and of a very broadband source, intermediate ones are present and described by an enhancement $\beta F/\pi$, where β ranges from 1 to 2 depending on the light source and the injection scheme employed [108]. An example is the case of an active locking of the laser to the cavity not tightly enough to shrink the laser linewidth below $\Delta\nu_C$, in this case the average intensity transmitted from the cavity depends on the spectral distribution of the laser with respect to the mode profile, which undergoes changes both in its peak transmission and width as a function of the sample absorption and cavity losses leading to a β values less than 2.

Besides an interaction length enhancement, a cavity also increases the intra-cavity power. From Eq.(3.16), a high finesse cavity is able to provide intra-cavity powers reaching the Watt or kilo-Watt level starting from few milli-Watts. Remembering from Chapter 1 that the Lamb-dip of an absorption line is a contrast feature over the linear absorption profile that depends on the interacting field intensity, with a high finesse cavity both the linear absorption and the intensity are enhanced, thus it makes possible the achievement of the saturation condition even of weak molecular absorption lines.

3.1.3 Transient Coupling

In the previous subsection we have considered the properties of optical cavities in the steady state condition, in particular when the light source is monochromatic or very narrow and is maintained on resonance in a stationary excitation condition. As shown in Eq.(3.24), when the model is applied to broadband sources or when the laser is not efficiently maintained on the resonance condition, the optical cavity has different characteristics. If a tight lock of the input source with the cavity cannot be established, usually the resonance condition is obtained in a transitory way, for example by sweeping the optical frequency of the source through the cavity resonances or vice-versa. In this condition, the cavity temporal response has to be taken into account [108]. This characteristic transient time is the cavity response time called Ring Down time (RD) τ.

As discussed above, the build up condition takes place at resonance, where the input field sums up coherently with the intra-cavity field until a point where field coupling and decoupling are balanced and a stationary condition is eventually reached. If the input optical frequency is slightly detuned above or below the resonance condition, there is a small phase difference with the field injected one round trip earlier, and this shift cumulates at every round trip. What happens is that fields injections separated in time by a few round-trips would interfere constructively, whereas fields separated by many round-trip times would interfere destructively. After longer times constructive interference reappears leading to an oscillatory behaviour of the intra-cavity intensity until a steady state condition is established, but at a lower build up level with respect to the resonance condition. The nature of these transient oscillations before reaching the steady state condition can be considered as a beat-note between the incoming field and the resonance frequency.

Let us now consider the case of a transient coupling of a laser into a cavity with mode-width $\Delta\nu_C$, which may occur either in the case where the laser frequency is scanned over a fixed cavity mode or vice-versa. In the first case, we introduce the scanning speed of the laser W in Hz/s, corresponding to the frequency change per unit of time. Three transient injection regimes can be identified and classified as a function of the scanning speed, as represented in Figure 3.3: the adiabatic, the ringing and the impulsive regimes. The adiabatic condition takes place if W is low enough that a full build up may occur at every frequency to achieve the stationary regime. This happens when the time taken by the field to be tuned across the cavity resonance $\Delta\nu_C/W$ is much longer than the cavity response time τ:

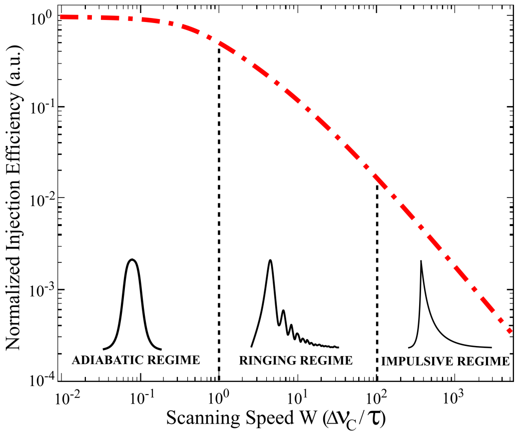

Figure 3.3: Cavity transient response as a function of the laser tuning speed W. Three regimes can be differentiated: the adiabatic regime, the ringing regime and the impulsive regime.

$$\frac{\Delta\nu_C}{W} >> \tau \tag{3.25}$$

In this situation, by conversion of the tuning time into frequency by means of W it is possible to directly retrieve the cavity mode profile. The ringing regime, instead, is obtained for higher W values typically close to:

$$\frac{\Delta\nu_C}{W} \simeq \tau \tag{3.26}$$

When approaching the resonance condition, the intra-cavity field starts to build up but, as it gets quickly de-phased with respect to the frequency-sweeping input field, the build up behaviour is quenched by destructive interference. A beating is established between the input field and the intra-cavity field that is undergoing an exponential decay, generating a profile affected by a ringing behaviour. The last regime is the impulsive regime, which is achieved in the limit of very short crossing time, or equivalently high scanning speed:

$$\frac{\Delta\nu_C}{W} << \tau \tag{3.27}$$

With very high scanning speed there is a short build up time and the output reaches a small amplitude value before decreasing quickly with a single-like exponential decay behaviour superimposed by fast and negligible oscillations.

To conclude this subsection, usually in practice the resonance condition is achieved modulating the cavity length, by mounting a cavity mirror on a piezoelectric transducer, leaving the input source frequency fixed. The previous description is easily converted to this case just by converting the scanning speed W into the mirror velocity v using the relation:

$$\frac{v}{L_C} = \frac{W}{\nu} \tag{3.28}$$

then again the three previous regimes are identified. The growing phase shift in this situation is given by the Doppler shift of the wave at each reflection from the moving mirror. This Doppler shift effect is going to be treated in details in Chapter 5 since it influences the spectral analysis of the ring down events and thus of the retrieved absorption profile.

3.2 Cavity Enhanced Absorption Spectroscopy

With Cavity Enhanced Absorption Spectroscopy (CEAS) one usually intends a variety of absorption spectroscopy methods in which optical cavities are used to improve the interaction length of light with matter. In this thesis we are going to use the term CEAS in a narrower sense referring to a stationary field coupling of a laser to the cavity and to an absorption measurement based on the light transmitted through it. In this way we separate Cavity Ring Down Spectroscopy (CRDS), based on the measurement of the time dependence of the transmitted light, from the previous group of techniques. CRDS is going to be presented in Section 3.3.

The following subsection is an overview of different CEAS techniques with a focus on their basic principles. In particular we pay attention to the case where CEAS is exploited together with a tight locking of the laser to the cavity as this is the approach followed in Chapter 4 to probe C_2H_2 Lamb-dips in the Sub-Doppler regime assisted by a frequency comb.

3.2.1 An Overview of CEAS Techniques

Since 1962 the properties of optical resonators, such as Fabry-Perot etalons, have been studied focusing in particular on the possibility to achieve frequency selectivity because of their narrow resonances associated with specific intra-cavity field distributions. One of the first applications regarding the acquisition of high resolution spectra has been demonstrated by Jackson in Ref. [109] probing the electronic transitions of Barium employing a confocal cavity. After the first demonstrations, almost two decades passed before new applications and experimental configurations were stimulated by the manufacturing of low loss dielectric super-mirrors [110]. From that moment, high finesse optical cavities were recognised as powerful tools in high-sensitivity molecular absorption spectroscopy and several cavity enhanced methods were developed.

As mentioned before, in this thesis the term CEAS is considered in its narrow sense indicating the techniques in which the transmitted light from the cavity is recorded. In particular we consider systems in which the probe laser is a single-frequency laser in the Near-IR with few examples in the Mid-IR. For a detailed treatment considering a broader range of sources and approaches the reader is referred to [108]. We start with a description of the basic principles and first implementations of the most known CEAS techniques, whereas their recent advancements and state of the art results are reviewed in the last subsection.

One of the major difficulties in CEAS regards the injection of light into the very narrow widths of the high finesse cavity modes. Moreover the cavity mode acts as a frequency discriminator, causing frequency noise and relative jitter of the input laser with respect to the cavity to be converted into amplitude fluctuations [111], influencing the stability of the transmitted signal. To deal with this intrinsic problem, several CEAS approaches have been proposed to reduce the impact of input noises that can be grouped in two categories: one where the laser frequency is swept over the cavity modes, the other in which the laser frequency is actively locked on cavity resonances.

The first category of techniques consists of quickly sweeping the laser frequency through several cavity resonances and monitoring the transmitted signal with a slower photodetector with respect to the sweep-time, so that the cavity output is integrated and averaged. Those techniques were the first CEAS approaches developed since 1998, based on relatively simple system configurations, and are referred to as Integrated Cavity Output Spectroscopy (ICOS). Averaging reduces the amplitude noise of the laser source caused by the cavity conversion of the frequency noise, but integration of the mode profile instead of the precise peak transmission leads to an equivalent absorption that is half of that achieved when the source is maintained actively on resonance, as reported in Eq.(3.23) and Eq.(3.24). On of the issues of ICOS is the non-uniform excitation of high order cavity modes because the effective finesse of the different transverse modes is affected by inhomogeneities and diffraction losses of the cavity mirrors, which alters in a periodic way the cavity enhancement factor and consequently the transmitted spectrum as a function of the cavity FSR. A possible way to reduce the impact of this periodic cavity mode structure is to excite a huge number of high-order transverse modes employing cavity mirrors with large radius of curvature and non-confocal cavity geometries combined with beams far from the mode-matching condition. This approach proposed by

Paul in 2001 was named off-axis ICOS [112]. The residual cavity mode structure is then washed out by several averaging while the cavity length is modulated. More recent solutions exploit degenerate modes configurations and their best performances are reported in the next subsection.

The second category regards optical or electronic locking of the laser frequency to cavity resonances to shrink the laser linewidth and reduce the impact of the laser frequency noise. In this frame there are techniques such as Optical Feedback Cavity Enhanced Spectroscopy (OF-CEAS), direct-cavity-transmission CEAS by means of the active locking of the laser to the cavity and Noise Immune Cavity Enhanced Optical Heterodyne Molecular Spectroscopy (NICE-OHMS).

Regarding Optical Feedback (OF) approaches, it was recognised since 1987 that optical feedback coupling of diode lasers into cavities leads to linewidth narrowing [113] and that OF locking can be employed for CEAS investigations. Optimal couplings of laser radiation through OF were obtained using simple V-shaped cavity geometries producing selective optical feedback. The reason why V-shaped cavities are preferred for OF is that when using high finesse confocal cavities, the modes are so narrow that is difficult to have high transverse modes degeneracy to obtain relatively good OF. Degeneracy of transverse modes exists only in a V-trajectory made by the superposition of such modes at resonance, but this condition is very difficult to achieve. Whereas in V-shape cavities only the fundamental TEM_{00} mode is needed to obtain good OF even without positioning the mirrors at the confocal distance, which is a fundamental advantage to set up cavities with small intra-cavity sample volumes [114]. The first implementations of OF with V-shaped cavities employed long pulse operation of DFB lasers and simple detection schemes, the main weaknesses being the poor frequency stability and the absence of control for the OF phase, leading to modest performances [115]. After few years, Morville *et al.* proposed an OF-CEAS scheme were the laser frequency is linearly swept over the TEM_{00} modes of a V-shaped cavity controlling actively the phase of the OF, obtaining efficient linewidth narrowing of the input source and reproducible injections [114]. The main advantage of that scheme was the acquisition of high quality spectra, sampled equidistantly in frequency, with relatively fast diode laser scans using small sample volume systems. Over the past decade, OF-CEAS has seen different application in the Mid:IR thanks to the good performances achieved, for example when using Quantum-Cascade lasers [116].

Among electronic locking techniques, one of the best and most widely known is Pound-Drever-Hall (PDH) locking (treated in detail in Appendix B). Here we give a brief description: it consists in adding to the laser two modulation sidebands to generate a first derivative like error signal after acquisition and demodulation of the reflected light from the cavity. The error signal is used to lock the laser frequency to the cavity resonance by means of a proper feedback loop [117]. Typical PDH locking schemes employ two feedback loops, one for a prior stabilization of the cavity length, usually with low bandwidth, to account for cavity drifts and the second loop with high bandwidth to lock the laser frequency to the cavity resonance. In this thesis we have employed PDH locking of an Extended Cavity Diode Laser (ECDL) to a high finesse cavity and we demonstrated a locking scheme with just a single feedback loop using a Single Sideband Modulator (SSM), described in Appendix C, as the only frequency actuator. Thanks to PDH it is possible to obtain a tight lock of the laser, in particular the higher is the bandwidth of the feedback loop the more effective is the laser frequency noise reduction relatively to the cavity resonance. In this way the spectral resolution that can be achieved is determined by the cavity mode width that for high finesse cavities is in the kHz range. As we are going to show in Chapter 4, if the low frequency noise and the residual amplitude noise of the laser do not restrict excessively the detection performances of the system, is possible to directly measure the DC transmitted output of the cavity and record the molecular absorption of the sample inside the cavity. Alternatively, to reduce the impact of low frequency noise an AC detection is possible by modulating the cavity length around the molecular absorption resonance and using a lock-in derivative line shape recovery process [118]. For the length modulation one cavity mirror is mounted on a PieZoelectric Transducer (PZT) and the laser tracks the modulation, usually limited to the audio range due to mechanical resonances of the PZT and mirror assembly. In this way a non-zero dispersive signal is obtained after demodulation at the PZT-frequency only in the presence of an absorption signal washing out other noise sources. One strict requirement for the application of DC or AC direct cavity transmission CEAS measurements is a super-tight lock of the laser to the cavity.

A scheme showing close to the shot-noise-limited performances and immunity to laser amplitude and frequency noise was called Noise Immune Cavity Enhanced Optical Heterodyne Molecular Spectroscopy (NICE-OHMS). NICE-OHMS, introduced by Ye *et al.* in 1998 [118], is based on a tight locking of the laser to an enhancement cavity combined with frequency modulation (FM) at a frequency equal to the cavity FSR. Modulating the phase of the laser with low modulation index and at frequencies typically of the order of hundreds of MHz, where the instrumental noise is lower, generates two sidebands equally separated from the carrier by the modulation frequency, referred to as a FM-triplet. The frequency modulated signal at the cavity output is the sum of two beat-note signals between the carrier and the two sidebands respectively. In the absence of absorbers, the two beat-note signals cancel out since the two sidebands are out of phase, whereas absorption, dispersion or any changes in one of the two sidebands causes an unbalance of the two signals which is detectable. Interestingly, the advantage of modulation at the FSR frequency comes from the fact that the carrier and the phase-modulated sidebands are transmitted through the cavity in the same way, so that any residual frequency noise of the laser, converted into amplitude noise by the cavity, is equally present in the two beat signals and will not affect the detected demodulated signal. This technique has provided extraordinary results in the sub-Doppler regime with fixed frequency lasers [118], unfortunately in the Doppler broadening regime where there is the need of relatively large spectral tuning of the input source, the approach is mainly limited by interference fringes. Also with respect to other CEAS techniques, NICE-OHMS requires sophisticated radio-frequency electronics for the frequency locking loops, for instance for the frequency locking of the frequency-modulated sidebands at the FSR frequency, and the system complexity is one of the main technological hurdle.

3.2.2 CEAS: Performances and State of the Art

This subsection, after an introduction to typically used figures of merit for the sensitivity of CEAS systems, provides a focus on their state of the art.

To quantify the minimum absorption coefficient α_{min} that a given spectrometer is able to appreciate, one may observe that for αL_{eff}¡¡1 the Lambert-Beer law can be linearised and written as:

$$\frac{\Delta I}{I_{in}} \simeq \alpha L_{eff} = \alpha L_C \frac{\beta F}{\pi} \tag{3.29}$$

where ΔI is the intensity drop given by the absorption medium. The minimum detectable absorption, also referred to as the Limit Of Detection (LOD), can thus be calculated as:

$$\alpha_{min} = \frac{1}{L_{eff}} \frac{\delta I}{I} = \frac{\pi}{\beta F L_C} \frac{\delta I}{I} \tag{3.30}$$

where $\frac{\delta I}{I}$ is the root-mean-square of the relative intensity noise for a given measurement time. In a condition where the probe laser has no amplitude noise beyond its intrinsic quantum fluctuations, α_{min} is given by the shot-noise limit expression:

$$\alpha_{shot-noise} = \frac{\pi}{2FL_C} \sqrt{\frac{2eB}{\eta P_0}} \tag{3.31}$$

where B is the detection bandwidth, η the photodetector responsivity and P_0 the total optical power. Since the shot-noise limit is not easily reached in the different CEAS configurations, a way to compare the performances in terms of sensitivity of the absorption axis is to refer to the Noise Equivalent Absorption (NEA) coefficient, defined as the smallest absorption coefficient that can be detected during a measurement lasting 1 s, with units cm^{-1} Hz$^{-1/2}$. Considering a set of measurement affected only by white noise, the

LOD for a given integration period T can be determined by the NEA value as:

$$LOD = NEA\frac{1}{\sqrt{T}} \tag{3.32}$$

Unfortunately Eq.(3.32) is valid only in the presence of white noise sources, whereas when other noise mechanisms are present, such as flicker noise, the LOD deviates from the $1/\sqrt{T}$ law, especially at longer time scales, hampering the advantage of more prolonged averaging. We have to point out that a full characterisation of the system through the Allan-Werle deviation analysis has to be carried out to correctly determine the LOD as a function of integration time and correctly evaluate the spectrometer performances, as reported in Appendix A for instance.

In off-axis ICOS, the state of the art in the Near-IR (from 1.5 to 1.65 μm) is a NEA of $3.1{\cdot}10^{-11}$ cm^{-1} Hz$^{-1/2}$ achieved with a degenerate configuration forcing the modes to be degenerate in uniform groups over the cavity FSR [119]. The possibility to employ off-axis ICOS in the Mid-IR at 5.45 μm has been demonstrated in the development of a NO gas sensor. Using a distributed feedback QCL laser, with a wavelength modulation technique and a 50-cm long high finesse cavity with an effective path length of ∼700 m, a minimum concentration of 0.7 ppbv at 1 s (equivalent to $1.4{\cdot}10^{-9}$ cm^{-1} at 1 s) averaging have been achieved [120].

As said previously, the strength of OF-CEAS is the fast acquisition of absorption profiles with relatively simple systems and a high sensitivity. Of particular interest are the results shown by Morville *et al.* in Ref. [114] in 2005. With a DFB laser, in the region close to 1312 nm, and a V-shaped cavity, with base length of 50 cm and finesse ∼20000, 2 cm^{-1} long spectra have been acquired in just 100 ms laser scans with a NEA of $\sim 5{\cdot}10^{-10}$ cm^{-1} Hz$^{-1/2}$. In Ref. [121] a compact system employing an optical cavity with finesse more than 140000 was adopted for water vapor isotope ratio measurements at 1.4 μm reaching a NEA of $5.7{\cdot}10^{-11}$ cm^{-1} Hz$^{-1/2}$ for the acquisition of a spectrum of about 40 cm^{-1}. In the visible, a highly sensitive OF-CEAS spectrometer have been developed in 2008 by Motto-Ros *et al.* for the measurement of very weak oxygen B-band transitions near 688 nm [122]. The authors exploited optical feedback of an ECDL from a Brewster-angle cavity for the acquisition of spectra covering a 1.35 cm^{-1} range in 5 s with a LOD of $3{\cdot}10^{-10}$ cm^{-1} at 1 s averaging. Potentially the NEA of the system was estimated at the level of $6{\cdot}10^{-12}$ cm^{-1} Hz$^{-1/2}$. OF-CEAS has been demonstrated also in the Mid-IR employing QCLs and V-shaped cavities. Of particular interest is the system developed at 5.6 μm showing the lowest detection limit for formaldehyde of $5{\cdot}10^{-10}$ cm^{-1} in 1 s [116]. Another example is the system at 7.84 μm for simultaneous detection of CH_4 and N_2O in air with a LOD of $5.5{\cdot}10^{-8}$ cm^{-1} for 1 s averaging [123].

The most outstanding result, most of all if one considers that it date back to 1998, has been achieved with NICE-OHMS, employing a fixed frequency

Nd:YAG laser locked to a 150 cm long cavity with a finesse of 100000, where a LOD of 10^{-14} cm^{-1} over 1 s has been obtained for sub-Doppler investigations of overtones of C_2HD, C_2H_2 and CO_2 [118]. A huge effort has been spent achieve similar performances for measurement in the Doppler-broadened regime, where NICE-OHMS is more susceptible to etalons and to the difficulty of maintaining the modulation at the FSR-frequency over tuning range of some GHz. Recently Silander *et al.* have demonstrated a NEA of $2.6{\cdot}10^{-13}$ cm^{-1} Hz$^{-1/2}$ and a minimum Allan deviation of $9{\cdot}10^{-14}$ cm^{-1} at 30 s in the Doppler-broadening regime using an Er:doped fiber laser emitting at 1.5 µm (tunable by PZT almost for 3 GHz and for almost 1 nm in temperature) and an optical cavity with finesse 50000 targeting a C_2H_2 transition [124]. NICE-OHMS have been demonstrated also in the Mid-IR employing QCLs achieving performances similar to those of OF-CEAS, for instance in the spectral region starting from 3.5 µm with NEAs of $9.7{\cdot}10^{-11}$ cm^{-1} Hz$^{-1/2}$ [125].

Technique	Spectral Range	Sensitivity	Ref.
Off-Axis ICOS	1.5-1.65 µm	$3.1{\cdot}10^{-11}$ cm^{-1} Hz$^{-1/2}$	[119]
	5.45 µm	$1.4{\cdot}10^{-9}$ cm^{-1} at 1 s	[120]
OF-CEAS	0.688 µm	$3{\cdot}10^{-10}$ cm^{-1} at 1 s	[122]
	1.312 µm	$5.7{\cdot}10^{-11}$ cm^{-1} Hz$^{-1/2}$	[121]
	5.6 µm	$5{\cdot}10^{-10}$ cm^{-1} at 1 s	[116]
	7.84 µm	$5.5{\cdot}10^{-8}$ cm^{-1} at 1 s	[123]
NICE-OHMS	1.064 µm	10^{-14} cm^{-1} at 1 s	[118]
	1.55012 µm	$9{\cdot}10^{-14}$ cm^{-1} at 30 s	[124]

Table 3.1: Performances of CEAS spectrometers in terms of sensitivity.

A number of CEAS systems were developed in conjunction with optical frequency combs for absolute frequency determinations. In this thesis the focus is on Comb-Assisted CEAS Doppler-free systems achieving kHz-level accuracies in centre frequency determinations, because of their relevance with the system developed in this thesis. Direct Frequency Combs or Dual Frequency Combs CEAS systems are beyond the scope of this thesis and the reader is referred to Refs. [126, 127] for instance. It is remarkable that among Comb-Assisted CEAS techniques only few demonstrations have been provided where the absorption is measured directly at the cavity output under a stationary coupling in a DC configuration, because of the cavity frequency-to-amplitude noise conversion. In most of them the laser is locked to the cavity and the cavity is dither-locked to a sub-Doppler feature.

A very interesting molecular target is C_2H_2 because of the presence of very intense lines in the Telecom range to be exploited as references. In 2005 Edwards *et al.* performed a broad survey over 41 lines of the $\nu_1 + \nu_3$

combination band of $^{12}C_2H_2$ in the 1.5 μm region employing the top-of-dip locking [4]. The authors developed two laser frequency standards starting from two semiconductor lasers stabilized to transitions of C_2H_2 using Sub-Doppler CEAS. The 41 C_2H_2 line centre frequencies have been measured by means of an optical frequency comb and the mean retrieved experimental uncertainty (Type A) was 3 kHz with a systematic contribution (Type B) of 10 kHz. Compared to the absolute centre frequency values of almost two hundred THz the overall uncertainty was at the few parts over 10^{11}. Benefiting from the frequency axis calibration of the comb, also spectroscopic values for the band parameters have been improved with respect to the one reported previously in literature. Later, Madej *et al.* performed measurements on the same C_2H_2 band with a similar system [4] but taking care of the influence of systematic effects [5]. Over a broader spectral region the uncertainties shown were as low as 2 kHz leading to improved determinations of the molecular parameters of the band. Recently other investigations were performed over the ν_4 and ν_5 excited hot bands in the $\nu_1 + \nu_3$ band of acetylene by Twagirayezu *et al.* achieving uncertainties ranging from 3 to 22 kHz [6]. Particularly significant is the fitting analysis which shows that the Lorentzian profile of the dip is clearly distorted and made asymmetric because of effects due to power broadening.

Several lines of ammonia have been investigated, by the system described in Ref. [5], in the spectral region from 1510 to 1560 nm of the $\nu_1 + 2\nu_4$ absorption band [89]. Four ammonia line centre frequencies were measured showing high reproducibility and overall uncertainties ranging from 3 to 5 kHz. The relevance of this paper is that for the first time were reported saturated absorption lines in a spectral region lacking strong absorbers.

Another extensive Sub-Doppler investigation was done on the $H_2^{18}O$ and $H_2^{17}O$ molecules in 2010 by Gambetta *et al.* [90]. The authors used an ECDL in the region from 1.38 to 1.41 µm referred to a frequency comb to determine line centre frequencies with a total uncertainty of $\sim$ 30 kHz, allowing an accurate determination of the rotational energy levels.

3.3 Cavity Ring Down Spectroscopy

This section regards the Cavity Ring Down Spectroscopy technique, whose principle relies on the measurement of the photon decay time inside an optical cavity when the injected input beam is abruptly interrupted.

A CRDS approach has been employed in this thesis with a CW laser to probe single absorption lines of CO_2 in the Doppler broadening regime with the adoption of a frequency comb, as it is going to be discussed in 5.

In the following subsections we begin with a description of the basic principles of the technique, then we show the most relevant implementations and state of the art.

3.3.1 The Principles of CRDS

The first photon decay time measurement in an optical cavity was performed by Anderson, Frisch and Masser in 1984 [110]. The authors demonstrated that the decay time of the transmitted intensity provided a precise measurement of the reflectivity of low-losses highly-reflective cavity mirrors. In particular they noticed that the higher was the mirrors reflectivity, the better was the precision in the reflectivity measurement. After few years, the concept was employed in spectroscopic applications for monitoring the frequency dependent losses of an optical resonator due to an enclosed absorbing medium. The first CRDS measurement was performed in 1988 by O'Keefe and Deacon [128] using a pulsed laser injected into an optical cavity filled with the absorbing sample. The authors showed how to determine the absorption spectrum of a weak electronic O_2 band near 690 nm by measuring the photon cavity decay rate at different frequencies.

When the input beam is coupled with the cavity resonance there is a build-up of photons and a part of the intra-cavity intensity is transmitted, then after an intensity threshold is reached at the output photodetector, the input laser is shut off. If the switching off of the input happens within a time shorter then the cavity response time, the transmitted intensity experiences an exponential decay behaviour imposed by the photon lifetime called Ring Down (RD) time.

The light decay can be described by a simple 1-dimensional model for an optical cavity made of two identical mirrors, at a distance L_C, with an intensity reflection coefficient R. When an intensity threshold $I(0)$ is reached, the laser injection is stopped and the intra-cavity intensity performs round-trips gradually leaking out through the mirrors. The transmitted intensity after k round-trip is given by:

$$I_{out}(k) = I(0)R^{2k}e^{-\alpha(\omega)2kL_C} = I(0)e^{-2k(-lnR+\alpha L_C)} \tag{3.33}$$

The discrete variable k can be substituted by a continuous time variable $t = 2kL_C/c$ corresponding to the time to perform k round-trips, so that the intensity at the cavity output is written as:

$$I_{out}(t) = I(0)e^{-\frac{ct}{L_C}(-lnR+\alpha(\omega)L_C)} \tag{3.34}$$

Since the reflectivity R is typically close to 1, it is possible to approximate $lnR \approx (R-1)$ obtaining:

$$I_{out}(t) = I(0)\exp\left[-\left(\frac{(1-R)c}{L_C} + \alpha(\omega)c\right)t\right] \tag{3.35}$$

that is usually rewritten as:

$$I_{out}(t,\omega) = I(0)e^{-\frac{t}{\tau(\omega)}} \tag{3.36}$$

where $\tau(\omega)$ is the Ring Down time. Comparing Eq.(3.36) with Eq.(3.35), the RD time in presence of an absorbing medium is:

$$\tau(\omega) = \frac{L_C}{c} \frac{1}{1 - R + \alpha(\omega) L_C} \tag{3.37}$$

whereas for an empty cavity:

$$\tau_0 = \frac{L_C}{c} \frac{1}{(1 - R)} \tag{3.38}$$

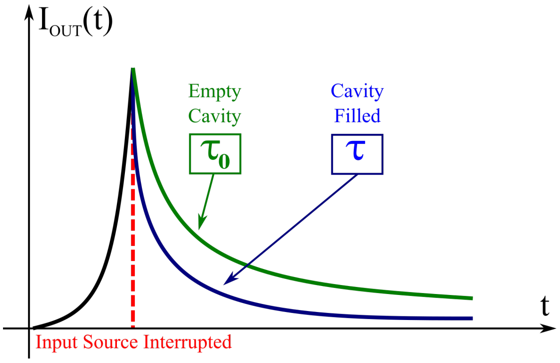

Figure 3.4: Ring down decay behaviours in the case of empty cavity (green curve) and of cavity filled with an absorbing medium (blue curve). The red-dashed line corresponds to the instant when the input source is abruptly switched off.

Figure 3.4 shows the different exponential decay behaviours of the transmitted intensity in the presence or not of an absorbing medium inside the cavity. The absorption coefficient of the sample can be deduced by the following expression:

$$\alpha(\omega) = \frac{1}{c} \left(\frac{1}{\tau(\omega)} - \frac{1}{\tau_0} \right) \tag{3.39}$$

Eq.(3.39) is not dependent either on the intensity of the input source or on the cavity length, so the measurement of the absorption coefficient is intrinsically immune to intensity noise of the laser source and does not require calibration of the cavity length.

In CRDS, the natural consequence of an exponentially decaying field whose spectrum, because of Fourier transform, retraces the Lorentzian cavity mode resonance and can thus be regarded as a broadband field. So CRDS may take advantage of a cavity enhancement factor of the interaction length $\beta = 1$ with an expression that is the same of Eq.(3.24):

$$L_{eff,RD} = \frac{F}{\pi} L_C \approx c\tau \tag{3.40}$$

The lowest absorption detectable by a cavity ring down absorption spectrometer α_{min} can be evaluated differentiating Eq.(3.39) in the limit when

$\tau \to \tau_0$. In the case of a spectrometer measuring the decay time τ with a standard deviation $\delta\tau$, α_{min} is obtained from the shot-to-shot fluctuations $\delta\tau/\tau_0$ and $L_{eff,RD}$:

$$\alpha_{min} = \left[\frac{1}{L_{eff,RD}}\frac{\delta\tau}{\tau}\right]_{\tau\to\tau_0} = \frac{\delta\tau}{c\tau_0^2} \tag{3.41}$$

where we highlight the inverse correlation between α_{min} and the square value of τ_0, meaning that system with higher values of τ_0 can achieve, in principle, better sensitivity levels. The value $\frac{\delta\tau}{\tau_0}$ is a function of several parameters, such as the laser linewidth, mechanical and thermal stability of the cavity mirrors, noise of the detectors and circuitry, number of bits in the digitalization and so on. While parameters such as the laser linewidth and detection noise are responsible for a low Signal-to-Noise Ratio (SNR) of the measured exponential decay, α_{min} deviates from the white-noise behaviour over integration time $1/\sqrt{T}$ mainly because of long term drifts of the baseline noise due to mechanical and thermal fluctuations of the cavity. The presence of drifts, due to flicker or random walk noise causing the deviation from the $1/\sqrt{T}$ law, can be evidenced by an Allan-Werle analysis performed on the ring down decay constants, as already pointed out in the previous section. $\frac{\delta\tau}{\tau_0}$ depends also on the type of sources employed, being it pulsed or continuous-wave (CW). Indeed typical values when using pulsed sources are at the level of 1%, whereas with CW sources the value achieved are as low as 0.03 %. Differences between pulsed-CRDS and CW-CRDS are going to be described in details in the following subsection, together with state of the art performances achieved in CRDS measurements.

3.3.2 CRDS: Overview and State of the Art

This subsection is an overview of the history of cavity ring down spectroscopy, from the first CRD experiments to the state of the art both in terms of sensitivity and of accuracy.

As stated before, the first cavity ring down absorption experiment was performed in 1988 by by O'Keefe and Deacon with a pulsed laser source [128]. Pulsed laser sources were chosen because of their spectral bandwidth, wider than the cavity mode spacing, basing on the idea of obtaining an easy coupling between the source and the cavity modes. The idea was that pulses shorter than the cavity response time would have been transmitted through the cavity unperturbed, without undergoing interference inside the resonator. Actually, Lehmann and Romanini deomnstrated that the previous idea was not correct [129]. With a rigorous theoretical analysis the authors showed that efficient photon build up inside the cavity occurs only at the resonance frequencies, where interference takes place. Because of it, a pulsed CRDS scheme is able to adequately probe an absorption line overlapped with the cavity modes only at resonance frequencies, increasing the separation of the acquired spectral points. Another experimental hurdle is due to high order transverse modes excitation, leading to multi-exponential decays because the losses for TEM_{mn} modes are different from those of the fundamental TEM_{00}.

To overcome the previous limitations, Romanini and co-workers developed the first CW-CRDS system in 1997 [2], which is still at the basis of state of the art spectrometers developed today. The adoption of CW laser sources was motivated by their characteristic narrow linewidth (less than tens of MHz) to excite single cavity modes, when spatially mode-matched to the fundamental TEM_{00}. Also a high coupling efficiency was possible, which was beneficial to improve the SNR of the exponential decays and the statistics of the ring down times. The first CW-CRDS measurement was performed with a tunable ring dye laser to probe the absorption of C_2H_2 overtones, other molecular samples using commercial dye lasers and diode lasers were investigated later [2, 130]. The matching between the laser frequency and the cavity resonance can be achieved following two ways: the first is to tune the cavity length by means of a piezoelectric transducer mounted on one cavity mirror, the second is to tune the laser by means of current or temperature sweeps. In both ways, a dither lock may be established to have a synchronous match between the laser frequency and the cavity resonance. Experimentally, to induce clear exponential decays, it is essential to have a fast optical switch, such as an Acousto-Optic Modulator (AOM), to turn off the laser faster than the cavity response time. The sensitivity achieved in the first CW-CRDS experiment was already at the 10^{-9} cm^{-1} level [2, 130].

Over the past decades, efforts have been spent towards the improvement of the sensitivity, with advancements facilitated by narrower lasers and by higher and higher reflectivity coatings. One of the lowest limit of detection reported so far in a CRDS measurements is $5{\cdot}10^{-13}$ cm^{-1} achieved in Ref. [131] using a free-running Distributed FeedBack (DFB) laser, in the spectral region across 1450 nm, together with a 140 cm long cavity with a finesse exceeding 500000 giving ring down times of more than 700 µs. The performances of the spectrometer were found limited by the photodetector noise at a NEA of $1.3{\cdot}10^{-11}$ cm^{-1} $\text{Hz}^{-1/2}$. To avoid thermomechanical drifts of the cavity, that emerged in an Allan-Werle deviation analysis, the acquisition time for a single spectrum was kept below 10 s. To reach the sensitivity of $5{\cdot}\ 10^{-13}$ cm^{-1}, the authors exploited the fact that by averaging subsequent spectra acquired in a time shorter than 10 s, the limitations retrieved by the Allan-Werle analysis no longer apply [132]. Importantly, averaging spectra over a period of five days, no limitations imposed by etalons have been evidenced, leading to the state of the art LOD. With that spectrometer, several first overtone electric quadrupole transitions of H_2 and D_2 have been investigated showing a good agreement with the values predicted by *ab initio* quantum electro-dynamic models developed for simple light diatomic molecules. The other impressive result was achieved in the detection of an electric quadrupole transition of N_2, the 3-0 S4 with a line strength of about $1.5{\cdot}10^{-31}$ cm/molecules which is one of the weakest ever measured.

As we said in Section 3.1, one of the main disadvantages of the employment of high finesse cavities is due to the difficulty in achieving a good light coupling, because the probe laser usually has a broader linewidth compared to the cavity resonance and this impairs the coupling efficiency. To improve the coupling efficiency and repeatability of the ring down events, laser linewidth narrowing techniques have been adopted also in CRDS systems, in particular Pound-Drever-Hall locking, as shown in Appendix B. A tight locking of the probe laser to the cavity is beneficial in CRDS because of two factors: i) the coupling into the cavity is very efficient and the exponential decays have a better SNR, ii) the RD-rates per single spectral point are fast, thus it is possible to average several RD constants increasing the sensitivity per spectral point. A disadvantage is in the system complexity due to the fact that to start the exponential decays the PDH-lock is interrupted, so a careful relocking procedure is necessary to achieve high repetition rates. Also when performing acquisitions of absorption spectra the PDH-lock has to be interrupted before moving to the next spectral point, thus the acquisition time for a single spectrum may require longer times than in simpler CRDS schemes. The first implementation of PDH-locking in a CW-CRDS system was demonstrated in Ref. [133], where two orthogonal linearly polarized beams of a single diode laser where employed, one to achieve the tight locking and the other to acquire ring down events and probe absorption profiles. The LOD obtained in that first experiment was $5{\cdot}\,10^{-9}$ cm^{-1} using a single ECDL laser, then other groups adopted the same operation principle improving the sensitivity down to 10^{-12} cm^{-1} Hz$^{-1/2}$ and a ring down repetition rate of 80 kHz obtained in Ref. [134] with a Nd:YAG laser.

An implementation to acquire ring down events with a high repetition rate and broad tunability was demonstrated in the Frequency-Agile Rapid-Scanning spectroscopy (FARS) scheme [135], in this thesis a CRDS acquisition scheme based on the FARS approach combined with an interleaving of spectral point has been adopted and is going to be discussed in Chapter 5. The principle of the technique is to employ a high-bandwidth electro-optic phase modulator (EOM) providing two sidebands, spaced in frequency from the carrier by a RF oscillator, to quickly shift one sideband from a cavity resonance to the adjacent one and acquire other spectral points obtaining a complete spectrum with a fast acquisition. Ring down events are triggered by switching off the RF signal to the EOM, thus without the need of an external AOM. Using an ECDL laser PDH-locked to a high finesse cavity whose length was stabilized against a co-resonant I_2-stabilized HeNe laser, the authors achieved a NEA of $2{\cdot}10^{-12}$ cm^{-1} Hz$^{-1/2}$ with a repetition rate of $\sim$ 8 kHz and a tunability of almost 70 GHz. Long *et al.* used the FARS CRDS adopting an heterodyne detection scheme in the so called Heterodyne-Detection CRDS (HD-CRDS) reaching a NEA of $6{\cdot}10^{-14}$ $\mathrm{cm}^{-1}/\mathrm{Hz}^{-1/2}$ [136]. HD-CRDS is performed by exciting two modes of an optical cavity, spaced by a selected integer number of the cavity FSR, and measuring the time-varying transmitted intensity at the frequency corresponding to the difference between the two modes. The advantage of the approach is the shift of the measurement at frequencies above the limiting Flicker noise of traditional CRDS systems and the monitoring of differential losses between the two cavity modes. The strength of the system was the capability of reaching the quantum noise limit, at reasonable optical powers, and with the use of a broadly tunable ECDL. In Reference [136] with the employment of high bandwidth EOMs and an arbitrary waveform generator a 2-THz-wide spectrum was acquired in 20 minutes. Apart from the previous investigation, the HD-CRDS technique has not been largely employed for broad spectroscopic surveys, as compared to the basic CRDS scheme, because of the systems requirements and complexity.

A very interesting alternative to FARS-CRDS is the PDH locking of the cavity to a highly-stable Hz-linewidth master laser, obtained by a V-shaped-Cavity Optical Feedback (VCOF) locking [137], together with a Single Side-band Modulator (SSM) to tune the master laser frequency over an absorption profile in a FARS-like approach. A sensitivity of $5{\cdot}10^{-13}$ cm^{-1} $\mathrm{Hz}^{-1/2}$ close to the shot-noise limit has been demonstrated by such technique. One of the weak points of all FARS approaches is the poor spectral separation of the acquired points, mainly determined by the cavity FSR. To increase the number of points per spectrum, the FARS approach together with the use of a SSM for fast frequency tuning were employed for an interleaved-FARS (IFARS) CRDS system developed in this thesis, presented in Chapter 5.

Another method to account for long term drifts of the experimental conditions is to monitor in real time the empty-cavity RDs and the medium absorption in a strong saturation regime, approach proposed by the Saturated Absorption Cavity Ring-down (SCAR) [138]. As a difference between the linear absorption regime where the exponential decays are characterised by a single decay value τ, in the saturated regime the evolution of the intra-cavity intensity is no more a single exponential decay. The SCAR approach exploits the fact that in the strong saturation regime the multi-exponential decays are substantially characterised by two decay constants: the initial decay signal depends only on the empty-cavity ring down constant τ_0, since the medium cannot absorb any more photons, whereas the lower part of the signal, characterised by a decaying intensity, depends on the ring down $\tau(\omega)$ due to the sample absorption. With this technique, measurements have been performed on CO_2 at 4.2 µm achieving a LOD of over about 160 s $1.1{\cdot}10^{-9}$ cm^{-1} which has enabled for the first time the measurement of the hyperfine structure of an excited vibrational state with a relative accuracy of 10^{-11} [138]. Recently radiocarbon dioxide detection at few parts per quadrillion sensitivity have been demonstrated employing SCAR using a

Quantum Cascade Laser (QCL) in the 4.5 µm region and a cavity with more than 10^4 finesse cooled down to 170 K [139]. Such detection levels were close to that offered by mass spectrometry, opening the way to sensitive optical radiocarbon measurements for dating applications.

Technique	Spectral Range	Sensitivity	Ref.
Dither-locked CRDS	1.45 µm	$5{\cdot}10^{-13}$ cm^{-1}	[131]
PDH-locked CRDS	1.064 µm	10^{-12} cm^{-1} Hz$^{-1/2}$	[134]
FARS-CRDS	1.599 µm	$2{\cdot}10^{-12}$ cm^{-1} Hz$^{-1/2}$	[135]
HD-CRDS	1.599 µm	$6{\cdot}10^{-14}$ cm^{-1}/Hz$^{-1/2}$	[136]
SCAR	4.2µm	$1.1{\cdot}10^{-9}$ cm^{-1} at 160 s	[138]

Table 3.2: Performances of CRDS spectrometers in terms of sensitivity.

One of the main focus of the aforementioned systems was the search of high sensitivities, where achievements have been reached in the minimization of drifts of the vertical axis. High sensitivities lead to high SNR and thus to high levels of precision in the horizontal axis. Interestingly, less attention was paid on the accuracy of the frequency axis. Indeed it started mainly during the last decade, when the levels offered by commercial wavemeters with typical resolution of more than 30 MHz were the main limit to the frequency uncertainty. One of the first implementation of a system focusing on the accuracy of the frequency axis was the Frequency Stabilized CRDS (FS-CRDS) scheme proposed in 2004 in Ref. [140] by the group of J.T.Hodges. The principle of the technique consists in an active stabilization of the length of a high finesse cavity with respect to an He-Ne reference laser, so that periodic mode structure of the cavity becomes fixed and can be used as a stable frequency axis for the spectroscopic measurements. Thanks to dichroic mirrors, the cavity exhibits a low finesse in the visible range for the locking reference laser and a high finesse in the Near-IR for the probe laser. After a first implementation where the probe laser was dither-locked to the cavity [140], the probe laser was PDH-locked to it [141]. Later in 2012 using an FS-CRDS system in which the He-Ne reference was tuned by an AOM, Long *et al.* achieved a total frequency uncertainty of $\sim$ 10 kHz combined with a sensitivity of $1.8{\cdot}10^{-11}$ cm^{-1} in less than 10 hours averaging [142]. With that system spectroscopic investigations in the Near-IR of O_2, CO_2 and H_2O have been performed, where the retrieved frequency values showed discrepancies up to 30 MHz with those reported in the HITRAN. The drawback of FS-CRDS is the system complexity because of the multiple locking schemes and of the need of custom defined dichroic mirrors.

The most relevant advancements in terms of accuracy have been achieved with the addition of Optical Frequency Combs (OFC) to CRDS. The periodic structure of the OFC is used to calibrate the frequency axis increasing both the accuracy of the spectrometer and the detection limit by massively averaging of spectra sharing the same horizontal axis. In 2013, Truong *et al.* successfully added an OFC to a FS-CRDS system [143] developing the Comb-Linked FS-CRDS (CL-FS-CRDS). The experimental system consisted in an ECDL (at 1.57 μm) PDH-locked to a cavity, with a finesse of $2{\cdot}10^4$, which was scanned over some cavity FSR to acquire spectral points. To tune the laser over different cavity modes the PDH-locking is interrupted and to relock the laser to the cavity automatically the authors used the procedure developed by Cygan *et al.* [141]. Absolute frequency calibration was provided acquiring the beat-note between the probe laser and the nearest comb tooth. The molecular target was an isolated CO_2 absorption line with a line strength suitable to reach SNR of 10^4 in the few Pascal pressure range. Centre frequency determinations at different pressures lead to the retrieval of the zero-pressure centre frequency with an overall uncertainty of ~ 9 kHz after acquisition of a huge number of spectra over several days.

A distinctly different approach was proposed by Gatti *et al.* in the Comb-Locked CRDS (CL-CRDS) scheme [144]. The core feature of the system was a frequency locking of an ECDL (at 1.57 μm) probe laser with the nearest comb mode using a feed-forward approach, narrowing the probe laser FWHM from 110 kHz at 10 ms to 68 kHz. A high finesse cavity ($\sim$125000) was slaved to the laser using a dither-locking at 500 Hz and frequency tuning was achieved slightly changing the comb repetition rate. The system NEA was limited by long term drifts of the system, which attested a LOD of $5.7{\cdot}10^{-11}$ cm^{-1} after a single scan acquisition over 2.5 GHz. Acquisition of a huge number of spectral points was possible thanks to the tuning procedure and to the cavity slaved to the laser. Spectroscopic tests were performed on the same CO_2 line investigated by Truong *et al.*. The retrieved centre frequency uncertainty over several measurements was at the 3 kHz level and, impressively, the zero pressure centre frequency value of the P14e line of the 30012-00001 band of CO_2 was find in agreement with that from Truong *et al.* [143] within 1 kHz, confirming the importance of OFCs for the traceability of the spectroscopic determinations.

In 2015 a Comb-Assisted CRDS system was developed by Mondelain *et al.* employing a widely tunable DFB laser source in the Near-IR to probe CO absorption lines with a NEA down to 10^{-11} cm^{-1} Hz$^{-1/2}$ and accuracies in the retrieved line positions better than 500 kHz. The frequency axis calibration was performed before every ring down events acquiring the beat-note of the probe laser with the frequency comb by a fast digitalization board and extracting its frequency value with a Fast-Fourier-Transform (FFT) algorithm.

Worth of notice are also the results reported in Ref. [145]. Using a VCOF-laser and the PDH-locking of the high-finesse cavity to it, with a FARS like approach 12 CO_2 Lamb-dips in the spectral region near 1.6 μm were probed, achieving uncertainties in the retrieved centre frequencies of few parts 10^{11} providing an accurate frequency grid in the spectral region from 1599 to 1616 nm.

Chapter 4

Comb-Assisted Cavity-Enhanced Spectrometer: Application to Saturated Spectroscopy of C_2H_2

This chapter describes the Comb-Assisted Cavity Enhanced Spectrometer for Sub-Doppler investigations developed in this thesis. The guideline of the experimental activity was the realization of a system for Doppler-free spectroscopy to probe single overtone lines, especially the ones difficult to saturate, and to explore ultimate accuracy levels. This has driven us to the development of a spectrometer with an innovative Pound-Drever-Hall (PDH) locking scheme employing just a single feedback loop, whose frequency actuator is an ultra-fast and wide-bandwidth Single Sideband Modulator (SSM). The locking was tight enough to ensure an efficient coupling of the probe laser to the cavity and to achieve a high intra-cavity power. A simple DC read-out of the signal transmitted from the cavity has been adopted to directly probe Lamb-dips, which is of particular interest to study line-shape effects in the sub-Doppler regime. The final aim was to check the accuracy of the spectrometer at the kHz level, which has been performed on three well known acetylene lines studied by metrological institutes, namely the P30e, P28e and P26e of the 10100-00000 band, and to investigate the saturation of an absorption line featuring one of the lowest Einstein coefficient, the P15e of the 01120-00000 band, with a good Signal to Noise Ratio (SNR). The results achieved have lead to the publication of two papers: Ref. [146] and [144].

The chapter is divided into four sections: the first describes the optical layout of the spectrometer focusing on the basic components. The second section regards the experimental characterisation of the Pound-Drever-Hall locking scheme, giving details on its performances. In the third section we report an analysis of the spectrometer sensitivity in the time domain, by an Allan-Werle analysis, and in the frequency domain, evaluating the baseline noise reduction after subsequent spectra averaging. The last section shows the Lamb-dip acquisitions with an analysis of the precision and accuracy of the system.

4.1 Optical layout of the Spectrometer

The complete architecture of the spectrometer is sketched in Figure 4.1.

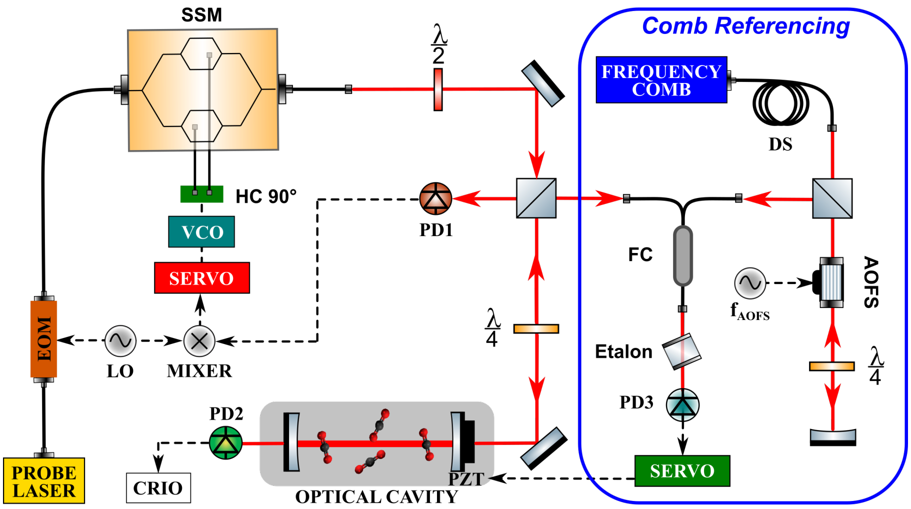

Figure 4.1: Representation of the Comb-Assisted Cavity Enhanced Spectrometer. The left side of the picture regards the tight locking of the probe laser to the cavity, whereas the right side to the comb referencing for absolute frequency calibration. EOM: electro-optical modulator; AOFS: acousto-optic frequency shifter; f_{AOFS}: AOFS driving frequency; VCO: voltage controlled oscillator; MIXER: electrical signal mixer; PZT: piezoelectric transducer; FC: fibre coupler; LO: local oscillator; DS: dispersion shifted fibre; HVA: high-voltage amplifier; RFA: radio-frequency amplifier; HC 90°: 90° hybrid coupler; RF Generator: radio frequency generator; RF Switch: radio-frequency switch; SSM: single sideband modulator; L1,2: lenses; DS: dispersion shifted fibre; PD1,2,3: photodetectors; CRIO: compact reconfigurable input/output board.

The probe laser is a Continuous Wave Extend Cavity Diode Laser (CW-ECDL) (Toptica model DL pro) with a broad tunability in the 1.5-1.63 µm range and an output power of ∼30 mW. The free-running linewidth of the ECDL was characterised against the emission of a sub-kHz master fibre laser (NKT Koheras AdjustiK E15) and results in 110 kHz at 10 ms, thus much narrower than the typical few-MHz linewidth of DFB lasers.

The ECDL injects a series of two electro-optic modulators: the first is an Electro-Optic phase Modulator (EOM) (Thorlabs LN63S-FC), driven by a modulation frequency f_{LO} of about 16 MHz, generating the triplet signal used for the Pound-Drever-Hall (PDH) locking. The second modulator is a Single Sideband Modulator (Oclaro custom model), whose working principle is described in Appendix C, which acts as an ultra-fast frequency actuator with a working bandwidth from DC to 20 GHz and a sub-ns response time. With the proper setting of the bias voltages and the application of the quadrature-phase-shift Radio-Frequency (RF) signal, by means of a 90° hybrid coupler (Krytar 3005070), the generated single sideband has a relative contrast of more than 35 dB from the optical carrier and the other suppressed sideband.

The output of the SSM is collimated by a variable focal length collimator to a beam waist of 470 µm to mode match the TEM_{00} mode of a high finesse optical cavity, which is a commercial stainless steel cylinder (CRD-optics model 901-0010-1530) composed by two high reflectivity mirrors (CRD-optics $R \simeq 0.999975$) with a radius of curvature of 1 m, implying a cavity finesse of about 125000. The cavity has a geometrical length of 50 cm with a Free Spectral Range of ∼295.7 MHz. The estimated cavity resonance linewidth is ∼3 kHz, retrieved from a ring down time of approximately 63 µs, which requires a wide bandwidth locking to obtain an efficient coupling when employing a laser a factor more than 30 larger. One mirror is mounted on a cylindrical PZT (PiezosystemJena series R) to tune the cavity length. To improve the short term mechanical stability and increase the thermal mass of the cavity, it is loaded with an aluminium shell, properly designed to maintain a cylindrical shape, hold by two Teflon supports, as sketched in Figure 4.2, and is housed inside a wooden box to reduce acoustical and thermal induced drifts.

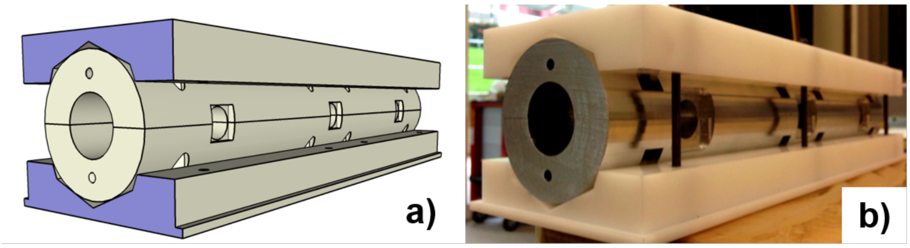

Figure 4.2: a) Design of the cylindrical shape aluminium shell and b) its final fabrication. The shell helps in improving the short term mechanical stability of the cavity and also increases its thermal mass.

The power transmitted from the cavity is acquired in a DC detection scheme using a variable gain detector from 10^3 to 10^7 V/W ensuring signals of few Volts even in the case of optical powers below 1 µW (Thorlabs PDB150C). The reflected signal from the cavity is extracted using a combination of a polarization beam splitter and a quarter-wave plate instead of an optical circulator, which has the advantage of minimizing any optical delay, and acquired by an avalanche photodetector with 50 MHz bandwidth and $0.9{\cdot}10^6$ V/W (Thorlabs APD110C), then it is demodulated to obtain the PDH error signal sent to a servo PID (Imra custom model), whose parameters have been set experimentally by a characterisation of the frequency spectrum of the error signal, as treated in the following section.

The SSM driving RF signal is provided by a commercial VCO centred at 800 MHz (Mini-Circuits ZX95-850-S+) controlled by the servo PID. Since the servo has an output range of ±3.5 V and the VCO has a 22 MHz/V frequency to voltage conversion, the overall tuning range is ±75 MHz, which we found suitable to compensate cavity drifts and maintain the locking for several hours. The frequency of the single sideband is equal to the frequency of the optical carrier ν_C plus the shift provided by the VCO: $\nu_{SSB} = \nu_C + f_{VCO}$. The output optical power of the SSM depends on the applied RF signal power, typically with a RF power of 6 dBm and on optical input of 20 mW the output is almost ∼100 µW. Amplifying the RF signal up to 27 dBm at the input port of the SSM, the output power can reach almost 10% of the input optical power corresponding to 2 mW.

The absolute frequency calibration is given by an Er:fibre frequency comb centred at 1550 nm (Toptica FFS1550). The oscillator output is split in two branches for further amplification till a level of 250 mW. One branch seeds a Highly Non-Linear Fibre (HNLF) generating the SuperContinuum (SC) spanning from 1 to 2.2 µm, enabling f_{ceo} detection by a home-made f-2f interferometer [45] employing a Periodically Poled Lithium Niobate (PPLN) crystal for frequency doubling. The second branch is sent to a Dispersion-Shifted (DS) fibre broadening the spectral output from 1.4 to 1.7 µm to match the tuning range of the ECDL. f_{rep} is phase locked against a GPS-disciplined Rb clock oscillating at 10 MHz with a frequency instability of $6{\cdot}10^{-12}$ over 1 s, while f_{ceo} is frequency-locked to the same primary reference acting on the pump current by means of a feedback loop and a servo PID (Toptica Digilock 110). Under locking conditions, the f_{ceo} stability was found to be within 2 kHz rms over 10 ms, thus negligibly affecting the error budget of absolute frequency determinations.

The beat-note between the comb and a fraction of the PDH-locked laser is acquired by an InGaAs photodetector (custom model), after optical filtering of the comb by means of an etalon (FWHM 1 nm FSR 44 nm from SLS Optics, custom model), and frequency locked to the GPS-disciplined reference by a low bandwidth feedback loop (700 Hz bandwidth) acting on the cavity PZT. In this way the cavity length is stabilized and the cavity resonance, to which the probe laser is locked to, is forced to remain at a fixed distance from the nearest comb mode. The frequency axis calibration is obtained from Eq.(2.10) with the addition of the VCO contribution and of the shift provided by an Acousto-Optic Frequency Shifter (AOFS), employed for frequency tuning as described below, resulting in:

$$\nu_{ABS} = nf_{rep} \pm f_{ceo} \pm f_{beat} + f_{VCO} - f_{AOFS} \tag{4.1}$$

where the order n can be approximatively determined firstly using a commercial wavemeter, and the signs of the f_{ceo} and f_{beat} can be deduced by slowing changing f_{rep} and monitoring the variations in both f_{ceo} and f_{beat}. We found experimentally that the beat-note between the PDH-locked laser and the comb must have a contrast from the noise floor of more than 25 dB at a resolution bandwidth of 10 kHz to reduce the averaged rms deviations of f_{beat} below 0.2 kHz. This requires matching of the linear polarizations of the comb and of the probe laser.

Since the laser frequency is fixed to the cavity resonance by the PDH-locking, frequency scans are obtained by tuning the whole comb pattern, keeping f_{beat} fixed, by means of an AOFS in a double pass pass configuration. As the AOFS provides a single pass diffraction efficiency higher than 75% in a 20 MHz range centred at 80 MHz, exploiting a double passage leads to a diffraction efficiency of $(75\%)^2$ over a tuning range of 40 MHz which is more than enough for sub-Doppler investigations. The scan is performed in steps of 1 MHz, corresponding to the spectral point separation, changing the RF driving frequency f_{AOFS}.

The remote control acquisition board is a Compact Reconfigurable Input-Output (CRIO) equipped with a Field-Programmable Gate Array (FPGA) (National Instruments Virtex-5 LX50). The board serves different purposes: i) acquisition of the voltage from the photodetector at the cavity output, after a selected integration interval, associating to every point a relative frequency value, ii) control of the RF oscillator driving the AOFS to tune the frequency comb and perform frequency scans, iii) absolute frequency calibration of the acquired data, spectra averaging, fitting and saving of the retrieved spectroscopic parameters.

4.2 Wide-bandwidth Pound-Drever-Hall Locking

This section describes the PDH-locking of the probe laser to the cavity and its performances.

The PDH locking procedure starts with a scan of the cavity length at a rate of about 800 MHz/s in an open loop condition, as shown in Figure 4.3. It reports the transmitted signal from the cavity, characterised by the typical triplet given by the carrier and phase-modulation sidebands (blue trace), and the corresponding error signal (red trace), obtained demodulating the reflected signal at the f_{LO} frequency. Figure 4.3 A zoomed-in window of the transmitted signal of the carrier and of the corresponding part of the error signal at half the scan speed is represented in Figure 4.4a). The transmitted and the error signal quickly increase when the superposition between the

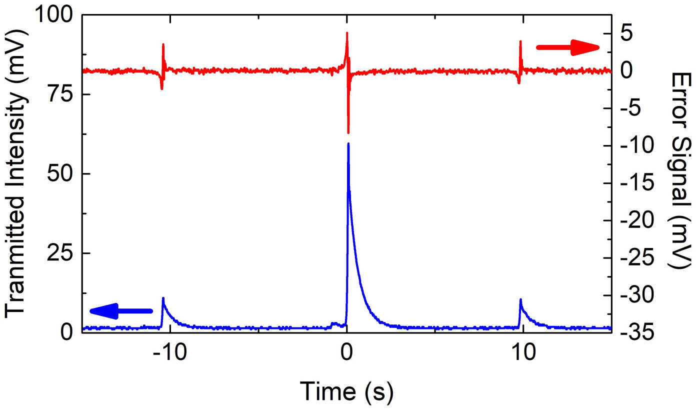

Figure 4.3: Transmitted signal from the cavity (blue trace) and PDH error signal (red trace) when the cavity length is modulated by means of the cavity PZT at a rate of about 800 MHz/s [146].

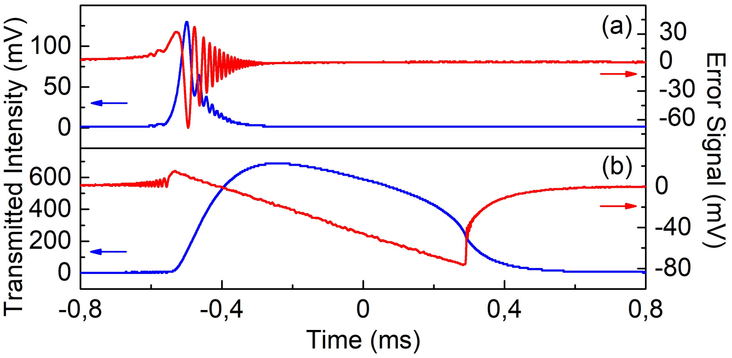

Figure 4.4: Comparison between the transmitted (blue trace) and error signal (red trace) when the proportional servo is set to OFF (panel a) or ON (panel b) [146].

cavity and the laser mode happens, whereas when departing from it there is a non-adiabatic exponential decay showing a ringing behaviour due to the Doppler-shift at every mirror bounce, as discussed in 3.1.3. To start the locking condition the proportional servo is turned on while the cavity length is still modulated acting on the cavity PZT. The influence of the servo is shown in Figure 4.4b), where it forces the laser to remain on resonance, increasing the output transmission by a factor ~7 and the time interval over which the laser may follow the scanning cavity mode, corresponding to a range of about 600 kHz, until the error signal reaches the minimum of its dynamic and the superposition is lost. The locking condition is achieved by reducing the scan rate of the signal sent to the cavity PZT until its complete removal and simultaneously turning on the integrative and the derivative servo.

We have optimized the servo PID parameters experimentally by looking at the frequency spectrum of the PDH error signal, identifying the conditions of maximum bandwidth and at the same time of the maximum suppression of the relative low frequency noise of the laser with respect to the cavity. For the latter we found particularly useful the employment of a double-integrative stage to further reduce the main noise contribution coming from frequencies lower than 1 kHz. Figure 4.5 is already expressed in terms of Hz/Hz$^{1/2}$ and represents the relative frequency noise PSD between the PDH-locked laser and the cavity. It has been retrieved from the frequency spectrum of the error signal in V^2/Hz, rescaled by the low-pass filtering action of the cavity at the frequency f_C of about 1.5 kHz, equal to the cavity mode half-width, and converted into a frequency noise PSD by means of the cavity discriminator with unit V/Hz, characterised as follows. In order to have a reproducible and precise determination of the voltage-to-frequency conversion factor of the PDH error signal, we modulated the locking set-point of the PDH servo in a closed-loop regime while simultaneously monitoring the cavity transmission signal. The intensity reduction of the transmitted signal may be translated into a frequency shift from the centre of the resonance knowing the cavity mode FWHM. In our case we applied different signals to the cavity PZT at a frequency of 100 Hz to modulate the PDH-locking set-point by 50 and 90 mV, respectively, in the linear response region of the cavity transmission, as represent in Figure 4.6. Since our cavity mode has a FWHM of about 3 kHz, deduced from an empty-cavity ring down

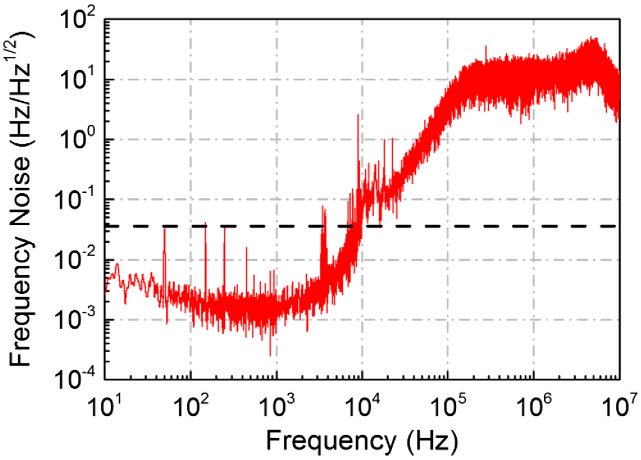

Figure 4.5: Relative frequency noise PSD between laser and cavity rescaled at f_C ~1.5 kHz from the cavity low-pass filtering action [146]. The black dashed line represents the photodetection shot-noise limit that is not measurable at the error point [147], yet it ultimately affects the relative linewidth of the laser locked to the cavity as discussed in the text.

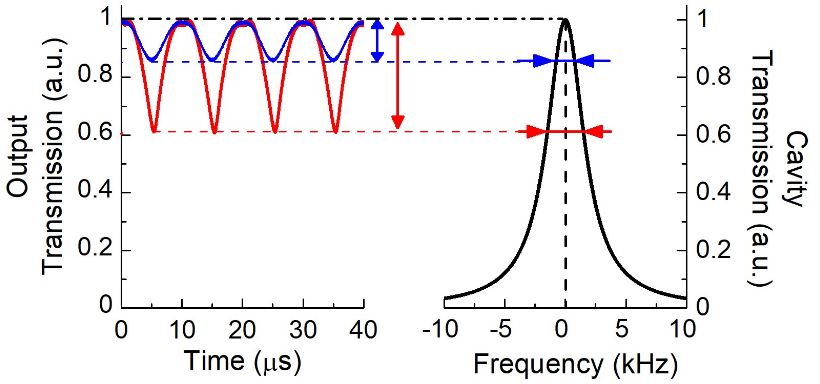

Figure 4.6: Power drop at the cavity output upon dithering at 100 Hz the PDH-locking set-point by 50 mV (blue curve) and 90 mV (red curve). From it, knowing the cavity mode FWHM of about 3 kHz, it has been possible the characterisation of the cavity discriminant [146].

measurement, we retrieved a cavity discriminant of about $3.1{\cdot}10^5$ V/Hz.

Figure 4.5 is consistent with an open-loop gain as represented in Figure 4.7. It derives from the product of different transfer functions charac-

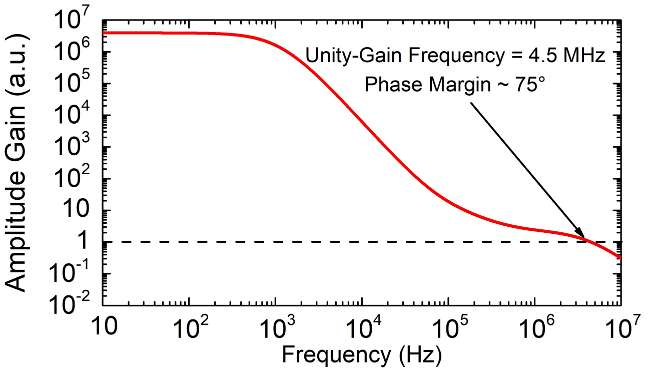

Figure 4.7: Simulation of the open loop transfer function of the PDH-locking system, coming from the product of the transfer functions of the servo PI^2D, the VCO, the SSM and the PDH discriminant, characterised experimentally. The unity gain bandwidth is close to 4.4 MHz with a phase margin of about 75°.

terised experimentally: namely from the PID, the VCO, the SSM and from the PDH discriminant. The PI^2D servo transfer function provides a flat 70-dB gain below 1 kHz, where the laser frequency noise is relatively higher, then it acts as a double integrator stage until a corner frequency of 70 kHz where the gain returns flat. A derivative contribution acts starting from a zero set at 500 kHz that is finally compensated by an upper pole at almost 4 MHz. The frequency actuator receiving the error signal is the SSM driven by the VCO. Since the first has a working bandwidth of more than 20 GHz with sub-ns response time, the main limitation to the application of the frequency correction comes from the transfer function of the VCO related to the introduced delay. We characterised the response time of the VCO to a voltage step function and we found a delay at the 20 ns time-scale. A faster VCO may be used to reach higher bandwidths, but in our case the choice was influenced by the dynamic constraint of counteracting the cavity drifts requiring a tuning range of ±75 MHz for a stable locking over few hours. With more stable cavities, such as thermodynamically controlled or Ultrastable-Low-Expansion (ULE) cavities, a different combination of PID parameters and VCO may be designed to fast the response time of the system. In our case, the unity gain of the simulation is reached at almost 4.4 MHz with a phase margin of about 75°, thus in good agreement with the bump at about 5 MHz in the frequency noise PSD of Figure 4.5.

Considering again Figure 4.5, the remarkable results are the minimum value of the relative frequency noise PSD of 1 mHz/Hz$^{-1/2}$ achieved at frequencies close to 1 kHz, attesting the high noise suppression capability, and the bump at 5 MHz, denoting the high control bandwidth of our PDH-locking system. This high bandwidth is comparable with the best results reported in literature for semiconductor lasers [148]. Apart from residual peak at 50 Hz and odd harmonics due to the power line, the slightly increase of the noise below 100 Hz is related to the cavity flicker-noise contribution, as discussed below for Figure 4.8, whereas the peak at 10 kHz comes from the laser. Taking into account also the photodetection shot-noise, that cannot be observed at the error point as explained in Ref. [147] and that has been evaluated separately as 36 mHz/Hz$^{1/2}$ (black dashed line in Figure 4.5), we found a relative linewidth (FWHM) between the PDH-locked laser and the cavity amounting to $\approx$ 4 mHz, showing the goodness of our tight frequency locking.

To the purpose of quantifying the absolute linewidth of the laser PDH-locked to the cavity, we measured its beat-note with a stable laser having a linewidth of less than 3 kHz over 1 ms (NKT Koheras Adjustik E15) and we analysed the beat-note signal using a frequency-to-amplitude converter followed bt an electrical spectrum analyser. To counteract the relative drift of the two lasers, a slow lock with a bandwidth less than 100 Hz was introduced. Figure 4.8 shows the frequency noise PSDs of the beat-note between the PDH-locked laser and the reference laser, together with the frequency noise PSD of the master laser from datasheet. At frequencies below 2 kHz the frequency noise PSD of the beat-note is higher than that of the reference, which implies that our PDH-locked laser is noisier than the reference due to the mechanical noise of the cavity, especially around 400 Hz. On the other hand, at frequencies higher than 2 kHz, the frequency noise PSD of the beat-note reproduces that of the master, implying that in such region our PDH-locked laser is less noisy than the reference. Using the beta-line

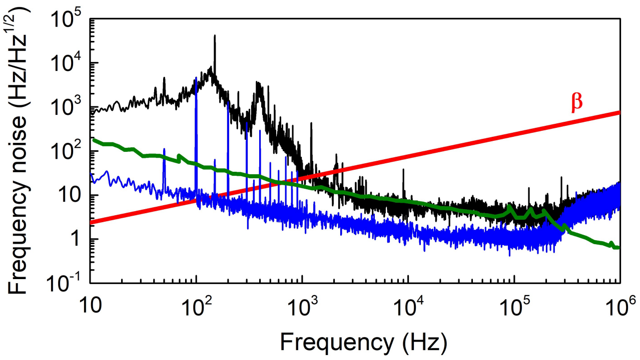

Figure 4.8: Frequency noise PSD of the beat-note between the PDH-locked laser and the master laser (black curve) together with the frequency noise PSD of the master from datasheet (green curve). The measurement has been performed by means of a frequency-to-amplitude converter (with a noise floor represented by the blue trace) followed by an electrical spectrum analyser [146]. The red curve corresponds to the beta-separation line crossing the experimental curve at about 1 kHz (the beta-line method to evaluate the linewidth is reported in Appendix A or Ref. [149], for instance).

evaluation method described in Appendix A, the integrated area of the PSD portion above the beta-line from the crossing point lead to an estimated linewidth of 60 kHz over 100 ms. Let us notice that this is an indicative yet roughly evaluation because of the slow locking condition, indeed the integral below 100 Hz is underestimated but at 100 Hz the servo bump of the locking increases the noise evaluation. Another remarkable result is that the laser remains steadily locked for a few hours without any need of a second feedback loop, until the point where the cavity thermal drifts exceed the ±75 MHz dynamic range.

4.3 Sensitivity Analysis

This section treats the characterisation of the sensitivity of the system through an Allan-Werle deviation analysis at fixed frequencies and through the evaluation of the rms deviation of blank acquisitions over subsequent spectra averaging when performing frequency scans.

The smallest absorption detectable in a CEAS system is written as:

$$\alpha_{min} = \frac{1}{L_{eff}} \frac{\delta I}{I} \tag{4.2}$$

where L$_{eff}$ is the effective interaction length and $\frac{\delta I}{I}$ is the root mean square value of the relative intensity noise, as derived in 3.2.2 from a first order approximation of the Lambert-Beer law. Actually, as $\frac{\delta I}{I}$ varies depending on the observation time, it is worth introducing the Allan-Werle analysis, as described in Appendix A, to infer the Limit Of Detection (LOD) as a function of the integration time T.

Figure 4.9 shows the Allan plot for integration times above 1 ms. Actually lower integration times are not relevant because they are below the response time of the comb-locking servo with a bandwidth of 700 Hz. At 1 ms the Allan-Werle deviation amounts to almost 10^{-3}, it decreases to $8{\cdot}10^{-4}$ at 10 ms and reaches a minimum of $4{\cdot}10^{-4}$ at about 20 ms. From 20 ms to about 10 s the Allan plot remains almost flat at $5{\cdot}10^{-4}$, signature that the system is mainly dominated by a flicker noise contribution mostly due to the detector noise and the residual frequency noise between the laser and the cavity. In a system affected by such dominant contribution, it is convenient to speed up the acquisition of a single spectrum and average over subsequent acquisitions to improve the LOD. This sets the requirements for: i) the choice of the optimum integration time for a single spectral point, ii) the total number of points per spectrum and iii) the overall spectrum acquisition time. As the settling time for a spectral step of about 1 MHz takes about 10 ms, because of the relatively slow feedback loop to refer the cavity-locked laser to the comb, we fixed the dwell time per spectral point at 20 ms, with the acquisition and integration of the cavity output over the last 10 ms only. This translates in a measurement time for a single spectrum composed of 100 spectral points of about 2 s.

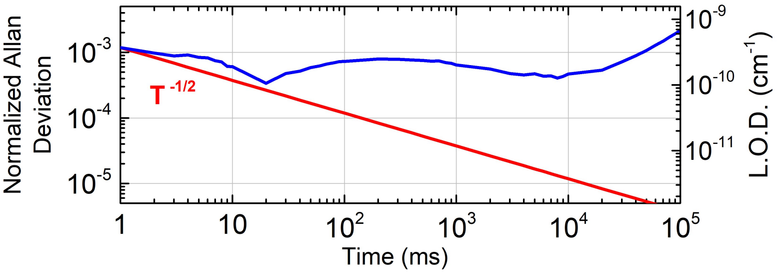

Figure 4.9: Normalized Allan-Werle deviation (left scale) and corresponding Limit Of Detection (right scale) as a function of the integration time T. The red trace is the ideal behaviour that follows the $1/\sqrt{T}$ law.

The comb ensures that repeated acquisitions occur on the same frequency grid, thus making it possible to efficiently averaging many spectra without distortions. We acquired several blank spectra to evaluate the reduction of $\frac{\delta I}{I}$, and thus the sensitivity improvement, by averaging subsequent acquisitions in an Allan-Werle like analysis. It is worth noting that the rms noise of blank spectra is equivalent to the rms deviation of the residuals obtained by the fitting of an absorption feature with the proper profile over the same frequency span. The analysis is reported in Figure 4.10. At N =1, corresponding to a 2-s-long measurement, the rms deviation amounts to $8{\cdot}10^{-4}$,

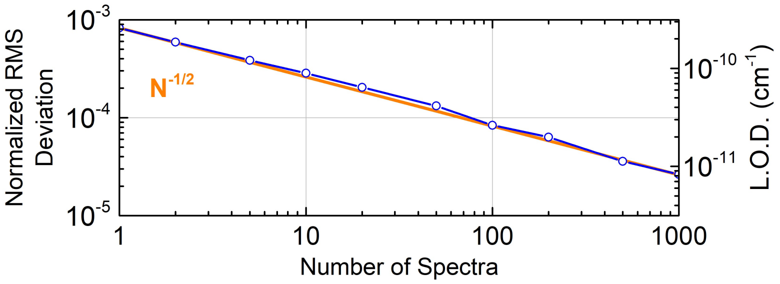

Figure 4.10: Rms deviation $\frac{\delta I}{I}$ per spectrum as a function of the number of acquisitions averaged N. The orange trace is the ideal behaviour following the $1/\sqrt{N}$ law [146].

thus in agreement with the Allan-Werle deviation at 2 s. It decreases over subsequent averaging with no visible deviation from the ideal behaviour following the $1/\sqrt{N}$ law, which is the signature of a normal noise distribution and of the absence of parasitic etalons in the explored frequency span range of about 10 MHz. At N =1000, with a total measurement duration of 2000 s, the rms value is $2.5{\cdot}10^{-5}$ and corresponds to a LOD of $7.8{\cdot}10^{-12}$ cm^{-1}, which is one of the best value reported so far in DC direct detection CEAS employing a widely tunable laser with a linewidth exceeding 100 kHz over 10 ms. Unfortunately, we were not able to fully exploit the sensitivity level given by averaging 1000 spectra because of a relatively high pressure leakage of the cavity of 1.5 Pa/hour when filled with the absorbing medium. Because of it we performed all measurements over 200 s (N=100) achieving a LOD of $2.8{\cdot}10^{-11}$ cm^{-1}.

4.4 Sub-Doppler Spectroscopy on C_2H_2

The following section regards the application of our spectrometer to Molecular Spectroscopy in the Sub-Doppler regime. Usually one of the main technological hurdle in Doppler-free spectroscopy is to reach the saturation of absorption because of the need of: i) high field intensities and ii) a high Signal to Noise Ratio (SNR) to detect Lamb-dip features. Our spectrometer dealt with the previous two requirements, with the adoption of the enhancement cavity and of the wide-bandwidth PDH-locking described above, providing: i) an intra-cavity intensity at the kW/cm^2 level, suitable for saturation even of very weak lines, ii) an absorption sensitivity at a level of 10^{-11} cm^{-1}, appropriate to probe weak overtone lines with a high SNR for both the linear absorption and the non-linear dip signal. Also the employment of a widely tunable ECDL as the probe laser in the region from 1.5 to 1.63 µm makes the system very versatile for the investigation of thousands of overtone lines of several molecules in the Doppler-free regime, from the most intense to the weak ones never explored in this regime.

To test the precision and accuracy of the spectrometer we performed spectroscopic investigations of selected transitions of the 10100-00000 band of acetylene that were already characterised by metrological institutes by sub-Doppler CEAS measurements using Comb-Assisted spectrometers, as described in Chapter 3 or Refs. [4, 5] for instance. We chose three of the less intense lines of the aforementioned acetylene band: the P26e, P28e and P30e featuring transition intensities up to $3{\cdot}10^{-22}$ cm/molecules. Because of their relatively high intensities as compared to the sensitivity of the spectrometer, we adopted particularly low pressures, ranging from 0.2 to 0.4 Pa, to maintain a good transmission signal of about 40% at the cavity output. To avoid strong saturation at these low pressures, we decreased the input power till the level required to have ~1 μW of transmitted power. Thus we set the photodetector gain to 10^6, so that 1 μW of transmitted power corresponded to 1 V. From the transmitted power it is possible to obtain an estimation of the intra-cavity intensity at the level of about 13 W/cm^2, retrieved using the transmission coefficient of the output mirror of $1.1{\cdot}10^{-5}$ and the beam waist of 470 μm.

The spectral points acquisition time was the one selected from the Allan-Werle analysis: wait the system stabilization for 10 ms and acquire the signal for 10 ms, as discussed in the previous section. The adopted pressure is varied from 0.2 Pa for the P26e and P28e line to 0.4 for the P30e line, the previous two slightly weaker than the latter. Figure 4.11a) shows the 100-fold averaged transmission spectrum of the P30e line, together with a Lorentzian fit with free parameters. The dip shows a relative contrast of

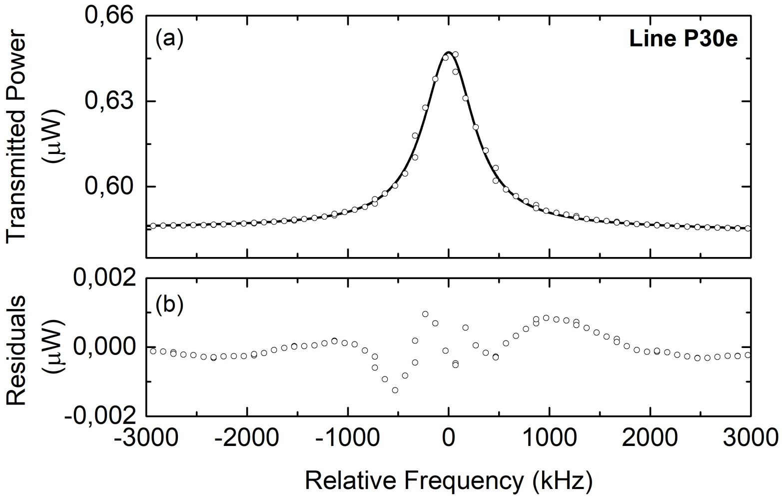

Figure 4.11: Transmission Lamb dip of the P30e line at a pressure of 0.4 Pa obtained from the average of 100 spectra (panel a) and Lorentzian fitting residuals evidencing a slight asymmetry of the line shape (panel b).

about 11%, normalized over the saturated absorption at the dip wings, and a FWHM of about 620 kHz retrieved from the Lorentzian fit. The latter closely matches the following contributions: the first comes from the transit time broadening of about 230 kHz FWHM, calculated from an intra-cavity beam waist of 470 µm for the 50-cm-long cavity with mirrors having a radius of curvature of 1 m using the expression reported in Ref. [150]. The second contribution is due to the collisional broadening at 0.4 Pa of about 220 kHz FWHM, calculated from the pressure broadening coefficient of 0.094 cm^{-1}/atm from the HITRAN database [17]. The last contribution comes from the power broadening of about 180 kHz, calculated using a saturation parameter of about 0.94 that has been estimated from the ratio of the intra-cavity field intensity of about 13 $\mathrm{W/cm}^2$ and a saturation intensity of 13.5 $\mathrm{W/cm}^2$ obtained using Equation (22) from Ref. [151].

Figure 4.11b) shows the residuals of the Lorentzian fitting evidencing an asymmetric deviation from this simple profile. This type of pattern revealed extremely reproducible and seemed the signature of line-shape effects that go beyond the typical Lorentzian assumption. A full study has not been performed, yet we believe that this asymmetry may be related to a combination of transit time effects induced by the curvature of the phase front of light [18, 30] and power broadening effects as discussed in Ref. [6].

The 100 spectra composing the averaged Lamb dip profile of Figure 4.11 have been fitted individually to assess the reproducibility of the centre frequency determinations over an observation time of 2 s, resulting in a rms scattering of the line-centres of 5-7 kHz depending on the set. The latter is consistent with a SNR of the dip close to 100 (the dip contrast is about $6{\cdot}10^{-2}$ over an rms noise of about 10^{-3} as retrieved from Figure 4.9) against a FWHM of about 600 kHz. This implies a precision of the spectrometer of $3{\cdot}10^{-11}$ at 2 s, slightly worse than the typical value of $4{\cdot}10^{-11}$ over the same time scale provided by top-of-the-dip dither-based systems [4, 5], yet the difference and main advantage of our spectrometer is the full access to the dip line-shape which cannot be investigated using AC detection schemes. The overall reproducibility of the system has been evaluated taking into account 25 completely independent sets of 100 consecutively spectra to be averaged, every time emptying-refilling the cavity and resetting the locking servos. The averaged centre frequency retrieved of these 25 sets are reported in Figure 4.12, the error bars represent the scattering of the 100 centre frequencies of the single acquisitions within a given set. Impressively the standard deviation of the weighted mean value amounts to only 1.1 kHz, corresponding to a Type A uncertainty of $5{\cdot}10^{-12}$.

Together with the precision of the spectrometer, we evaluated the contributions to the Type B uncertainty affecting the system. One contribution comes from our frequency comb providing absolute calibration of the frequency axis, where its stability depends on the GPS-Rb reference; for a measurement lasting 200 s its contribution amounts to ~0.19 kHz.

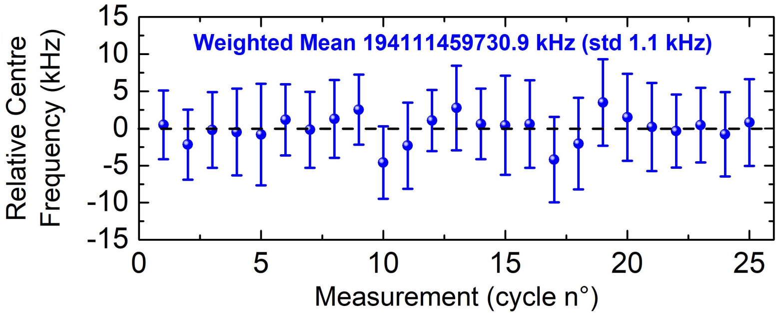

Figure 4.12: 10100-00000 P30e centre frequency values of 25 fully independent set of measurements, each one resulting from the average of 100 spectra, retrieved from Lorentzian fittings. The error bars of each set are the rms deviations of the line centre values from the single acquisitions within a given set [152].

Other two contributions are related to the pressure measurement and pressure stability of our spectrometer. The first depends on the accuracy of the pressure gauge adopted (Ceravac CTR100N), which is at level of 15%. Considering a pressure-shift coefficient of ∼-3 kHz/Pa for the three lines, derived from the analysis of Ref. [153] where the dependence of the pressure shift on the rotational number is accounted for, this leads to ∼0.18 kHz. The second pressure-related error comes from the relatively high leakage of the cavity, discussed in the previous section, of 1.5 Pa/h, causing an additional pressure-induced shift error of 0.25 kHz over a measurement of 200 s. Electronic fluctuations of few mV in the PDH-locking point with a frequency discriminator of $3.1 \cdot 10^5$ V/Hz are negligible, whereas offset drifts of the slow lock for the comb referencing are responsible for another contribution evaluated as 0.2 kHz after monitoring the averaged deviation of the beat-note frequency over a complete frequency scan. Using the power shift coefficient of -11Hz/mW reported in Ref. [154], an intra-cavity power uncertainty evaluated at the level of 20% gives an overestimated contribution of 0.1 kHz. The major contribution to the systematic uncertainty budget is due to the line-shape profile, as in our case a simple Lorentzian fitting cannot fully describe the experimental profile. Since the residual asymmetry is $\sim 1.6 \cdot 10^{-3}$ over a FWHM of about 600 kHz, the estimated contribution is 1 kHz. Table 4.1 shows the summary of the aforementioned systematic errors. The quadrature sum of all systematic contributions leads to a Type B uncertainty of 1.09 kHz. The latter summed up in quadrature with the Type A uncertainty of 1.1 kHz brings to an overall uncertainty of ∼1.5 kHz. A similar analysis have been performed on the other two lines, the P26e and P28e, leading to overall uncertainties of 1.8 and 1.9 kHz respectively.

The three centre frequency values are reported in Table 4.2, together with a comparison with the ones determined by Madey *et al.* at the Cana-

Sources of systematic errors	**Estimated Shift (kHz)**
Frequency reference	0.19
Pressure reading	0.18
Pressure leakage	0.25
Comb-cavity locking point drifts	0.2
Power shift	0.1
Spectral line-shape asymmetry	1
Total Type B uncertainty	**1.09**

Table 4.1: Estimated systematic error (Type B) contributions associated to the line centre frequencies retrieved from the Lorentzian fittings of the Lamb-dips [152].

dian metrological institute [5], exhibiting the lowest uncertainties among the values reported in literature. As the line centre frequencies reported by Madey *et al.* refer to a pressure of 2.7 Pa, we rescaled them to our working pressures using the pressure shift coefficient reported in Ref. [153], giving a total shift of about +7 kHz for line P30e and more than +8 for both P28e and P26e. Another major correction comes from the different detection scheme, the authors of Ref. [5] employed a synchronous detection scheme through a top-of-the-dip locking approach employing a relatively large modulation depth of 1.8 MHz peak-to-peak. In Ref. [154] it is explained that this modulation is responsible for a frequency shift of about -4.7 kHz/MHz$_{pp}$. Since in our spectrometer no modulation is applied, this translates into a correction factor of -8.5 kHz. Since the intra-cavity intensities for both determinations have the same order of magnitude, even if Madey *et al.* adopted a cavity with a lower finesse (∼400), no power shift corrections have been applied. As can be seen from the deviation between the corrected centre frequencies of Madey *et al.* and the values reported in this thesis, the agreement is within the respective uncertainties and is at the kHz level [152]. This is a very re-

Line	Frequency (Madey *et al.* [5])	Shift corrections	Frequency (this work)	Deviation
P30e	194111459735.0(1.9)	+6.9,-8.5	194111459730.9(1.5)	-2.5
P28e	194295440629.5(2.0)	+8.1,-8.5	194295440625.8(1.8)	-3.4
P26e	194476488864.4(2.4)	+8.1,-8.5	194476488862.0(1.9)	-2.1

Table 4.2: Absolute frequencies for the P30e, P28e, P26e lines of the 10100-00000 band of C_2H_2 measured at a pressure of 0.4 for the first transition, 0.2 Pa for the other two. The values are expressed in kHz. The deviation is calculated subtracting from the corrected centre frequency values of Ref. [5], using the pressure and amplitude-modulation shifts reported respectively in the table and discussed in the text, the values of this work [152].

markable result: i) it represents a test of the accuracy of the spectrometer at the kHz level; ii) it shows the necessity of an appropriate calibration of the results acquired in different experimental conditions to have a comparison at the kHz level.

The spectrometer has been also applied to a weak transition to test its ability to extend sub-Doppler investigations to lines never explored so far. The selected line was the P15e of the 01120-00000 band of acetylene, featuring a line strength of $9.468 \cdot 10^{-24}$ cm/molecules and an Einstein A coefficient of 0.005632 Hz, one of the smallest ever explored in the sub-Doppler regime [155]. As compared to the three lines reported above, the P15e line provides a linear absorption a factor of three lower at 0.2 Pa (of about 20% instead of 60%) together with an Einstein coefficient three orders of magnitude lower. Because of it, the input power has been raised until a transmitted power of about ∼57 µW is reached at the cavity output, corresponding to an intra-cavity intensity of more than 1 kW/cm^2. This implies an expected saturation parameter ranging from 0.06 to 0.08 at a pressure of about 0.2 Pa. The gain of the photodetector has been lowered from 10^6 to 10^5, this revealed helpful to reduce the noise level by a factor of 10. We also took care of minimizing ground loops present in the system.

The average of 100 Lamb-dip spectra of the P15e line is reported in Figure 4.13a) at a pressure of 0.2 Pa. The dip contrast is about 0.3% normalized against the saturated absorption signal at the wings of the dip, and the retrieved linewidth is about 390 kHz, negligibly affected by power broadening.

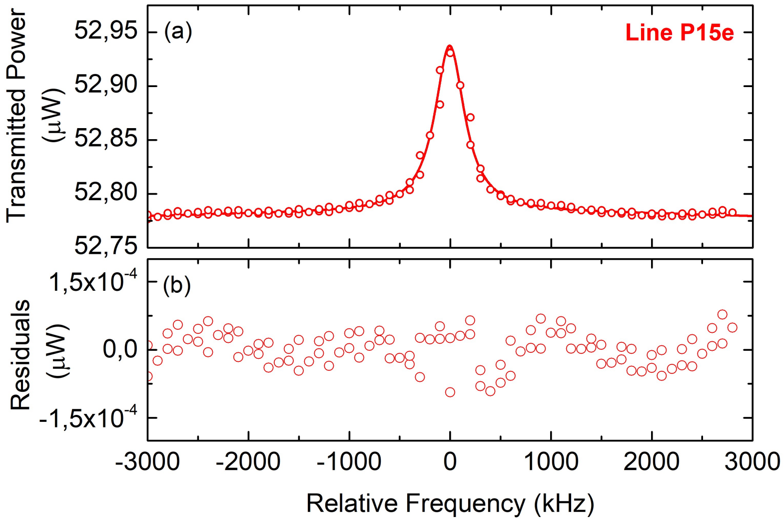

Figure 4.13: a) Lamb-dip profile of the P15e line of the 01120-00000 band of acetylene at a pressure of 0.2 Pa, resulting from the average of 100 spectra. b) Residuals from a Lorentzian fitting of the dip profile [152].

The residuals of a Lorentzian fitting, reported in Figure 4.13b), reflect a normalized rms deviation of about $3.5 \cdot 10^{-5}$. The latter corresponds to a LOD of about $3.1 \cdot 10^{-12}$ cm^{-1} over 200 s, which is one of the lowest reported so far employing a broadly tunable laser in a purely DC cavity transmission detection. Yet we have to point out that at this level of LOD, ground loops strongly affect the detection performances and the working conditions have been found hardly reproducible, explaining why in Section 4.3 the analysis reported was based on typical and more repeatable conditions.

A statistical analysis has been performed on the centre frequency determinations of this weak line. The scatter of the line centres composing a set measurement ranges from 18 to 24 kHz, only a factor of 4 worse than the scatter retrieved within a single set for the lines of the 10100-00000 band, despite the P15e Einstein coefficient is three orders of magnitude lower. An analysis over different independent acquisitions leads to an overall Type A uncertainty of 5 kHz, whereas the systematic contributions are affected negligibly by the different band and are considered at the same level reported in Table 4.1. The overall uncertainty results in 5.1 kHz and the line centre frequency can be expressed as 192248852.795(5) MHz for a working pressure of 0.2 Pa.

The results obtained with the P15e characterisation are particularly promising for extended sub-Doppler absolute calibrated surveys performed on several lines, also ones never saturated before, with an accuracy at the kHz level.

Chapter 5

Comb-Assisted Cavity-Ring-Down Spectrometer: Application to Doppler-Broadening Thermometry

The following chapter is focused on the characterisation of the Comb-Assisted Cavity-Ring-Down Spectrometer developed in this thesis. The guideline was the realization of a sensitive and accurate spectrometer for two purposes: the first is to investigate line-shape profiles and retrieve spectroscopic parameters of high metrological quality. The second is to measure diluted samples or weak absorbers, such as H_2, HD or D_2 of particular interest for the spectroscopic community. For these purposes we adopted CRDS, which is preferred with respect to CEAS to probe low intensity lines in the Doppler-Broadening regime. We developed an innovative acquisition scheme inspired by the Frequency-Agile Rapid-Scanning (FARS) CRDS approach to reach a high sensitivity, comparable with the best values reported in the literature, conjugated with a fast acquisition time, indeed only 6.4 s are needed to probe $\sim$3200 points over 4.2 GHz with a separation of about 1.3 MHz. Absolute frequency calibration is provided by an optical frequency comb used as the reference laser source. The spectrometer has been employed for Doppler-Broadening primary Thermometry (DBT) over an isolated CO_2 transition of the 30012-00001 band, the P12e line at 1.578 µm. We exploited the system high sensitivity and accuracy to perform absorption measurements in the low pressure regime, namely from 0.5 to 7.3 Pa, useful to significantly reduce the systematic uncertainties of the Doppler-width determinations related to the line-shape model, which lead us to the smallest ever observed experimental uncertainty of 8 ppm for a measurement lasting few hours, result reported in Ref. [156]. To validate the precision and accuracy of the spectrometer at the kHz level, we tested its reproducibility on the line centre frequency determinations of the aforementioned CO_2 transition, in particular we deduced the zero-pressure centre frequency and the pressure-shift coefficient and compared them with the most accurate values present in the literature, as reported in Ref. [157].

The chapter is divided into three sections: the first describes the operation principle of the Interleaved-FARS CRDS approach, the optical layout and the performances of the system. The second section regards the application of the spectrometer to DBT, showing the active temperature stabilization of the cavity and the Doppler-width determinations for the P12e CO_2 line. In the last section we report the statistical analysis performed to test the precision and accuracy of the system at the kHz level.

5.1 The Interleaved-FARS Spectrometer

The section regards the basis of the the CRD spectrometer ensuring at the same time: i) a fast acquisition time for few GHz-large spectra, down to a few seconds, ii) an extremely dense spectral grid, with point separation down to few MHz, iii) a high sensitivity, down to few parts 10^{-12} per cm^{-1}.

5.1.1 Conjugating Speed and Dense Frequency Grid

The approach developed in this thesis has been inspired by FARS-CRDS [135] with the aim of improving its performances. As described in 3.3.2, in FARS-CRDS the probe laser is one sideband generated by a high-bandwidth Electro-Optical-Modulator (EOM), PDH-locked to a high finesse cavity, that can be quickly shifted on several cavity modes separated by the cavity Free Spectral Range (FSR) ultimately giving the spectral point separation. The laser is slaved to the cavity whose length has to be calibrated, for instance by an I_2-stabilized HeNe laser. Because of the PDH-locking of the probe laser to the cavity, it is not straightforward to interleave the spectral points to increase the sampling of the frequency grid.

With respect to the original FARS approach, our spectrometer takes advantage of a dither-locking scheme slaving the cavity to the probe laser, in our case the single sideband generated from a Single Sideband Modulator (SSM), without the need of any cavity length stabilization. The dithering locking ensures a relatively good coupling of light provided that the single sideband is shifted either by a multiple of the cavity FSR or by a frequency amount smaller than the capture range of the dithering window. To establish this locking, a saw-tooth signal is sent to the cavity PZT to modulate its length within a range of about ±8.3 MHz ($\sim$1/37 of the cavity FSR) at a frequency of 500 Hz. Also a tracking system is implemented to provide an offset voltage to the PZT to compensate for cavity-length drifts and maintain the dithering window centred with respect to the single sideband frequency, even when performing frequency scans. Thanks to this dithering locking, it is possible to interleave spectral points increasing the density of the frequency grid, which is extremely beneficial to improve the quality of the spectroscopic parameters retrieved from the spectral acquisitions.

The scanning operation principle is illustrated in Figure 5.1. Figure 5.1a) reports some working points of the single sideband linked by arrows highlighting the scan procedure sequence, while Figure 5.1b) shows the cavity modes dither-locked to the probe laser. When a selected number of ring down constants per spectral points is stored, the SSM-driving RF shifts the single sideband by a cavity FSR and this repeats until a FSR-spaced spectrum is acquired. This procedure essentially replicates FARS with the only difference that the tuned frequency is that of generated from the SSM instead from an EOM. The innovative feature of our procedure is related to the dithering locking: after a FSR-spaced spectral scan is over, the sideband frequency is detuned by a small amount ($2\delta f$ in Figure 5.1a)) within the dithering window, in our case by 2.6 MHz, so that the tracking signal changes the cavity length and another FSR-spaced spectrum can be acquired in the reverse direction. Alternating the procedure back and forth, interleaved spectra composed by 3178 points separated by δf=1.3 MHz over 4.2 GHz are acquired in just 6 s. We called our scan approach Interleaved-FARS (IFARS) [157]. As far as we know no other spectrometer have the

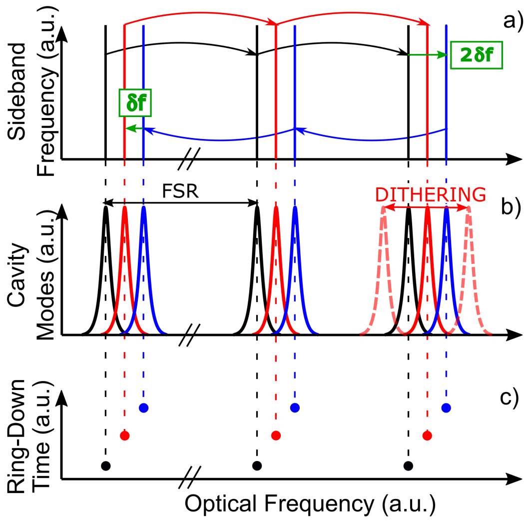

Figure 5.1: a) Set of frequency scanned by the single sideband over some cavity modes represented in b). The colours refer to slightly detuned (by δf,$2\delta f$) cavity modes within the dithering-locking window. c) Saw-tooth behaviour of the acquired ring-down constant depending on a slightly misalignment of the intra-cavity beam as a function of the offset voltage applied to the PZT for the tracking [157].

previous figures of merit. The constraint of 4.2 GHz is the maximum useful frequency interval that emerges from the intersection of the working ranges of the RF generator (Mini-Circuits SSG-6400HS: 0.25-6400 MHz), the RF amplifier (Mini-Circuits ZVE-8G+: 2000-8000 GHz), the hybrid coupler (Krytar 3005070: 500-7000 MHz) and electric switch (Mini-Circuits ZASWA-2-50DR: DC-5000 MHz), respectively, allowing a RF power of about +27 dBm at the SSM input, required to have ~10% of the input laser power, in the range from 1.9 to 6.1 GHz.

A peculiarity of the Interleaved-FARS approach is that the spectral baseline may be affected by a saw-tooth behaviour, as sketched in Figure 5.1c). This behaviour is due to the fact that our scanning procedure suffers from a slight dependence of the ring down time on the cavity length adjusted at every δf,$2\delta f$ jumps. A possible cause may be the presence of tiny misalignments of the intra-cavity beam when the scanning mirror does not move parallel to the optical axis and its reflectivity is not perfectly uniform across the surface. A typical experimental acquisition is reported in Figure 5.2, showing the sawtooth pattern, usually it may also lie on a more typical linear baseline if the cavity finesse is not constant over the explored frequency range. Since this saw-tooth behaviour is highly reproducible, it may be easily fitted away.

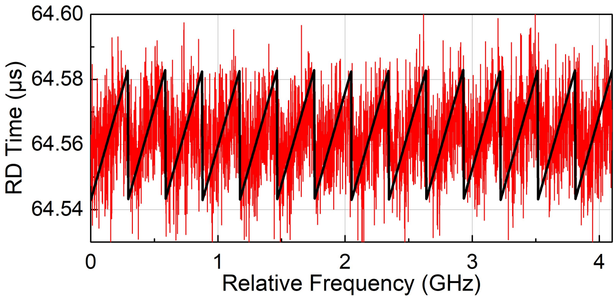

Figure 5.2: Single blank spectrum acquired in 6.4 s over 4.2 GHz with a point-spacing of 1.3 MHz. The black trace is the saw-tooth like fitting function to remove the experimental RD pattern [157].

5.1.2 Optical Layout of the Spectrometer

The spectrometer shares most parts with the CEAS system described in 4.1. This holds for the ECDL, for the SSM generating the single sideband, for the Er:fibre based frequency comb, for the high finesse optical cavity and for the CRIO acquisition board.

The exponential lay-out is shown in Figure 5.3. The ECDL, operating from 1.5 to 1.63 µm, is split by a 10:90 fibre coupler: the low power portion is made to beat with the frequency comb while the high power portion is sent to the SSM.

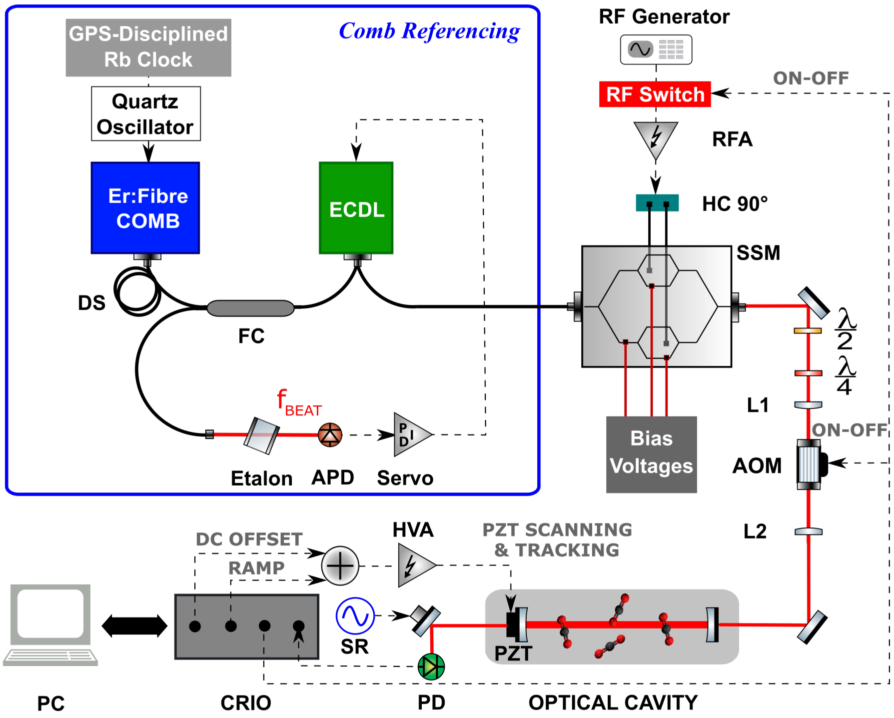

Figure 5.3: Complete representation of the Comb-Assisted Cavity Ring Down system. ECDL: extended cavity diode laser; AOM: acousto-optic modulator; PZT: piezoelectric transducer; FC: fibre coupler; DS: dispersion shifted fibre; HVA: high-voltage amplifier; RFA: radio-frequency amplifier; HC 90°: 90° hybrid coupler; RF Generator: radio frequency generator; RF Switch: radio-frequency switch; SSM: single sideband modulator; L1,2: lenses; SR: Scrambler to reduce fringes; DS: dispersion shifted fibre; APD: avalanche photodetector; PD: photodetector; f$_{BEAT}$: beat-note frequency between the comb and ECDL; CRIO: compact reconfigurable input/output board.

The beat-note frequency f_{beat} with the comb is acquired by an InGaAs APD (Thorlabs APD110C) after been filtered by an etalon (SLS Optics custom model: FSR 44 nm FWHM 1 nm), and its stabilized together with f_{ceo} and f_{rep} of the comb against a primary GPS-referred Quartz oscillator. In particular the feedback loop stabilizes f_{beat} acting on the laser piezo modulation port via a digital servo (Toptica Digilock110) with a locking bandwidth of about 4 kHz. Thanks to a contrast of the beat-note of more about ∼30 dB at 10 kHz of resolution bandwidth, the standard deviation of f_{beat} amounts to 6.5 kHz over an integration time of about 10 ms, affecting the repeatability of the frequency axis to less than 1 part over 10^{11} at 1 s.

The single sideband generated from the SSM acts as the probe beam injected into the high finesse cavity for CRDS, with a typical power of about 2 mW for SSM driving signals of +27 dBm. Using the SSM is beneficial in two ways: i) the tuning can be straightforwardly defined over a predetermined frequency grid with a proper setting of the RF driver; ii) speed and range are only limited by the RF signal generator, and can easily reach the sub-ns and the 20 GHz range, respectively, with top-end devices, iii) the tuning is disentangled from the locking loops for f_{beat}, f_{rep} and f_{ceo} stabilization.

Absolute frequency calibration of the single sideband ν_{SSB} is straightforward knowing the SSM driving frequency ν_{RF}:

$$\nu_{SSB} = \nu_{ECDL} + \nu_{RF} = nf_{rep} \pm f_{ceo} \pm f_{beat} + \nu_{RF} \tag{5.1}$$

when the selected sideband is the one shifted from the optical carrier by $+\nu_{RF}$.

The dithering locking is controlled by the CRIO board, which sends both the sawtooth and tracking signal to the cavity PZT. The board also sends a trigger to an electronic switch (Mini-Circuits ZASWA-2-50DR) to interrupt both the SSM and an Acousto-Optic-Modulator (AOM) driving signals to have a double switch-off of the beam injected into the cavity, allowing a high extinction ratio to observe clean exponential decays without ringing. This happens when an intensity threshold of more than 1.5 V is detected at the cavity output by an InGaAs detector (Thorlabs PDB150C: gain 10^6 V/W and bandwidth 300 kHz). The exponential decay behaviours are acquired point-by-point with a sampling rate of 1 MSamples/s and 16 bits resolution over more than 3.5 times the photon decay time. A decay behaviour is described by:

$$V = V_0 e^{-t/\tau_0} + V_{OFFSET} \tag{5.2}$$

where V_{OFFSET} is the offset voltage of the photodetector which in our case is acquired once, at the beginning of each measurement, and then subtracted from the following decays. A Labview algorithm elaborates in real-time the acquired points: it rejects the first 7 points due to a residual transient behaviour, subtracts V_{OFFSET}, performs a logarithm conversion and a two-parameters least-square linear regression to extract the ring down constant. The linear regression assigns a heavier weight to the first points of the exponential decay, where the SNR is higher, to have a more reliable determination of the Ring Down (RD) constant τ.

Figure 5.4 shows a ring down series acquired and elaborated by the CRIO in real-time together with the dithering signal applied to the cavity PZT (that is an integrated saw-tooth signal due to the PZT capacitance) at a frequency of 500 Hz, implying a RD-rate of 1 kHz. The empty-cavity decay constant is about 64 µs, which implies a mirror reflectivity of 99.9975% and a cavity finesse of about 125000.

5.1.3 Sensitivity Analysis

We firstly characterised the spectrometer at fixed frequency, to evaluate both the short term and long term sensitivity through an Allan-Werle analysis of

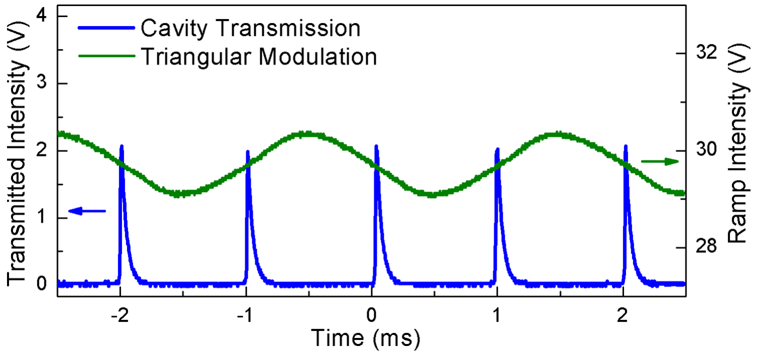

Figure 5.4: A series of ring down events occurring every 1 ms (blue trace), the voltage threshold is set approximatively to 1.5 V corresponding to 1.5 μW, together with the dithering signal sent to the cavity PZT (green trace).

the ring down acquisitions. As discussed in Appendix A, the Allan-Werle plot is useful to choose the integration time per single spectral element and to evidence the presence of temporal drifts of the experimental conditions.

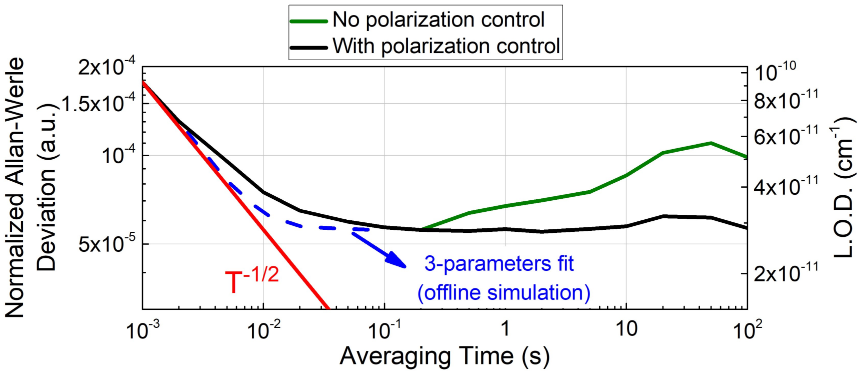

Figure 5.5: Normalized Allan-Werle deviation in the presence of polarization matching (black trace) and without any polarization control (green trace) of the input laser with respect to the more stable cavity polarization mode. The blue dashed-trace shows an off-line simulation of the short-time behaviour when the ring-down decays are fitted using a three-parameters linear regression where the offset is a free parameter.

As can be seen from the green trace of the Allan-Werle plot reported in Figure 5.5, we found a strong contribution affecting the system sensitivity for time-scale higher than 0.1 s when no polarization control of the input light is performed. Indeed as discussed by Huang and Lehmann in Ref. [158], stress-induced linear birefringence and polarization dependent losses of the high reflectivity mirrors are responsible for the lifting of the polarization-degeneracy of the TEM_{00} mode of a high finesse cavity, split-ting two almost linearly polarized and orthogonal modes that affect each other at the cavity output if the input polarization is not properly matched only to one of them. Following the procedure reported also by Burkart in Ref. [159], we clearly saw the polarization mode beating at the cavity output using a rotating polarization beam splitter. With a combination of a quarter-wave and a half-wave plate at the cavity input together with the polarizing beam splitter at the cavity output enables us to properly match the more stable of the two polarization-split cavity modes and to obtain the Allan-Werle plot reported in the black trace of Figure 5.5. The latter starts at $1.77{\cdot}10^{-4}$ for an integration time of 1 ms and decreases following the $\mathrm{T}^{-1/2}$ until almost 2 ms reaching $1.25{\cdot}10^{-4}$, there it departs from the ideal behaviour. We analysed this fact and ascribed it to our real-time fitting procedure that maintains the offset of the photodetector fixed in the elaboration of the RDs from the beginning of every measurement. Indeed acquiring a complete trace of exponential decays and fitting them off-line with a three-parameters linear regression, where the offset is left as a free parameter, the resulting short-time Allan-Werle plot becomes the dashed-line blue trace of Figure 5.5. Since this algorithm requires longer elaboration times than the two-parameters linear regression implemented for our real-time RD acquisition and the sensitivity penalty is acceptable, we decided to maintain the FPGA-based architecture described in the previous section because it is extremely fast and robust. Actually, the Allan-Werle plot decreases until 100 ms where it remains substantially flat at a value of less then $6{\cdot}10^{-5}$ up to 100 s, signature of a dominant flicker-noise contribution that in our case may be ascribed to a combination of the photodetector offset fluctuations and the quantization noise of the acquisition board (of about 300µV from a maximum input range of ±10 V and 16-bit resolution). The corresponding Limit Of Detection (LOD) evaluated as $\sigma_A/(c \cdot \tau_0)$, as derived in Eq.(3.41) where σ_A is the Allan-Werle deviation, is about $3{\cdot}10^{-11}$ cm^{-1} at 100 ms.

In a system dominated by a flicker contribution, it is beneficial to speed up the acquisition of a single spectrum and average over subsequent acquisitions. That is why we selected the single point integration time at 2 ms, corresponding to the averaging of two decay events with different mirror speeds, to leading to the acquisition of a complete spectrum composed by ∼3200 point over 4.2 GHz in less than 7 s. The importance of averaging an even number of RD events per spectral point is fundamental to reduce the Doppler-shift effect at the first order, as it is going to be discussed in 5.2.2.

The second characterisation of the spectrometer regarded the analysis of the baseline rms of blank spectra, over the frequency span of 4.2 GHz, and the gain in sensitivity when averaging subsequent acquisitions. To obtain a flat baseline for every spectra we took care of removing the sawtooth pattern characteristic of the I-FARS approach. Also we implemented a proper fringe scrambler to reduce the impact of interference fringes, where we found a contribution coming from a parasitic cavity as discussed below. Such fringes are evidenced in Figure 5.6a) in a single spectrum acquisition and are further highlighted after 10 averages, as shown Figure 5.6b). Performing a Fast Fourier Transform (FFT) analysis over the spectral trace of Figure 5.6b) we were able to precisely identify the contribution of a single parasitic cavity, with FSR of about 2 m, as the most relevant source of oscillation. It corresponded to the distance between the output cavity mirror and the photodetector. To reduce its effect, we mounted one mirror in the optical path of this parasitic cavity on a PZT (PI, motion characteristic 15 nm/V) and we sent to it a triangular modulation to achieve a shift of $\lambda/4 = 0.8$ µm over a time corresponding to the acquisition of a fringe period of about 150 ms. After an experimental fine tuning of the parameters for fringe scrambling, the RD rms of a single spectrum reaches a value of about $1.8{\cdot}10^{-4}$ as opposed to $6.6{\cdot}10^{-4}$ in the presence of fringes.

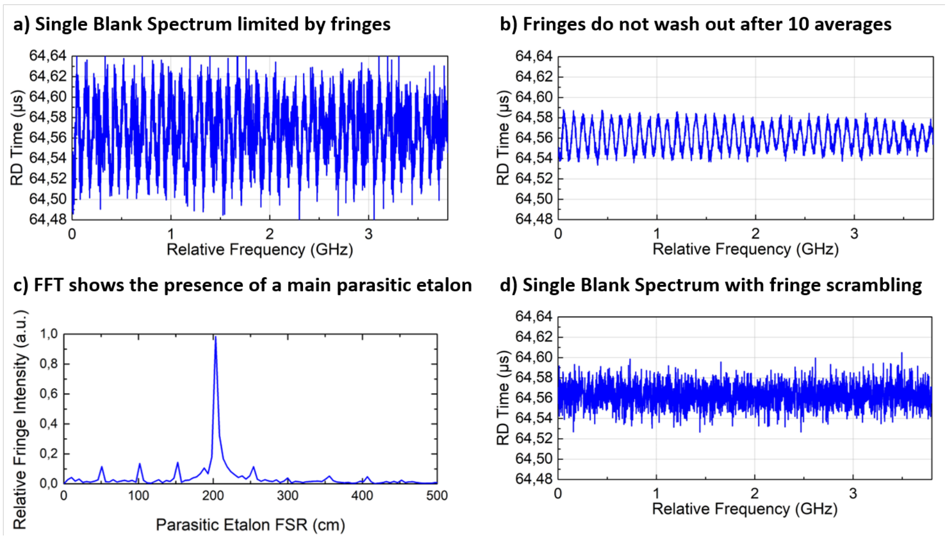

Figure 5.6: a) Single blank spectrum over a span of about 4.2 GHz and b) 10-times averaged spectrum without fringe scrambler. c) A FFT analysis performed on the trace of panel b) shows the FSR of the dominant contribution of about 2 m, which corresponds to the parasitic cavity between the output cavity mirror and the photodetector. d) The use of a fringe scrambler in the optical path of the parasitic cavity efficiently wash out fringes.

The effectiveness of the fringe scrambling is shown in Figure 5.7 where the spectral baseline is reported as a function of the number of empty-cavity spectra averaged.

To better quantify the sensitivity of our spectrometer, we evaluated the rms noise level of the spectra $\sigma_\tau/(c \cdot \tau_0)$ in cm^{-1}, where σ_τ is the standard deviation of the RD-times per spectrum, over subsequent spectra averaging. The equivalent absorption sensitivity per spectral element may be deduced by normalizing the obtained rms-noise-level over the square root of the num-

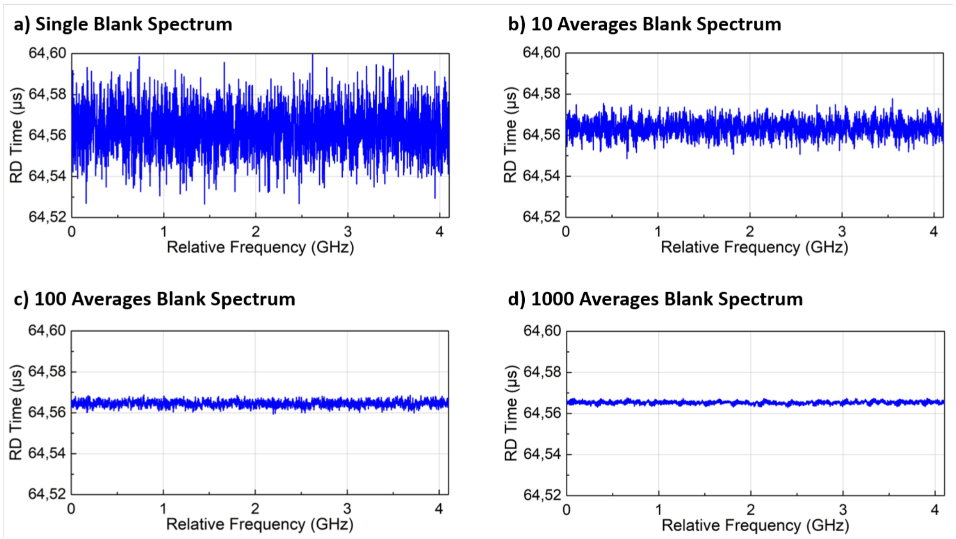

Figure 5.7: a) Single blank spectrum acquired over a span of 4.2 GHz with 3178 points in 6.4 s. b) Spectrum obtained after 10 averages (64 s). c) Spectrum obtained after 100 averages (640 s). d) Spectrum obtained after 1000 averages (6400 s).

ber of spectral elements: $\sigma_\tau/(c\cdot\tau_0\sqrt{N})$. The results are shown in Figure 5.8. Spectra averaging improves the sensitivity of the spectrometer showing only a slightly departure from the $1/\sqrt{N}$ behaviour ascribed to residual parasitic etalons that affect the baseline after averaging more than 10 spectra. The noise level is $9.8{\cdot}10^{-11}$ cm^{-1} at N=1 and reaches the value of $5{\cdot}10^{-12}$ cm^{-1} at N=1000, which is highly satisfactory if one considers the acquisition times of less than two hours. The two corresponding equivalent absorption sensitivities are $2{\cdot}10^{-12}$ cm^{-1} and 10^{-13} cm^{-1} for N=1 and N=1000 respectively, ranking the system among those featuring the best sensitivity.

We have to point out that the previous analysis have been performed in empty-cavity conditions. In the presence of a strong absorption signal the Ring-Down (RD) times may decrease by a factor more than 3, and because of it we decided to employ a non-uniform RD acquisition to achieve an almost uniform Signal-to-Noise Ratio (SNR) at the wings and at the centre of the absorption spectra. In particular the number of averaged RD per spectral points scales from 2 on the spectral wings, to 4 almost 1 GHz away from the centre, 8 on the maximum slope of the absorption profile and 16 in the range of ±150 MHz around the line centre. Also in this case the number of acquisition is even because of the Doppler shift effect. With the non-uniform acquisition scheme, one spectrum is acquired in 17 s instead of 6.4 s and to reach the same sensitivity level shown in Figure 5.8 for the empty-cavity acquisitions the measurement time increases by a factor of 3. Because of it, we selected to average a number of spectra equal to 35 as a trade-off between the sensitivity level of about $\sim 2{\cdot}10^{-11}$ cm^{-1} ($\sim 5{\cdot}10^{-13}$ cm^{-1} as normalized

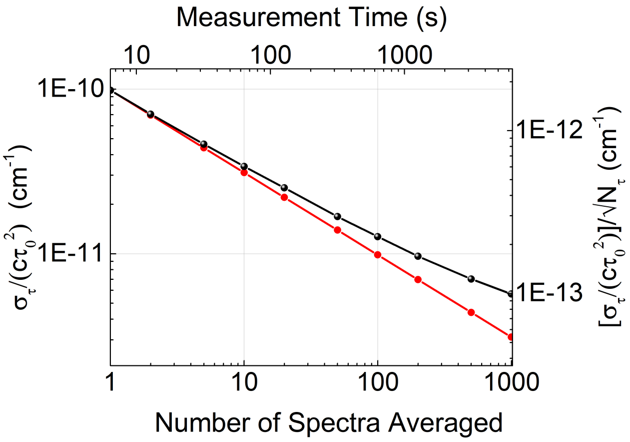

Figure 5.8: Root mean square noise of the blank spectra (left axis in cm^{-1}) as a function of the number of averages (bottom axis) and measurement time (top axis), the red curve follows the $1/\sqrt{N}$ law [157]. The right axis corresponds to the equivalent absorption sensitivity per spectral element, obtained normalizing the rms noise against the square root of the number of spectral points.

over the square-root of the number of spectral point) and the measurement time of less than 10 minutes, to avoid the onset of drifts in the experimental conditions mainly due to cavity leakages of about 1.2 Pa/h.

5.2 Doppler-Broadening Primary Thermometry

The following section regards the application of our spectrometer to Doppler-Broadening-Thermometry (DBT). This primary method is of particular interest because of the upcoming redefinition of the unit kelvin in 2018, where it is going to be deduced from a fixed value of the Boltzmann constant instead that from the physical properties of the triple point of water. The importance of an independent confirmation of other primary methods, such as Johnson noise or dielectric constant gas thermometry, by an optical measurement has been already recognized by the international community.

DBT is based on the linking relation between the Doppler width, that can be probed by an optical measurement, and the thermal energy. By accurate observations of the absorption shapes of a given atomic or molecular profile it is possible to retrieve the Doppler width $\Delta\nu_D$ from:

$$\Delta\nu_D = \frac{\nu_0}{c}\sqrt{8ln2\frac{k_BT}{M}} \tag{5.3}$$

where ν_0 is the central frequency, M the atomic or molecular mass and k_BT the thermal energy. Inversion of (5.3) allows to determine the thermal energy and from it, considering a fixed value of the Boltzmann constant, the thermodynamic temperature. Since T is obtained without any calibration from a master, as required for empirical sensors, this method is referred to as primary.

Historically, the first successful DBT experiment has been performed by Daussy *et al.* [160]. Actually, the best result for DBT determinations on a molecular sample was reported by Fasci *et al.* [7], where the Boltzmann constant was retrieved with a combined uncertainty of 24 ppm over 50 hours using a dual-laser spectrometer and a sophisticated spectral analysis procedure on a rovibrational transition of a water isotopologue at 1.39 µm. Worth of notice is also the work of Cheng *et al.* [161], where acetylene spectra were recorded at 787 nm at 1.5 Pa with a CRD spectrometer achieving the outstanding precision of 6 ppm in few hours, unfortunately affected by a strong systematic deviation of about 800 ppm attributed to weak lines overlapped with the selected transition.

As deeply reviewed in Ref. [96], several aspects have to be taken carefully into account for a successful DBT experiment. Among them, a key role is played by the response linearity of the photodetector and by the the noise level at relatively small optical powers. In this respect, the visible and Near-InfraRed (Near-IR) spectral regions are advantageous because of the excellent performance of Si and InGaAs detectors. The other crucial aspect is the model adopted for the spectral analysis, which has to be sophisticated enough to account for the various collisional effects [162] but also refined and simplified to be implemented into a fitting routine. One way to overcome this hurdle is to resort to a highly sensitive technique in the Doppler-Broadening regime to lower down the gas pressure to the level of about 1 Pa and use simplified line-shape models.

The main objective of DBT is to reach a global uncertainty at the 1 ppm (10^{-6}) level over a measurement lasting few hours. As we are going to show in 5.2.2, our spectrometer represents a promising pathway towards this purpose.

5.2.1 Temperature Stabilization of the Optical Cavity

This subsection describes the control system to maintain the temperature of the cavity stable around a selected set point. Such stabilization is essential for two purposes: the first is to reduce the drifts of the system of thermal origin, the second is to perform different sets of measurement in the same thermodynamic conditions.

As discussed in Chapter 4, to increase the thermal mass of the high finesse cavity it is sandwiched between two Aluminium blocks, designed to be in direct contact over all the cavity surface, and it is isolated from the optical table by two teflon holders. A wooden box is used to store the cavity making its temperature independent from the air conditioning of the laboratory, also it reduces the effect of acoustic noises.

The active temperature control is performed using four silicon-rubber thermofoil heaters (Minco custom model) glued on the Al shell, which provides a good thermal conductivity avoiding direct contact of the heaters to the cavity. Inside the shell three holes were made, two on the bottom left and bottom right respectively and the third on the top centre, to insert 6 cm long high accuracy Pt100 sensors (Tersid custom model) calibrated by the manufacturer against the triple point of water and the gallium melting point, with a total accuracy of 25 mK. The sensors were read by three multi-metres (Agilent 34401A) in a four-wire configuration. We developed a Labview algorithm based on an Arduino UNO PID controller, which output changes the duty cycle of a square-like function to turn on and off the heaters acting on a solid state relè sending a supply voltage of 15 V.

To reduce the effect of gradients, we turned off the pressure gauge connected to the central part of the cavity since slighting increasing the temperature in that region and we used two fans inside the wooden box to increase the temperature uniformity.

A sketch of the control loop system is represented in Figure 5.9.

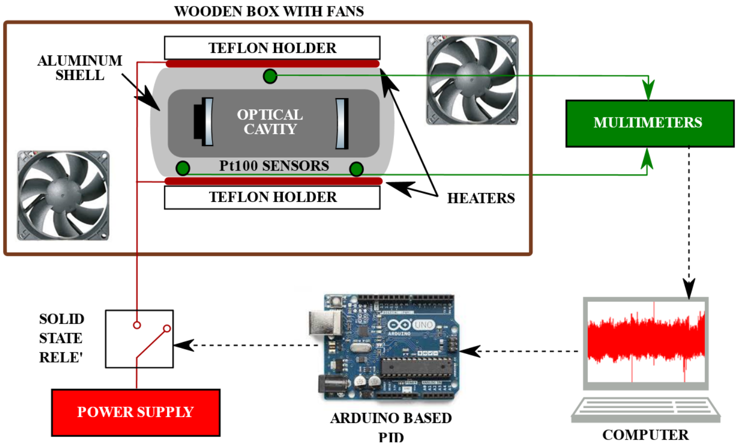

Figure 5.9: Schematic representation of the Labview-Arduino based PID control loop for temperature stabilization of the high finesse cavity.

The reading of the temperature is performed every 1.5 s simultaneously from the three sensors, monitoring the uniformity along the entire length of the cavity-shell. The feedback is closed on the central Pt100 sensor around a set point of 25.3° C (298.45 K). After a fine experimental tuning of the PID parameters, a stability of 3 mK for a measurement lasting more than 5 hours is achieved. Figure 5.10 shows the temperature readings of the central Pt100 sensor over a measurement lasting almost 2 hours showing the aforementioned stability at the mK level. Thanks to the employment of the two fans inside the box, the temperature uniformity is about 6 mK

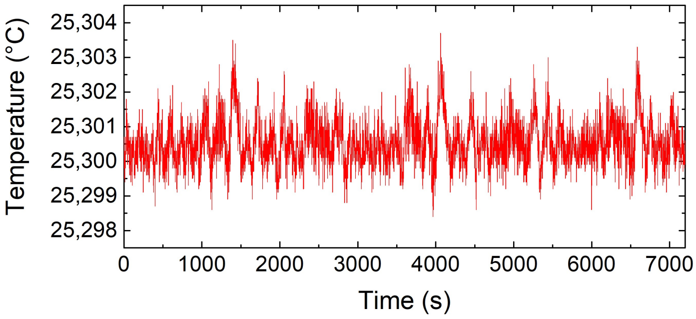

Figure 5.10: Temperature readings (one point every 1.5 s) from the central sensor on the top of the cavity shell over a measurement lasting about 2 hours with a stability at the mK level.

along the cavity shell.

With this good temperature stability and uniformity over few hours that can be maintained over different days, the spectra acquired for DBT have been treated as a statistical ensemble sharing the same thermodynamical conditions.

5.2.2 CO_2 Primary Thermometry

Our Comb-Assisted CRD spectrometer has been applied to DBT since it has been able to provide: i) a high sensitivity, a dense frequency grid, an absolute frequency calibration and a flat spectral baseline, to reduce the statistical uncertainty of the Doppler-width determinations and to explore the few Pa pressure range; ii) a fast acquisition time per single spectrum, to quickly average subsequent acquisition within few hours leading to an accurate determination of the line-shape and select the proper fitting model.

The chosen molecular target is CO_2, which turns out as an excellent choice since: i) it is a centrosymmetric and linear molecule with only three fundamental vibration modes showing a simplified IR spectrum, as compared to that of other polyatomic molecules, ii) its spectral lines do not present any hyperfine structure, iii) it has no permanent dipole moment, circumstance that reduces significantly the interactions with the walls of the gas container [96].

We selected an highly isolated weak overtone transition of CO_2 around 1.578 μm, almost at the centre of the working region of our probe laser, namely the P12e of the 30012-00001 band, whose relevant spectroscopic parameters from the HITRAN database [17] are reported in Table 5.1.

The pressure range adopted in the measurements goes from 0.5 to 7.3 Pa, corresponding to absorption peaks ranging from about $1{\cdot}10^{-7}$ to $1.6{\cdot}10^{-6}$ cm^{-1}. In such conditions, the main contribution to the spectra linewidth comes from the Doppler broadening (of ∼353 MHz), more than three orders

Parameter	**Value**
Centre frequency	6337.990396 cm^{-1}
Line strength	$1.512{\cdot}10^{-23}$ cm/molecules
Pressure broadening coefficient	0.104 cm^{-1}/atm (HWHM)
Pressure shift coefficient	-0.00587 cm^{-1}/atm
Einstein coefficient	0.0078 Hz

Table 5.1: List of the main parameters of the P12e line of the 30012-00001 band of CO_2 from the HITRAN database [17].

of magnitude greater than the collisional width.

The analysis presented below has been performed in collaboration with the scientific group of Professor Livio Gianfrani from the Department of Mathematics and Physics of Second University of Naples (Caserta). We employed a Multispectrum Fitting Procedure (MFP) [163], applied to 33 independent sets comprising 35 spectra acquisitions lasting 17 s each, as discussed in 5.1.3, for a total measurement time of about ≈5 hours. The 33 sets (composed by 35 measurements) are divided into 7 groups of 5 profiles to be averaged, so that 7 spectra are available for each of the 33 pressures. Thus the overall ensemble can be organised in 7 datasets of 33 5-times-averaged profiles for each pressure values. Figure 5.11 reports three spectra of one dataset at different pressures where Signal-to-Noise Ratio (SNR) of the spectra at ∼1 Pa is already 10000, as evaluated from an absorption peak of about $4{\cdot}10^{-7}$ cm^{-1} over a noise level of about $4{\cdot}10^{-11}$ cm^{-1}.

Despite the low pressure regime investigated, the model chosen for the fitting is the Hartmann-Tran Profile (HTP), whose complete form is reported in 1.2.3 or in Ref. [27] for instance, because we found necessary to include the speed dependence of the relaxation rates. The HT profile is particularly useful because: i) it may be implemented into a fitting routine and also using the procedure developed by Ngo *et al.* [26], ii) most of the known line-shape profiles may be retrieved fixing some of its seven parameters. Also the absorption coefficient $\alpha(\omega)$ may be expressed as:

$$\alpha(\omega) = (P_0 + P_1\omega) + \alpha_{TOT} HTP(\omega) \tag{5.4}$$

where P_0 and P_1 account for background variations of instrumental nature and α_{TOT} is the integrated absorption coefficient. With the MFP procedure we applied physical constraints between some of the HTP parameters, leading to a reduction of their statistical correlations and to more accurate determinations. In particular the collisional width Γ_0 and shift Δ_0 have been considered linearly dependent from the sample pressure, and thus on the integrated absorption coefficient α_{TOT}. Regarding the velocity-changing collision frequency (β) and the correlation parameter (η), they did not improve the quality of the fittings if considered as free parameters or set to

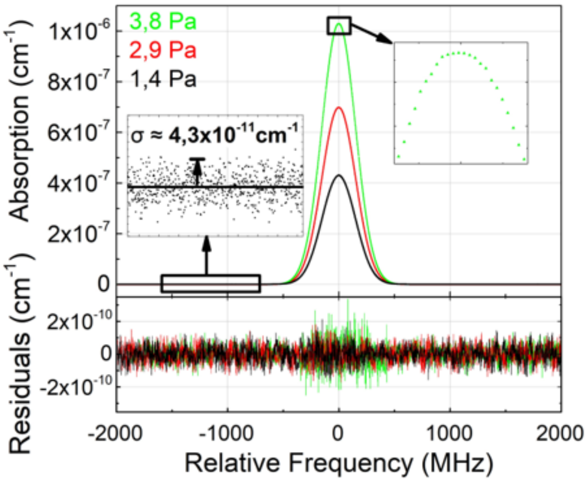

Figure 5.11: Three averaged spectra at different pressures, each spectrum is obtained from the average of 5 consecutive profiles [156]. The two insets highlights the dense spectral point sampling and standard deviation on the spectra wings. The bottom panel shows the residuals of a Speed-Dependent Voigt Profile (SDVP).

zero, implying that in our experimental conditions the absorption may be descried by the Speed-Dependent Voigt Profile (SDVP). A confirmation comes from the residuals shown in Figure 5.11, where using the SDVP no evident features are visible except of an increased noise at the centre of the spectrum due to reduced SNR for the RD acquisition. Also with the SDVP the fitting parameters related to the quadratic collisional width and shift are returned with physical values consistent with a quadrupole-dipole interaction.

MFP has been applied to the 7 datasets leaving the 33 temperatures of the spectra at different pressures as free parameters. The seven absolute mean temperatures are reported in Figure 5.12. Every dataset point is affected by a statistical uncertainty (Type A) of 6 mK which corresponds to 20 ppm; notice that this value is remarkably low considering that the cavity temperature stability is about 3 mK. The weighted mean of the absolute temperatures of 298.517 K is retrieved with a standard deviation of 2.4 mK corresponding to 8 ppm, this value is one the best reported so far for a measurement lasting only ∼5 hours. For a sake of comparison 3.2 ppm were obtained with ammonia over 70 h [164] and 6 ppm with acetylene over few hours with a CRDS approach [161].

We evaluated the error budget considering the following systematic (Type B) errors. The frequency scale uncertainty of our spectrometer is 0.2 kHz given by the GPS-disciplined clock over 10 minutes, affecting the measurement with 0.5 ppm. The linearity of the detector and of the acquisition board were measured independently and give a cumulative effect of 2.3 ppm in the IR region close to 1.578 μm. The instrumental spread function coming

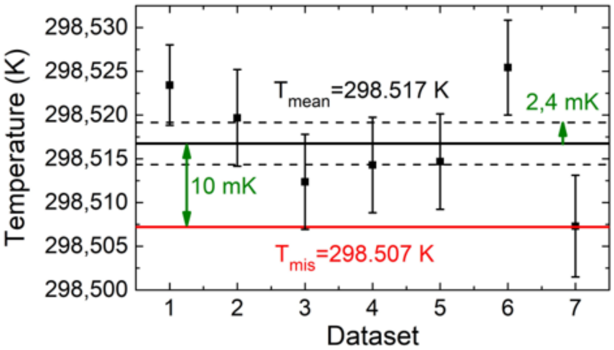

Figure 5.12: Seven absolute mean temperatures retrieved from the MFP of the datasets using the SDVP [156]. The overall mean temperature of 298.517 K (black horizontal line) is affected by a statistical uncertainty of 2.4 mK (8 ppm). It is retrieved with an offset of 10 mK (33 ppm) with the value read from the central Pt100 sensor (red line), the latter affected by an accuracy of 25 mK (80 ppm).

from the linewidth of our laser (of the order of 100 kHz over 10 ms) affects the error budget by 0.2 ppm since it is a Gaussian contribution which is added in quadrature in the convolution with other Gaussian profiles. The saturation of the P12e line has been investigated as a possible source of systematic error, but thanks to a weak Einstein coefficient (0.0078 Hz) it is mitigated and a saturation broadening varying from 0.3 ppm to a maximum of 1.6 ppm, depending on pressure, has been calculated in the approximation of a steady-state coupling (which is not the case of CRDS except during the build-up condition).

The two main contributions to the error budget come from the line-shape model adopted and the Doppler-shift that the intra-cavity field experiences during the ring down decays because of the reflections from a moving mirror. The first has been estimated comparing the mean temperature from the 7 datasets adopting the SDVP and a more sophisticated HTP where the velocity changing collision frequency (β) and the correlation parameter (η) are fixed to values given by the diffusion theory (1.03 MHz/Torr) and specific of the CO_2 band (0.273) [165], respectively. The discrepancy between the DBT determinations is about 10 ppm, which can be considered as an excess estimation of the systematic contribution of the SDVP model adopted. The second contribution has been evaluated by numerical simulation using the model discussed in Ref. [144]. The Doppler shift effect causes a distortion of the absorption profile that can be seen at the first order when sampling Ring Down (RD) events from a mirror moving only in one direction, such as in the left or right directions, namely towards or away from the incoming field. The mirror speed has been evaluated taking into account the peak-to-peak voltage of the sine-like function monitored when a triangular ramp is applied to the PZT. Here we found a slightly asymmetry leading to two different velocities for the mirror moving in the left and right directions, respectively, of about 47.01 µm/s and 47.07 µm/s. We performed spectra measurements at a pressure of 2.6 Pa sorting the RD events for the mirror moving in the right and left directions. The residuals of the fits of the spectra are shown in Figure 5.13a) e b) for the events acquired with the mirror motion on the left and on the right respectively. In red we report the simulations of the residuals from the numerical model using the aforementioned mirror speeds, showing good agreement with the experimental results. The distortion has peak excursions of about $\sim 8 \cdot 10^{-10}$ cm^{-1}, clearly detectable by our spectrometer. Since in our case the mirror speeds for the two directions are almost the same and an even number of RD-times are averaged together at each spectral point, this distortion is removed at the first order, as can be seen from the residuals of Figure 5.13c), but it remains at the second order affecting both the line-width and the line centre frequency determinations, the latter discussed in the following subsection. At each pressure we

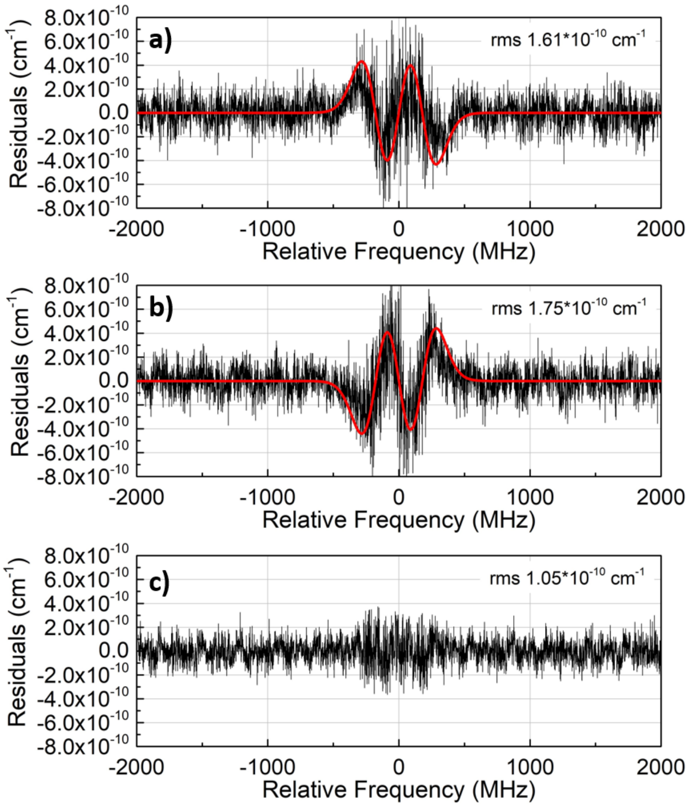

Figure 5.13: Experimental and simulated residuals of a spectrum acquired at 2.6 Pa sorting the RD events depending on the mirror moving directions, a) for mirror moving in the right and b) in the left direction. Panel c) shows the residuals when an even number of RD events are averaged for different mirror speeds, resulting in a first order compensation of the distortion.

evaluated this second order distortion taking into account the mirror speed, the cavity finesse, the acquisition time and the fitting procedure of the RD events. The retrieved systematic deviations as a function of pressure are reported in Figure 5.14. A maximum discrepancy of 48 ppm may be reached

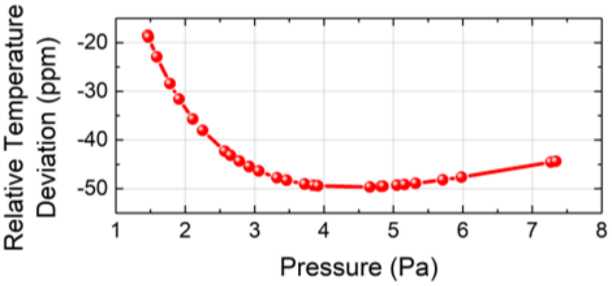

Figure 5.14: Systematic deviations on DBT determinations induced by the Doppler shift from the moving mirror at second order. A maximum discrepancy of 48 ppm is reached for pressures above 3.5 Pa.

but, thanks to the accurate modelling, its impact is reduced to less than 10% giving a contribution to the error budget of about 4.8 ppm.

Uncertainty source	Type A	Type B
Experimental reproducibility	8 ppm	
Frequency scale		0.5 ppm
Laser linewidth		0.2 ppm
Detector + Acquisition board linearity		2.3 pp
Saturation broadening		0.3-1.6 ppm
Line-shape model		10 ppm
Second order Doppler-shift		4.8 ppm

Table 5.2: Error budget of the DBT determinations [156].

Both the Type A and Type B error contributions are summarized in Table 5.2. Their quadrature addition results in an overall uncertainty of 14 ppm achieved in a measurement lasting ∼5 hours, which is almost 2 times better than the best result reported so far [164], ranking our spectrometer at the first place among optical methods and paving the way towards DBT determinations at the 1 ppm level over practical times.

5.3 Precision and Accuracy of the Spectrometer

The same measurements acquired for DBT, which is particularly wide, has enabled us to test the precision and accuracy on the line centre frequency determinations.

We employed an Allan-Werle deviation analysis to evaluate the improvement of the precision in the line centre frequencies as a function of the spectra averaged, as sketched in Figure 5.15. The plot shows that for the two different pressure conditions the precision over the single determination is less than 10 kHz, in particular at the higher pressure (with a higher SNR) it is almost 4 kHz, corresponding to 2.1 parts over 10^{11}. The latter is one of the highest precision reported so far for a measurement lasting about 17 s in the Doppler-broadening regime, comparable to the precision provided by sub-Doppler spectroscopy over 1 s, as reported in Ref. [6] for instance. Interestingly it can be seen that the precision reaches a value close to the sub-kHz but does not follow the ideal behaviour, as it is better evidenced at the higher pressure. We ascribed this fact to slight drifts of the slow locking of the ECDL to the nearest comb mode affecting the determination at the sub-kHz level over few seconds. One possible solution is to upgrade the system with a phase-locking of the ECDL to the comb instead of a frequency locking.

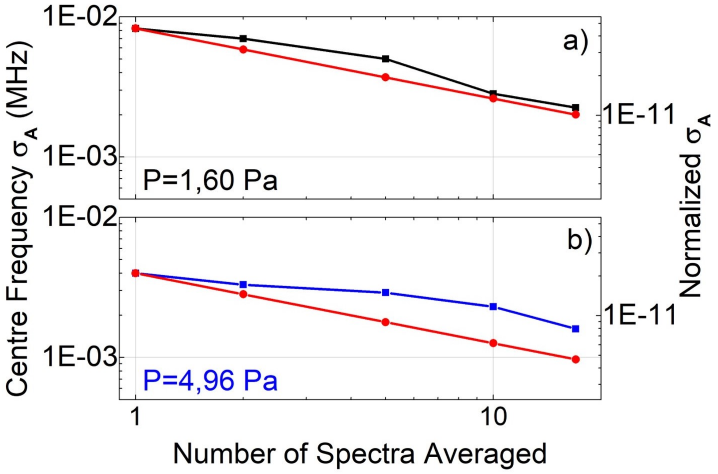

Figure 5.15: Allan-Werle deviation on the retrieved centre frequency as a function of the number of spectra averaged for two datasets, one at 1.6 Pa and the other at 4.9 Pa [157].

The reproducibility of the spectrometer has been evaluated from the behaviour of the line centre frequencies of the 35-times averaged spectra at the 33 different pressures. The results are shown in Figure 5.16. Every point corresponds to the mean value obtained from the fitting of 35 averaged spectra, whereas the error bars correspond to the value of the Allan-Werle deviation plot at N=17.

The slope coefficient obtained from a weighted linear fit of Figure 5.16 is -2.80±0.42 kHz/Pa and corresponds to the self-induced pressure shift coefficient. If we compare our result with the most accurate value reported

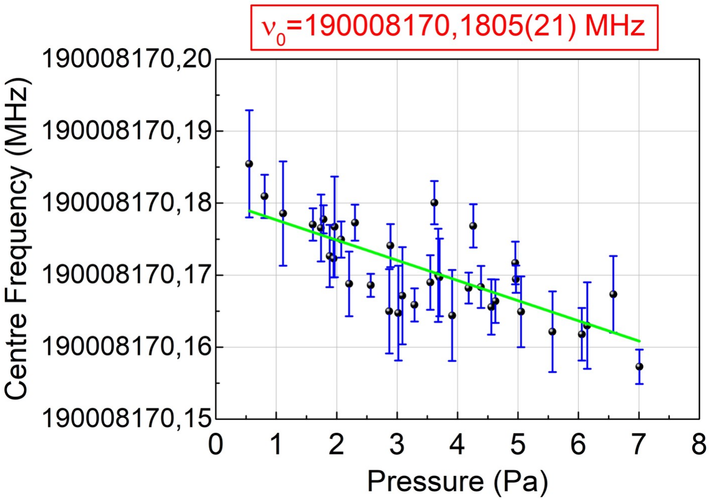

Figure 5.16: Centre frequencies from independent sets at different pressures, every value is extracted from the average of 35 profiles and the error bars correspond to the precision retrieved from the Allan-Werle plot at N=17(35/2) [157].

for this line, that is equal to -1.49±0.02 kHz/Pa [166], the agreement is only within 3σ. We ascribed this discrepancy to the pressure regimes adopted differing by about 4 orders of magnitude. The possible difference of the pressure shift coefficients in the few Pascal pressure range with respect to the values obtained at higher pressure is a very interesting topic for the spectroscopic community and is ongoing further investigations.

The linear fit allowed us to extrapolate a zero pressure line centre frequency of 190008170.1805 MHz with a statistical (Type A) uncertainty of 1.6 kHz. In terms of systematic (Type B) uncertainties the main contributions comes from: i) the frequency stability of the GPS-based reference oscillator of about 0.6 kHz, ii) the accuracy of the absolute pressure gauge of 0.4 kHz, iii) the cavity leakage of 0.16 kHz and iv) the Doppler shift at the second order evaluated as 1.2 kHz as described below. The Doppler shift is one of the main causes of Type B uncertainty affecting the line centre frequency determinations [144]. Considering the spectra obtained fitting only one family of RD-times with the mirror moving in the left or right direction, as reported in the previous subsection, the retrieved centre frequencies differ from about 1.8 MHz, each one ±900 kHz away from the unperturbed value. When averaging an even number of RD events, caring of mixing the same number for the two different mirror motions, the distortion is reduced at the first order but still it affects the line centre frequency determination due to the slightly difference between the two mirror speeds. The second order Doppler shift distortion causes an estimated difference between the unperturbed value and the one retrieved from our experimental measurements of 1.2 kHz, as obtained considering the difference of the two mirror speeds of about 0.06 µm/s and comparing it with the shift of about 900 kHz for a mirror speed of about 47 µm/s.

The overall uncertainty is obtained from the quadrature addition of the Type A contribution of 1.6 kHz and of the Type B of 1.4 kHz resulting in 2.1 kHz, and our retrieved zero pressure line centre frequency may be written as 190008170.1805(21) MHz. We compared our value with the others present in the literature, namely from the HITRAN database [17], from Ref. [166] obtained by a Fourier-transform measurement and from Ref. [167] deduced by a FARS-CRD spectrometer. Table 5.3 shows the comparisons with those values and the one retrieved in this thesis. With respect to HITRAN and Devi *et al.* the deviation is within 1σ of their declared uncertainty, with a difference of 1.78 and 0.67 MHz respectively, whereas the deviation from the comb-calibrated value of Long *et al.* is 79 kHz which corresponds to more than 2.5σ of their uncertainty (approximately one order of magnitude greater than the one obtained in this work).

	Centre frequency (MHz)	Uncertainty (kHz)	Deviation (kHz)
This work	190008170.1805	2.1	...
HITRAN [17]	190008171.960	300-3000	-1780
Devi *et al.* [166]	190008170.850	600	-670
Long *et al.* [167]	190008170.101	30	79

Table 5.3: Absolute frequency comparison between the value of this work [157], the one from the HITRAN database [17], Devi *et al.* [166] and Long *et al.* [167]. The deviations are calculated as the centre frequency of this work minus the ones from the other references.

As a conclusion, the previous analysis has attested the precision and accuracy of the spectrometer at the kHz level, in particular we have demonstrated the achievement of a precision down to 4 kHz for a measurement lasting less than 20 s, which is one of the best result obtained without recurring to sub-Doppler regimes.

Conclusions and Future Perspectives

In this thesis we have described the realization and characterisation of two spectrometers: the first based on CEAS which has been employed for highly accurate saturated spectra acquisitions enabling line-shape analysis in the sub-Doppler regime, the second relying on CW-CRDS that has been used for molecular investigations in the Doppler regime with the fundamental application of DBT.

Concerning the CEAS spectrometer, its strengths are: i) The very tight Pound-Drever-Hall (PDH) locking which provides high Signal-to-Noise Ratios (SNRs) in a purely DC acquisition scheme, particularly useful for sub-Doppler profile analysis. Indeed the latter is not straightforward when employing a CRDS approach because of the need to discriminate two decay constants. ii) The use for the first time of a Single Sideband Modulator (SSM) as a frequency actuator for a single-loop PDH-locking, featuring a wide-bandwidth of about 5 MHz and a capture range of 150 MHz to maintain a stable locking of the probe laser to the cavity for few hours. iii) The kHz level repeatability on the line centre frequency determinations for measurements lasting few seconds and the agreement at the kHz level with measurements performed by metrological institutes. iv) The chance to saturate a very weak Einstein coefficient transition, demonstrating the possible application of the spectrometer for broad surveys, even on weak lines, in the Doppler-free regime.

With respect to the CRDS spectrometer, its main features are: i) The combination of an Interleaved Frequency Agile Rapid Scanning (I-FARS) approach and a cavity dithering locking, suitable to conjugate acquisition speed and a dense frequency grid. The first interesting on one hand to investigate low pressure avoiding the onset of drifts in the experimental conditions, on the other hand to work at the minimum of the Allan-Werle deviation. Whereas the dense frequency sampling is particularly useful for line-shape analysis to select the proper fitting model and extract parameters of high metrological quality. ii) The application to Doppler-Broadening Thermometry, with an active temperature stabilization of the cavity providing a few mK deviation over few hours, and with the choice of an isolated molecular transition together with a Multi-spectrum Fitting Procedure (MFP) accounting for the speed dependence of the relaxation rates even in the few Pascal pressure range. iii) The precision and accuracy on the retrieval of the line centre frequency, comparable to the best results reported in the literature.

In the future the CEAS spectrometer is going to be applied for: i) the saturation of molecular transitions, even ones never observed, of molecular samples of particular interest in many applications, such as CH_4 in the $2\nu_3$ band; ii) the study of the Doppler-free profiles focusing on transit time, power broadening and speed-dependent effects causing an asymmetry of the sub-Doppler line-shape. Also an upgrade of the system may be performed employing the Noise Immunity Cavity Enhanced Optical Heterodyne Molecular Spectroscopy (NICE-OHMS) technique.

An outlook of the CRDS spectrometer regards on the one hand its application to Doppler-Broadening Thermometry (DBT), where the system could be stabilised at the triple point of water and where an upgrade of the dithering locking could be implemented to further minimise the distortion of the absorption profile caused by the Doppler shift effect at the second order. On the other hand the spectrometer may be used for investigations of absorption transitions of light diatomic molecules, such as H_2, HD or D_2 of particular relevance for the spectroscopic community, to be compared to *ab initio* calculations both for the molecular energy levels and for the line-shape profile in the presence of collisions, which are possible only for molecules featuring a simple structure.

Appendix A

Frequency Noise of Laser Sources

This Appendix is an overview about frequency noise of laser sources. The analysis of frequency noise is a fundamental topic, studied since the first invention of lasers to better understand their frequency domain structure and their time-domain behaviour. The optical spectrum of a laser oscillator depends on the noise processes associated with the laser itself.

Let us consider an ideal monochromatic oscillator without any noise terms, described in the time-domain by the following electric field amplitude:

$$E(t) = E_0 \cos(\omega_0 t + \varphi_0) \tag{A.1}$$

where E_0 is the maximum field amplitude, ω_0 is the angular frequency and φ_0 is the initial phase of the oscillation. Due to different noise contributions even a single-frequency laser does not consist of a perfect sinusoidal oscillation of the electric field. The two main categories of noise are: quantum noise (in particular spontaneous emission from the gain medium and cavity quantum losses) and technical noise (related to the mechanical and thermal perturbation of the laser cavity). Since these noise sources generate random fluctuations of the laser phase in the time domain ($\varphi(t)$), the field amplitude oscillations evolve in time as:

$$E(t) = E_0 \cos(\omega_0 t + \varphi(t)) \tag{A.2}$$

From Eq.(A.2) is possible to derive the instantaneous angular frequency:

$$\omega(t) = \frac{d(arg[E(t)])}{dt} = \frac{d(\omega_0 t + \varphi(t))}{dt} = \omega_0 + \frac{d\varphi(t)}{dt} \tag{A.3}$$

Frequency fluctuations $\Delta\nu(t)$ are related to phase fluctuations $\Delta\varphi(t)$ by:

$$\Delta\nu(t) = \frac{1}{2\pi}\frac{d\Delta\varphi(t)}{dt} \tag{A.4}$$

which shows that phase noise translates intrinsically into frequency noise, being the two just different manifestations of the same physical process.

A deeper understanding of the frequency noise of a laser uses the Power Spectral Density (PSD) function which allows to analyse the different spectral contributions coming from the overall noise process. From the basic analysis performed by Wiener and Khintchine [168], their theorem states that the PSD is the Fourier transform of the autocorrelation function of the variable considered. The autocorrelation function for frequency fluctuations is:

$$R_\nu(\tau) = \lim_{T\to\infty} \frac{1}{2T} \int_{-T}^{T} \nu(t+\tau)\nu^*(t)dt \tag{A.5}$$

where * refers to the complex conjugate. The frequency noise PSD has then the expression:

$$S_\nu(f) = 2\int_0^\infty R_\nu(\tau)e^{-i2\pi f\tau}d\tau \tag{A.6}$$

expressed in $\mathrm{Hz}^2/\mathrm{Hz}$. Equation (A.6) considers the frequency noise PSD as a single-sided function, with the positive real frequency axis as its domain. The factor of two comes from the conversion of a double-sided function into a single-sided with the same integrated area, as commonly used in practice. When measuring the stability of an oscillator, the parameter considered is the phase noise PSD, which decompose the underlying phase modulation processes in the spectral interval $f + df$. Exploiting the relation (A.4) it is possible to derive the phase noise PSD, in $\mathrm{rad}^2/\mathrm{Hz}$, from the frequency noise PSD, which reads as:

$$S_\varphi(f) = \frac{1}{f^2}S_\nu(f) \tag{A.7}$$

Some of the most known noise processes are characterized by frequency noise PSDs which are polynomial functions of the Fourier frequency f, and the same happens for the phase noise PSDs taking into account the scaling factor of (A.7). Typical examples are white frequency noise (the one possessed by laser sources with random walk of phase) characterized by $S_\nu = const.$, and flicker noise (mainly due to the electrical sources driving the laser) characterized by $S_\nu \sim 1/f$. The reader interested in a complete treatment on several other phase-frequency noise processes may refers to [169].

Let us now introduce a new variable, $L(f)$, defined as the ratio between the power in the noise floor (within 1 Hz area) and the total power in the carrier:

$$L(f) = \frac{P_{noise}}{P_C} \tag{A.8}$$

with unit 1/Hz, or in logarithm scale dBc/Hz. It is possible to demonstrate that the relation between $S_\varphi(f)$ and $L(f)$ is:

$$S_\varphi(f) = 2L(f) \tag{A.9}$$

which comes from the fact that $L(f)$ considers only one side of the carrier noise, but the complete value is its double. The total phase variance σ_φ^2 can thus be obtained by:

$$\sigma_\varphi^2 = \int_0^{+\infty} S_\varphi(f)df = 2\int_0^{+\infty} L(f)df \tag{A.10}$$

From σ_φ it is possible to retrieve the fraction of the total power stored in the coherent carrier with the following relation:

$$P_C = e^{-\sigma_\varphi^2} P_{TOT} \tag{A.11}$$

The ratio P_C/P_{TOT} is useful to compare how much the frequency noise of a laser source is reduced by a linewidth-narrowing process, for instance. An example is given by coherence transfer experiments, where the frequency stability of a narrow laser, acting as the master, is transferred to a noisier one, considered as the slave. The goodness of this coherence transfer can be evaluated by acquiring the beat-note between the master and the phase-cloned slave and measuring the amount of power in the coherent peak using Eq.(A.11).

The previous dissertation about frequency noise can be useful for the determination of the spectral line-shape of a laser in the optical frequency domain. Let us start to demonstrate the relation between the frequency noise PSD, $S_\nu(f)$, and the electric field PSD, $S_E(\nu)$ [169]. $S_E(\nu)$ is defined as:

$$S_E(\nu) = 2\int_{-\infty}^{+\infty} R_E(\tau)e^{-i2\pi\nu\tau}d\tau \tag{A.12}$$

where $R_E(\tau)$ is the autocorrelation function of the electric field:

$$R_E(\tau) = \lim_{T\to\infty}\frac{1}{2T}\int_{-T}^{T} E(t+\tau)E^*(t)dt \tag{A.13}$$

Without entering in the complete analytical procedure, reported in Ref. [169] for instance, the autocorrelation function $R_E(\tau)$ can be rewritten in terms of the phase jitter $\Delta\varphi(t,\tau) = \varphi(t) - \varphi(t-\tau)$ as:

$$R_E(\tau) = \lim_{T\to\infty}\frac{1}{2T}\int_{-T}^{T} e^{i\Delta\varphi(t-\tau)}\left(e^{i\Delta\varphi(t)}\right)^* dt \tag{A.14}$$

and, exploiting a relation between the phase fluctuations $\Delta\varphi(t)$ and the frequency noise PSD, it is possible to obtain the link between $S_\nu(f)$ and $R_E(\tau)$:

$$R_E(\tau) = E_0^2 e^{-2i\omega_0\tau} e^{\int_0^{+\infty} S_\nu(f)\frac{\sin^2(\pi f\tau)}{f^2}df} \tag{A.15}$$

Consequently $S_E(\nu)$ is retrieved after Fourier transform. The mathematical expression of (A.15) can be solved analytically only in some cases, for example when pure white frequency noise is dominant. Indeed in such case the frequency noise PSD is represented by a constant value independent from Fourier frequencies f:

$$S_\nu(f) = h_0 \tag{A.16}$$

and its electric field PSD is:

$$S_E(\nu) = E_0^2 \frac{h_0}{(\nu - \nu_0)^2 + \frac{\pi^2 h_0^2}{4}} \tag{A.17}$$

which is a Lorentzian function. When other noise mechanisms than white frequency noise are present, the line-shape of a laser becomes the convolution of a Lorentzian and a Gaussian contributions, the first coming from the aforementioned white frequency noise, the second mainly due to spontaneous emission and flicker noise. In those cases a solution of Eq.(A.15) is not straightforward, and numerical integrations are necessary to retrieve the line-shape of the laser, taking care of the physics behind the boundaries to set in the integral calculation.

A.1 Linewidth of a Laser Source

The purpose of the following analysis is to explain some methods to evaluate the linewidth of lasers. The linewidth is an useful parameter which allows to compare the spectral characteristics of different sources. Noise processes cause the laser to be far from a monochromatic source, i.e. characterised by a delta-function peak centred at ν_0 in the frequency domain, and the linewidth is the parameter that express how far is the considered laser source from an ideal one.

Since the 1950s with the famous works of Schawlow and Townes [170], the linewidth of laser sources was under study. Starting from their pioneering analysis, M. Lax derived the quantum limit expression for the laser linewidth when spontaneous emission events are the only source of broadening [171]:

$$HWHM = \frac{\pi \hbar \nu_0 (\Delta\nu_c)^2}{P}(1 + \alpha^2) \tag{A.18}$$

The term $\hbar\nu_0$ is the photon energy, $\Delta\nu_c$ is the half-width at half maximum of the laser cavity resonance, P is the output power of the laser and $(1+\alpha^2)$ is a broadening factor due to amplitude-to-phase noise coupling. The result reported above is the ultimate intrinsic limit of a laser linewidth.

Typical laser sources are affected by several noise processes and a simple equation for the evaluation of their linewidth is not available. This is why several experimental approaches have been developed to measure the laser linewidth. One of of the most used rely on the beat-note measurement generated heterodyning the laser under study with a reference one in the same spectral region characterised by better properties of both stability and coherence. By superimposing the two fields onto a photodetector, the measured beat-note signal is proportional to the square of the sum of the electric fields:

$$(E_1(t) + E_2(t))^2 \sim E_1^2 + E_2^2 + E_1 E_2 \cos((\omega_2 - \omega_1)t + (\varphi_2 - \varphi_1)) \quad \text{(A.19)}$$

where the high frequency terms are omitted because far away from the bandwidth limit of the detector. For lasers that have similar optical frequencies, the beat-note signal lies in the radio-frequency (RF) domain where electrical spectrum analysers can be used for the characterization. The beat-note, in fact, represents the convolution of the linewidth of the two lasers: when the linewidth of the reference laser is well known or supposed to be negligible (for instance where the reference laser has an Hz-level linewidth), it is possible to retrieve the linewidth of the source under test.

A second widely employed employed method to measure the frequency noise directly in the optical domain is related to the use of an optical frequency discriminator which allows to convert laser frequency fluctuations to amplitude modulation. A typical frequency discriminator is constituted by a shoulder of a Fabry-Perot resonance or by a side of an atomic or molecular absorption. The frequency noise characterization of a laser with a cavity is obtained by tuning it into resonance in order to have a transmitted power which is half of the maximum power. In this case the laser is probing the resonance in correspondence of the maximum slope of the resonance where the frequency-to-amplitude conversion is linear. If the cavity or the laser drifts do not allow to have the described coupling condition for the time needed for the measurement, the laser can be slowly locked to the side of cavity to be transmitted without affecting too much the original noise characteristics. The PSD of the transmitted power is then measured through a photodetector connected to an ESA. The obtained spectrum provides the power for the different Fourier frequencies, with units V^2/Hz. The slope of the resonance is the frequency discriminator D_ν in V/Hz, which is the conversion factor between amplitude and frequency fluctuation. The frequency noise PSD of the input laser is then obtained from S_V according to:

$$S_\nu(f) = \frac{S_V}{D_\nu^2} \quad \text{(A.20)}$$

A rigorous analysis envisages the cleaning of the transmitted output PSD from the background noise, measurable by covering the detector, and the laser amplitude noise contribution. For the latter an independent measurement has to be performed to separate it from the frequency noise contribution. Also $S_V(f)$ has to be corrected from the filtering action of the resonator for Fourier frequencies above its characteristic frequency cut-off, which corresponds to a value equal to the half-width at half maximum of the resonance.

A very powerful technique to retrieve an approximate value of the linewidth uses a geometrical approach starting from the frequency noise PSD, as reported in Ref. [149]. Introducing the β-separation line described as:

$$\beta(f) = \frac{8 \ln 2}{\pi^2} f \tag{A.21}$$

it is possible to demonstrate that the section of $S_\nu(f)$ lying below the β line contributes mainly on the Lorentzian wings of the line-shape, whereas the sections above it affect the central peak determining its FWHM. Considering the area A of the section above the βline, the laser FWHM is evaluated as:

$$FWHM \approx \sqrt{8 \ln 2 A} \tag{A.22}$$

In Ref. [149] some examples are shown for the evaluation of the laser linewidth of sources affected by different noises, results that are in very good agreement with the values obtained from different independent procedures.

A.2 Allan-Werle Deviation

The noise characterisation of a laser source described in the previous section is a very useful tool to study the noise in the spectral domain. That description is usually supported by an Allan-Werle deviation analysis, which provides information about the average frequency stability of the laser source over different time scales.

In 1966 Allan suggested a two-sample variance, to characterise the frequency stability of oscillators acting as atomic frequency standards [172], which avoided the problem of non-convergence present for the standard variance in the case of noise processes different from the white noise. Later in 1993, Werle and co-workers applied the Allan deviation concept to measure the stability of laser sources employed as molecular spectrometers [173], so in this thesis we refer to such measurement as an Allan-Werle deviation analysis. The importance of the Allan-Werle deviation is to reveal possible drifts that cannot be clearly seen in short time-scale measurements. Focusing on a series of adjacent frequency measurement, obtained by averaging over a time interval τ, it is possible to evaluate the frequency deviations.

The Allan-Werle deviation relative to the variable $y(t)$ is defined as:

$$\sigma_A(\tau) = \left\langle \frac{1}{2} [\overline{y}(t+\tau) - \overline{y}(t)]^2 \right\rangle \tag{A.23}$$

where $\langle\rangle$ indicates an infinite time average and $\overline{y}$ represents a time average of $y(t)$ as a function of the time interval τ. A graph of the rms difference as a function of the integration time τ reveals the fluctuations of the source over different time-scales.

Experimentally, when considering $y(t)$ as the frequency of the frequency oscillator under test, an estimation of the Allan-Werle deviation can be obtained from a finite set of N-measurements $\overline{y_i}$ measured by a frequency counter for instance:

$$\sigma_A(\tau) = \left[\frac{1}{2(N-1)} \sum_{i=1}^{N-1} (\overline{y_{i+1}} - \overline{y_i})^2\right] \tag{A.24}$$

The previous evaluation is strongly affected by dead-times of the frequency counter or of the measuring device, that in general may bias the results. Figure A.1 shows typical noise processes in the so-called Allan-Werle deviation graph. White and flicker phase noise follow the τ^{-1} power law, while white frequency noise $\tau^{-1/2}$, flicker frequency noise τ^0, random walk frequency $\tau^{1/2}$ and linear frequency drifts τ^1.

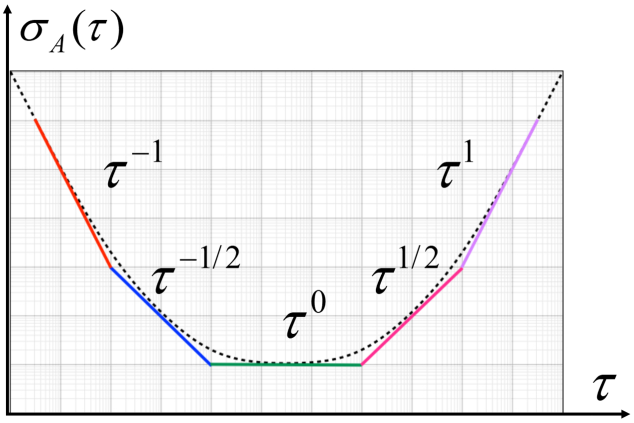

Figure A.1: Allan-Werle deviation behaviours, as a function of the integration time, for different phase and frequency noise processes and frequency drifts.

The Allan-Werle deviation is useful for the evaluation of the Limit Of Detection (LOD) of spectroscopic systems. The relation is described in details in Chapter 3 for the two spectroscopic configurations used in this thesis, namely Cavity Enhanced Absorption Spectroscopy (CEAS) and Cavity Ring Down Spectroscopy (CRDS).

Appendix B

Pound-Drever-Hall Locking

This appendix is focused on the description of the Pound-Drever-Hall locking of a laser to an optical resonator. Frequency and phase locking techniques are particular useful to obtain a more stable and purer spectral source, which is beneficial for several applications in optical spectroscopy, for instance to interrogate narrow molecular transitions such as Lamb dips. Among the techniques for laser stabilization, the Pound-Drever-Hall (PDH) locking is a highly versatile approach with very good performances in terms of robustness and locking bandwidth.

The first implementation was based on a microwave-oscillator stabilization scheme by Pound [174] and was adapted in the near-IR and optical domain by Drever, Hall and co-workers [175]. For a complete and detailed description of this locking technique the reader can refers to [117]. The concept of Pound-Drever-Hall technique is to measure the frequency of the laser under test by means of an optical resonator. In the following the focus is to explain the concepts leading to the so-called PDH error signal and the frequency discriminator.

Before the development of the PDH locking scheme, the general procedure to reduce the frequency noise of a laser by means of an optical resonator was to maintain the laser at the side of one of the cavity resonances, where some of the light is still transmitted. If the laser frequency suffers some fluctuations, the transmitted intensity changes proportionally. By measuring the transmitted intensity changes and feeding back them to the laser is possible to lock its frequency in correspondence to the side of the resonance. This procedure is simple and easy to apply, but it is limited by the fact that is not possible to distinguish between laser frequency noise and amplitude noise, which causes unwanted corrections. A better method is to measure the reflected intensity and hold it at zero, but unfortunately the intensity of the reflected beam is symmetric about resonance and is not possible to discriminate in which direction the laser frequency has to be corrected.

However, it is well known that the derivative of a symmetric function is anti-symmetric, so the first derivative of the reflected beam can be used to create an error signal to lock the laser to the cavity. Indeed when the laser frequency is above that of the centre of the resonance, the derivative of the reflected beam is positive, the opposite happens when the laser frequency is below resonance, whereas on resonance the reflected intensity is at zero. If a sinusoidal modulation is applied to the laser frequency or phase, the reflected intensity varies sinusoidally in-phase with the sine when above resonance and 180° out-of-phase below it. By comparing the variation in the reflected intensity with the modulation applied it is possible to tell on which side of the resonance the laser is.

In practice, it is easier to modulate the phase of the input beam instead of its frequency, for instance using an electro-optical phase modulator. The modulated electric field can be expressed using Bessel functions:

$$\begin{aligned} E_{inc} &\approx E_0[J_0(\beta) + 2iJ_1(\beta)\sin(\Omega t)]e^{i\omega t} \\ &= E_0[J_0(\beta)e^{i\omega t} + J_1(\beta)e^{i(\omega+\Omega)t} - J_1(\beta)e^{i(\omega-\Omega)t}] \end{aligned} \tag{B.1}$$

where, in the last expression, three terms can be separated: a carrier with frequency ω and two sidebands with frequency $\omega \pm \Omega$. Ω is the phase modulation frequency and β is the phase modulation depth.

Considering the total power of the incident beam as $P_0 = |E_0|^2$, the power in the carrier is $P_c = J_0^2(\beta)P_0$ and the power in each first order sideband is $P_s = J_1^2(\beta)P_0$. For small modulation depth, which means $\beta < 1$, almost all power is in the carrier and the first order sidebands, so that $P_c + 2P_s \approx P_0$. The electric field of the total reflected beam can be written as:

$$\begin{aligned} E_{ref} = E_0[&F(\omega)J_0(\beta)e^{i\omega t} \\ &+ F(\omega+\Omega)J_1(\beta)e^{i(\omega+\Omega)t} - F(\omega-\Omega)J_1(\beta)e^{i(\omega-\Omega)t}] \end{aligned} \tag{B.2}$$

where $F(\omega)$ is the reflection coefficient of a symmetric cavity with no losses defined as the ratio E_{ref}/E_{inc}:

$$F(\omega) = \frac{r\left[\exp\left(i\dfrac{\omega}{\Delta\nu_{fsr}}\right) - 1\right]}{1 - r^2\exp\left(i\dfrac{\omega}{\Delta\nu_{FSR}}\right)} \tag{B.3}$$

being r the amplitude reflection of each mirror and $\Delta\nu_{FSR}$ the free spectral range of the cavity.

After some algebra the reflected power is:

$$\begin{aligned} P_{ref} = |E_{ref}|^2 = P_c|F(\omega)|^2 + P_s\{|F(\omega+\Omega)|^2 + |F(\omega-\Omega)|^2\}+ \\ + 2\sqrt{P_cP_s}\{Re[F(\omega)F^*(\omega+\Omega) - F^*(\omega)F(\omega-\Omega)]\cos\Omega t+ \\ + Im[F(\omega)F^*(\omega+\Omega) - F^*(\omega)F(\omega-\Omega)]\sin\Omega t\} + (2\Omega terms) \end{aligned} \tag{B.4}$$

The terms sampling the phase of the reflected beam are:

$$F(\omega)F^*(\omega+\Omega) - F^*(\omega)F(\omega-\Omega) \tag{B.5}$$

When the carrier is near resonance and the modulation frequency Ω is high enough that the sidebands are not, Eq.(B.5) is purely imaginary and in Eq.(B.4) the cosine term cancels out [117, 175]. The so-called error signal is extracted by acquiring the modulated reflected signal on a photodetector, mixing it with the frequency modulation signal and filtering it with a low pass filter:

$$\epsilon = -2\sqrt{P_c P_s} Im\left\{F(\omega)F^*(\omega+\Omega) - F^*(\omega)F(\omega-\Omega)\right\} \tag{B.6}$$

A plot depicting the error signal is reported in Figure B.1, at resonance it

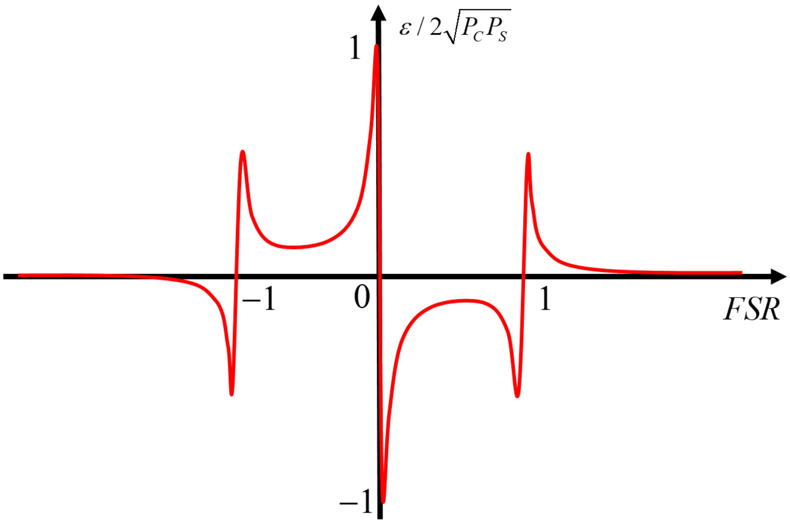

Figure B.1: Simulated Pound-Drever-Hall error signal for the case of fast modulation near the resonance of a symmetric cavity.

is antisymmetric and has a zero crossing point suitable as the locking point for the control system.

In the particular case where the optical resonator has a high finesse, the reflection coefficient close to resonance can be expressed as a function of the frequency deviation $\delta\omega$ and the cavity's linewidth $\delta\nu$:

$$F \approx \frac{i}{\pi}\frac{\delta\omega}{\delta\nu} \tag{B.7}$$

As long as $\delta\omega \ll \delta\nu$, the error signal can be linearised:

$$\epsilon \approx -\frac{4}{\pi}\sqrt{P_c P_s}\frac{\delta\omega}{\delta\nu} = -8\sqrt{P_c P_s}\frac{\delta f}{\delta\nu} \tag{B.8}$$

In the last equation the conversion between angular and regular frequency $f = \omega/2\pi$ has been used. The error signal can be rewritten as $\epsilon = D\delta f$, where D is the frequency discriminant defined as:

$$D \equiv -\frac{8\sqrt{P_c P_s}}{\delta\nu} \tag{B.9}$$

The more the frequency discriminant is steep, the more frequency fluctuations can be detected and corrected. This is the reason why high finesse cavities are widely used to reduce the frequency noise of a laser by PDH-locking.

Since the PDH approach is based on the laser stabilization on a cavity resonance where the reflected carrier vanishes, the locking is insensitive to contributions coming from: the laser intensity noise, the photodetector response, the relative phase of the two signals going into the mixer and their modulation frequency and depth. The technique is sensitive to fluctuations in the sidebands power, but their noise can be reduced increasing the modulation frequency (since most noise processes have less impact as frequency increases). However the shot noise of the reflected sidebands is a limiting factor which cannot be reduced increasing the modulation frequency, and the best frequency noise reduction through PDH locking stops at the level imposed by this limit.

Appendix C

Single Sideband Modulator

This appendix regards the properties of a Single Sideband Modulator (SSM). A detailed theoretical analysis is given in the supplementary materials Ref. [159] for instance.

A SSM is basically a Mach-Zehnder Interferometer (MZI) realised with lithium-niobate ($LiNbO_2$) technology where the two branches are two Mach-Zehnder Modulators (MZM). This configuration is typically called dual-parallel MZM.

By feeding an SSM with a laser source it generates a single broadly-tunable sideband suppressing the input optical carrier and the other sideband, as sketched in Figure C.1.

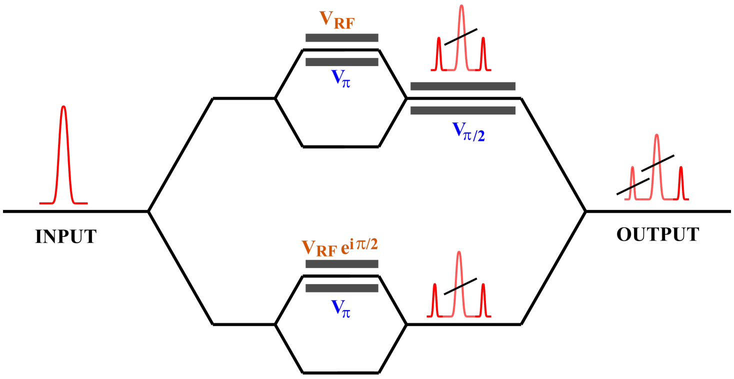

Figure C.1: SSM configuration scheme. A quadrature RF signal is applied at the two branches together with appropriate bias voltages to suppress the optical carrier. The suppression of one sideband with respect to the other is achieved through the application of a $\pi/2$ bias voltage at the outer interferometer.

A high-bandwidth actuator is fundamental in application such as laser-frequency control loops, where there is the need to imprint very fast frequency corrections. Typically in a frequency control loop, a laser, affected by frequency noise, is stabilized against a primary reference source such as a low-noise narrow laser or an optical resonator. If the frequency difference between the reference and the laser under test is measured, it is possible to use that difference as an error signal to drive the frequency actuator and correct for the relative frequency fluctuations between the two lasers. Focusing only on actuators external to the laser source under correction, the most common are acousto-optic frequency shifters, in which the error signal drives the acoustic wave inside the medium, so that in the first-diffracted beam the frequency fluctuations are corrected. With respect to AOMs, a SSM is inherently faster because it does not rely on the propagation speed of the acuostic-wave, thus it enables a sub-ns response time. Also it provides a working range of tens of GHz, much wider than those of AOMs.

When a continuous wave (CW) laser with electric field $E(t) = E_0 \cos(\omega_0 t + \varphi(t))$ is provided at the input of the SSM, firstly it is equally separated in the two branches where two static bias voltages for a π phase shift are applied. The two MZMs are driven by the RF error signal, which is sent through a 90° hybrid coupler, thus the two equally divided branches of the input beam are phase-modulated by the Pockels effect following the relations:

$$\varphi_1(t) = G\cos(\omega_m t + \phi_m) \tag{C.1}$$

$$\varphi_2(t) = G\cos(\omega_m t + \phi_m + \pi/2) \tag{C.2}$$

where G is the modulation depth (properly amplified after a gain stage), ω_m and ϕ_m are the frequency and phase of the RF modulating signal.

Let us now consider the upper MZM of Figure C.1, where at its input is injected $E(t)/2$, to retrieve the expression of the field at its output. The description for the lower MZM is similar to the following. At the two branches there is a relative static phase of π that may be written as $\pi = \pi/2 - (-\pi/2)$ and inserted in the expression of the two fields summing at the output of the modulator:

$$E_1(t) = \frac{E_0}{2}\left\{\cos\left[\omega_0 t + \varphi(t) + \frac{\pi}{2} + \varphi_1(t)\right] + \cos\left[\omega_0 t + \varphi(t) - \frac{\pi}{2} - \varphi_1(t)\right]\right\} \tag{C.3}$$

where it has been considered also the RF modulating signal. The development of the two cosines simplifies the equation, that may be rewritten as:

$$E_1(t) = -E_0 \cos[\omega_0 t + \varphi(t)]\sin[\varphi_1(t)] \tag{C.4}$$

The term $\sin[\varphi_1(t)] = \sin[G\cos(\omega_m t + \phi_m)]$ may be expressed through the well-known Bessel functions:

$$\sin[G\cos(\omega_m t + \phi_m)] = 2\sum_{k=0}^{+\infty}(-1)^k J_{2k+1}(G)\cos[(2k+1)(\omega_m t + \phi_m)] \tag{C.5}$$

For small modulation depths $G << 1$, the above equation is goodly approximated by the first-order Bessel function, and Eq.(C.3) becomes:

$$E_1(t) = -J_1(G)E_0 \{[\cos(\omega_0 t + \varphi(t)) - (\omega_m t + \phi_m)] + \\ + \cos[\cos(\omega_0 t + \varphi(t)) - (\omega_m t + \phi_m)]\} \quad \text{(C.6)}$$

Analogously a same description is possible for the lower MZM of Figure C.1 considering the quadrature shift of the RF signal:

$$E_2(t) = -J_1(G)E_0 \{[\sin(\omega_0 t + \varphi(t)) - (\omega_m t + \phi_m)] + \\ + \sin[\cos(\omega_0 t + \varphi(t)) - (\omega_m t + \phi_m)]\} \quad \text{(C.7)}$$

At both branches the optical carrier is suppressed.

The application of a $\pm\pi/2$ static bias voltage to the outer MZI, where the sign - or + depends on what sideband is selected, implies that in the sum of the fields E_1 and E_2 also one sideband is suppressed. For the sake of simplicity let us consider the (-) single sideband, which means the selection of a $-\pi/2 = -[\pi/4 - (-\pi/4)]$ static phase shift. Writing the sum of the two fields $E_1 + E_2$ and applying the trigonometric addition theorem, it is possible to obtain the following equation for the SSM output field:

$$E_{OUT-}(t) = 2J_1(G)E_0 \cos\left[\omega_0 t + \varphi(t) - \omega_m t - \phi_m + \frac{3\pi}{4}\right] \quad \text{(C.8)}$$

Eq.(C.8) shows that the (-) single sideband oscillates at a frequency $\omega_0 - \omega_m$.

If ω_m contains the information about the frequency fluctuations of a noisy laser with respect to a stable reference, the SSM output sideband is a purified version of the input laser phase-cloning the reference. Conversely, the (+) sideband contains double of the frequency fluctuations.

Ideally, the output of the modulator is only the single sideband, in reality some spurious signals and an imperfectly suppressed carrier can still be present. The contrast of the single sideband with respect to the other suppressed tones is typically greater than 30 dB.

One of the strengths of SSMs is the possibility to tune the single sideband for more than 10 GHz, leaving the input optical carrier unperturbed. Conversely one weakness is the difficulty to provide a high-RF power at the two branches, at the level of +26 dBm typically, with a precisely fixed $\pi/2$ phase-shift over a such large frequency range, thus reducing the single sideband contrast if the bias voltage of the outer MZI is not actively controlled.

Such a versatile modulator may be used as a frequency actuator in a Pound-Drever-Hall locking scheme as reported in Chapter 4. Indeed thanks to the high-bandwidth of the device the limiting factors in the correction bandwidth are due to delays introduced in the control loop. Minimizing those delays lead to control bandwidths at the MHz level that are beneficial to improve the quality of the frequency locking.

Bibliography

[1] Richard Engeln, Giel Berden, Rudy Peeters, and Gerard Meijer. Cavity enhanced absorption and cavity enhanced magnetic rotation spectroscopy. *Review of scientific instruments*, 69(11):3763–3769, 1998. `doi:10.1063/1.1149176`.

[2] D Romanini, AA Kachanov, N Sadeghi, and F Stoeckel. Cw cavity ring down spectroscopy. *Chemical Physics Letters*, 264(3-4):316–322, 1997. `doi:10.1016/s0009-2614(96)01351-6`.

[3] Gareth D Dickenson, Ming Li Niu, Edcel J Salumbides, Jacek Komasa, Kjeld SE Eikema, Krzysztof Pachucki, and Wim Ubachs. Fundamental vibration of molecular hydrogen. *Physical review letters*, 110(19):193601, 2013. `doi:10.1103/physrevlett.110.193601`.

[4] CS Edwards, GP Barwood, HS Margolis, P Gill, and WRC Rowley. High-precision frequency measurements of the ν 1+ ν 3 combination band of 12 c 2 h 2 in the 1.5 μm region. *Journal of Molecular Spectroscopy*, 234(1):143–148, 2005. `doi:10.1016/j.jms.2005.08.014`.

[5] Alan A Madej, A John Alcock, Andrzej Czajkowski, John E Bernard, and Sergei Chepurov. Accurate absolute reference frequencies from 1511 to 1545 nm of the ν1+ ν3 band of 12 c2h2 determined with laser frequency comb interval measurements. *JOSA B*, 23(10):2200–2208, 2006. `doi:10.1364/josab.23.002200`.

[6] Sylvestre Twagirayezu, Matthew J Cich, Trevor J Sears, Christopher P McRaven, and Gregory E Hall. Frequency-comb referenced spectroscopy of v 4-and v 5-excited hot bands in the 1.5 μm spectrum of c 2 h 2. *Journal of Molecular Spectroscopy*, 316:64–71, 2015. `doi:10.1016/j.jms.2015.06.010`.

[7] Eugenio Fasci, Maria Domenica De Vizia, Andrea Merlone, Luigi Moretti, Antonio Castrillo, and Livio Gianfrani. The boltzmann constant from the h2 18o vibration–rotation spectrum: complementary tests and revised uncertainty budget. *Metrologia*, 52(5):S233, 2015. `doi:10.1088/0026-1394/52/5/s233`.

[8] Johann Heinrich Lambert. *Photometria sive de mensura et gradibus luminis, colorum et umbrae.* Klett, 1760.

[9] August Beer. Bestimmung der absorption des rothen lichts in farbigen flussigkeiten. *Ann. Physik*, 162:78–88, 1852. `doi:10.1002/andp.18521620505`.

[10] Robert Eisberg and Robert Resnick. *Quantum physics.* John Wiley New York, 1974.

[11] Erwin Schrödinger. An undulatory theory of the mechanics of atoms and molecules. *Physical Review*, 28(6):1049, 1926. `doi:10.1103/physrev.28.1049`.

[12] Vladilen S Letokhov and Veniamin Pavlovich Chebotayev. *Nonlinear laser spectroscopy*, volume 4. Springer, 1977. `doi:10.1007/978-3-540-37541-8`.

[13] Ludwig Boltzmann. *Lectures on gas theory.* Courier Corporation, 2012. `doi:10.1063/1.3051862`.

[14] A Goldman, RR Gamache, A Perrin, J-M Flaud, CP Rinsland, and LS Rothman. Hitran partition functions and weighted transition-moments squared. *Journal of Quantitative Spectroscopy and Radiative Transfer*, 66(5):455–486, 2000. `doi:10.1016/s0022-4073(99)00176-4`.

[15] Christian Hill, Iouli E Gordon, Roman V Kochanov, Lorenzo Barrett, Jonas S Wilzewski, and Laurence S Rothman. Hitranonline: An online interface and the flexible representation of spectroscopic data in the hitran database. *Journal of Quantitative Spectroscopy and Radiative Transfer*, 177:4–14, 2016. `doi:10.1016/j.jqsrt.2015.12.012`.

[16] A Ben-Reuven, H Friedmann, and JH Jaffe. Theory of pressure-induced shifts of infrared lines. *The Journal of Chemical Physics*, 38(12):3021–3028, 1963. `doi:10.21236/ad0400319`.

[17] Laurence S Rothman, Iouli E Gordon, Yury Babikov, Alain Barbe, D Chris Benner, Peter F Bernath, Manfred Birk, Luca Bizzocchi, Vincent Boudon, Linda R Brown, et al. The hitran2012 molecular spectroscopic database. *Journal of Quantitative Spectroscopy and Radiative Transfer*, 130:4–50, 2013. `doi:10.1016/j.jqsrt.2013.07.002`.

[18] Ch J Bordé, JL Hall, CV Kunasz, and DG Hummer. Saturated absorption line shape: Calculation of the transit-time broadening by a perturbation approach. *Physical Review A*, 14(1):236, 1976. `doi:10.1103/physreva.14.236`.

[19] Roman Ciuryło. Shapes of pressure-and doppler-broadened spectral lines in the core and near wings. *Physical Review A*, 58(2):1029, 1998. doi:10.1103/physreva.58.1029.

[20] Jonathan Tennyson, Peter F Bernath, Alain Campargue, Attila G Császár, Ludovic Daumont, Robert R Gamache, Joseph T Hodges, Daniel Lisak, Olga V Naumenko, Laurence S Rothman, et al. Recommended isolated-line profile for representing high-resolution spectroscopic transitions (iupac technical report). *Pure and Applied Chemistry*, 86(12):1931–1943, 2014. doi:10.1515/pac-2014-0208.

[21] RH Dicke. The effect of collisions upon the doppler width of spectral lines. *Physical Review*, 89(2):472, 1953. doi:10.1103/physrev.89.472.

[22] Sergei G Rautian and Igor I Sobel'man. The effect of collisions on the doppler broadening of spectral lines. *Soviet Physics Uspekhi*, 9(5):701, 1967. doi:10.1070/pu1967v009n05abeh003212.

[23] Mark Nelkin and Ajoy Ghatak. Simple binary collision model for van hove's g s (r, t). *Physical Review*, 135(1A):A4, 1964. doi:10.1103/PhysRev.135.A4.

[24] Louis Galatry. Simultaneous effect of doppler and foreign gas broadening on spectral lines. *Physical Review*, 122(4):1218, 1961. doi:10.1103/physrev.122.1218.

[25] Paul R Berman. Speed-dependent collisional width and shift parameters in spectral profiles. *Journal of Quantitative Spectroscopy and Radiative Transfer*, 12(9):1331–1342, 1972. doi:10.1016/0022-4073(72)90189-6.

[26] NH Ngo, D Lisak, H Tran, and J-M Hartmann. Erratum to" an isolated line-shape model to go beyond the voigt profile in spectroscopic databases and radiative transfer codes"[j. quant. spectrosc. radiat. transf. 129 (2013) 89-100]. *Journal of Quantitative Spectroscopy and Radiative Transfer*, 134:105–105, 2014. doi:10.1016/j.jqsrt.2013.10.016.

[27] MD De Vizia, A Castrillo, E Fasci, P Amodio, L Moretti, and L Gianfrani. Experimental test of the quadratic approximation in the partially correlated speed-dependent hard-collision profile. *Physical Review A*, 90(2):022503, 2014. doi:10.1103/physreva.90.022503.

[28] LS Vasilenko, VP Chebotaev, and AV Shishaev. Line shape of two-photon absorption in a standing-wave field in a gas. *ZhETF Pisma Redaktsiiu*, 12:161, 1970.

[29] VS Letokhov. Narrowing of the doppler width in a standing wave. *ZhETF Pisma Redaktsiiu*, 7:348, 1968.

[30] G Gagliardi, G Rusciano, and L Gianfrani. Sub-doppler spectroscopy of h 2 18 o at 1.4 μm. *Applied Physics B: Lasers and Optics*, 70(6):883–888, 2000. doi:10.1007/pl00021149.

[31] WR Bennett Jr. Hole burning effects in a he-ne optical maser. *Physical Review*, 126(2):580, 1962. doi:10.1103/physrev.126.580.

[32] Willis Lamb. Theory of an optical maser. *Physical Review*, 134(6A):A1429, 1964. doi:10.1103/physrev.134.a1429.

[33] Max Born and Robert Oppenheimer. Zur quantentheorie der molekeln. *Annalen der Physik*, 389(20):457–484, 1927. doi:10.1002/andp.19273892002.

[34] Gerhard Herzberg. *The spectra and structures of simple free radicals: an introduction to molecular spectroscopy*. Courier Corporation, 1971.

[35] Jeffrey I Steinfeld. *Molecules and radiation: An introduction to modern molecular spectroscopy*. Courier Corporation, 2012.

[36] K Narahari Rao. *Molecular spectroscopy: modern research*. Elsevier, 2012.

[37] Philip M Morse. Diatomic molecules according to the wave mechanics. ii. vibrational levels. *Physical Review*, 34(1):57, 1929. doi:10.1103/physrev.34.57.

[38] J Michael Hollas. *Modern spectroscopy*. John Wiley & Sons, 2004.

[39] Ursula Keller. Recent developments in compact ultrafast lasers. *Nature*, 424(6950):831–838, aug 2003. doi:10.1038/nature01938.

[40] Th. Udem, J. Reichert, R. Holzwarth, and T. W. Hänsch. Accurate measurement of large optical frequency differences with a mode-locked laser. *Opt. Lett.*, 24(13):881–883, Jul 1999. doi:10.1364/OL.24.000881.

[41] Darren D Hudson, Kevin W Holman, R Jason Jones, Steven T Cundiff, Jun Ye, and David J Jones. Mode-locked fiber laser frequency-controlled with an intracavity electro-optic modulator. *Optics letters*, 30(21):2948–2950, 2005. doi:10.1364/ol.30.002948.

[42] Marco Bellini and Theodor W. Hänsch. Phase-locked white-light continuum pulses: toward a universal optical frequency-comb synthesizer. *Opt. Lett.*, 25(14):1049–1051, Jul 2000. doi:10.1364/OL.25.001049.

[43] Th Udem, Ronald Holzwarth, and Theodor W Hänsch. Optical frequency metrology. *Nature*, 416(6877):233–237, 2002. `doi:10.1038/416233a`.

[44] David J. Jones, Scott A. Diddams, Jinendra K. Ranka, Andrew Stentz, Robert S. Windeler, John L. Hall, and Steven T. Cundiff. Carrier-envelope phase control of femtosecond mode-locked lasers and direct optical frequency synthesis. *Science*, 288(5466):635–639, 2000. `arXiv:http://science.sciencemag.org/content/288/5466/635.full.pdf`, `doi:10.1126/science.288.5466.635`.

[45] Harald R Telle, G Steinmeyer, AE Dunlop, J Stenger, DH Sutter, and U Keller. Carrier-envelope offset phase control: A novel concept for absolute optical frequency measurement and ultrashort pulse generation. *Applied Physics B: Lasers and Optics*, 69(4):327–332, 1999. `doi:10.1007/s003400050813`.

[46] Scott A Diddams, David J Jones, Jun Ye, Steven T Cundiff, John L Hall, Jinendra K Ranka, Robert S Windeler, Ronald Holzwarth, Thomas Udem, and TW Hänsch. Direct link between microwave and optical frequencies with a 300 thz femtosecond laser comb. *Physical Review Letters*, 84(22):5102, 2000. `doi:10.1103/PhysRevLett.84.5102`.

[47] N Haverkamp, H Hundertmark, C Fallnich, and HR Telle. Frequency stabilization of mode-locked erbium fiber lasers using pump power control. *Applied Physics B: Lasers and Optics*, 78(3):321–324, 2004. `doi:10.1007/s00340-003-1397-y`.

[48] Nathan R Newbury and William C Swann. Low-noise fiber-laser frequency combs. *JOSA B*, 24(8):1756–1770, 2007. `doi:10.1364/JOSAB.24.001756`.

[49] Erik Benkler, Harald R Telle, Armin Zach, and Florian Tauser. Circumvention of noise contributions in fiber laser based frequency combs. *Optics express*, 13(15):5662–5668, 2005. `doi:10.1364/OPEX.13.005662`.

[50] John J McFerran, William C Swann, BR Washburn, and NR Newbury. Suppression of pump-induced frequency noise in fiber-laser frequency combs leading to sub-radian f ceo phase excursions. *Applied Physics B: Lasers and Optics*, 86(2):219–227, 2007. `doi:10.1007/s00340-006-2426-4`.

[51] William C Swann, John J McFerran, I Coddington, Nathan R Newbury, Ingmar Hartl, Martin E Fermann, Paul S Westbrook, Jeffrey W Nicholson, KS Feder, Carston Langrock, et al. Fiber-laser frequency

combs with subhertz relative linewidths. *Optics letters*, 31(20):3046–3048, 2006. `doi:10.1364/OL.31.003046`.

[52] Davide Gatti, Tommaso Sala, Marco Marangoni, Gianluca Galzerano, and Livio Gianfrani. Precision molecular spectroscopy with frequency combs. *Encyclopedia of Analytical Chemistry*, 2012. `doi:10.1002/9780470027318.a9249`.

[53] Scott A Diddams. The evolving optical frequency comb [invited]. *JOSA B*, 27(11):B51–B62, 2010. `doi:10.1364/JOSAB.27.000B51`.

[54] Kyoungsik Kim, Brian R Washburn, G Wilpers, Christopher W Oates, L Hollberg, Nathan R Newbury, Scott A Diddams, Jeffrey W Nicholson, and MF Yan. Stabilized frequency comb with a self-referenced femtosecond cr: forsterite laser. *Optics letters*, 30(8):932–934, 2005. `doi:10.1364/OL.30.000932`.

[55] MC Stumpf, S Pekarek, A EH Oehler, T Südmeyer, JM Dudley, and U Keller. Self-referencable frequency comb from a 170-fs, 1.5-μm solid-state laser oscillator. *Applied Physics B: Lasers and Optics*, 99(3):401–408, 2010. `doi:10.1007/s00340-009-3854-8`.

[56] Albrecht Bartels, Chris W Oates, Leo Hollberg, and Scott A Diddams. Stabilization of femtosecond laser frequency combs with subhertz residual linewidths. *Optics letters*, 29(10):1081–1083, 2004. `doi:10.1364/OL.29.001081`.

[57] Florian Tauser, Alfred Leitenstorfer, and Wolfgang Zinth. Amplified femtosecond pulses from an er: fiber system: Nonlinear pulse shortening and self-referencing detection of the carrier-envelope phase evolution. *Optics Express*, 11(6):594–600, 2003. `doi:10.1364/OE.11.000594`.

[58] Parama Pal, Wayne H Knox, Ingmar Hartl, and Martin E Fermann. Self referenced yb-fiber-laser frequency comb using a dispersion micromanaged tapered holey fiber. *Optics express*, 15(19):12161–12166, 2007. `doi:10.1364/OE.15.012161`.

[59] Jens Bethge, Jie Jiang, Christian Mohr, Martin Fermann, and Ingmar Hartl. Optically referenced tm-fiber-laser frequency comb. In *Advanced Solid-State Photonics*, pages AT5A–3. Optical Society of America, 2012. `doi:10.1364/ASSP.2012.AT5A.3`.

[60] Marc Fischer, Nikolai Kolachevsky, Marcus Zimmermann, Ronald Holzwarth, Th Udem, Theodor W Hänsch, M Abgrall, J Grünert, I Maksimovic, S Bize, et al. New limits on the drift of fundamental constants from laboratory measurements. *Physical Review Letters*, 92(23):230802, 2004. `doi:10.1103/PhysRevLett.92.230802`.

[61] CJ Campbell, AG Radnaev, and A Kuzmich. Wigner crystals of th 229 for optical excitation of the nuclear isomer. *Physical review letters*, 106(22):223001, 2011. `doi:10.1103/PhysRevLett.106.223001`.

[62] Florian Adler, Michael J Thorpe, Kevin C Cossel, and Jun Ye. Cavity-enhanced direct frequency comb spectroscopy: technology and applications. *Annual Review of Analytical Chemistry*, 3:175–205, 2010. `doi:10.1146/annurev-anchem-060908-155248`.

[63] Elisabeth Peters, Scott A Diddams, Peter Fendel, Sascha Reinhardt, TW Hänsch, and Th Udem. A deep-uv optical frequency comb at 205 nm. *Optics express*, 17(11):9183–9190, 2009. `doi:10.1364/OE.17.009183`.

[64] Arman Cingöz, Dylan C Yost, Thomas K Allison, Axel Ruehl, Martin E Fermann, Ingmar Hartl, and Jun Ye. Direct frequency comb spectroscopy in the extreme ultraviolet. *Nature*, 482(7383):68–71, 2012. `doi:10.1038/nature10711`.

[65] Axel Ruehl, Alessio Gambetta, Ingmar Hartl, Martin E Fermann, Kjeld SE Eikema, and Marco Marangoni. Widely-tunable mid-infrared frequency comb source based on difference frequency generation. *Optics letters*, 37(12):2232–2234, 2012. `doi:10.1364/OL.37.002232`.

[66] Feng Zhu, Holger Hundertmark, Alexandre A Kolomenskii, James Strohaber, Ronald Holzwarth, and Hans A Schuessler. High-power mid-infrared frequency comb source based on a femtosecond er: fiber oscillator. *Optics letters*, 38(13):2360–2362, 2013. `doi:10.1364/ol.38.002360`.

[67] Kevin F Lee, Christopher J Hensley, Peter G Schunemann, and ME Fermann. Midinfrared frequency comb by difference frequency of erbium and thulium fiber lasers in orientation-patterned gallium phosphide. *Optics express*, 25(15):17411–17416, 2017. `doi:10.1364/oe.25.017411`.

[68] Florian Adler, Kevin C Cossel, Michael J Thorpe, Ingmar Hartl, Martin E Fermann, and Jun Ye. Phase-stabilized, 1.5 w frequency comb at 2.8–4.8 μm. *Optics letters*, 34(9):1330–1332, 2009. `doi:10.1364/OL.34.001330`.

[69] Nick Leindecker, Alireza Marandi, Robert L Byer, Konstantin L Vodopyanov, Jie Jiang, Ingmar Hartl, Martin Fermann, and Peter G Schunemann. Octave-spanning ultrafast opo with 2.6-6.1 μm instantaneous bandwidth pumped by femtosecond tm-fiber laser. *Optics express*, 20(7):7046–7053, 2012. `doi:10.1364/oe.20.007046`.

[70] H Schnatz, B Lipphardt, J Helmcke, F Riehle, and G Zinner. First phase-coherent frequency measurement of visible radiation. *Physical Review Letters*, 76(1):18, 1996. `doi:10.1103/PhysRevLett.76.18`.

[71] M Niering, R Holzwarth, J Reichert, P Pokasov, Th Udem, M Weitz, TW Hänsch, P Lemonde, G Santarelli, M Abgrall, et al. Measurement of the hydrogen 1 s-2 s transition frequency by phase coherent comparison with a microwave cesium fountain clock. *Physical Review Letters*, 84(24):5496, 2000. `doi:10.1103/PhysRevLett.84.5496`.

[72] Christian G Parthey, Arthur Matveev, Janis Alnis, Birgitta Bernhardt, Axel Beyer, Ronald Holzwarth, Aliaksei Maistrou, Randolf Pohl, Katharina Predehl, Thomas Udem, et al. Improved measurement of the hydrogen 1 s–2 s transition frequency. *Physical review letters*, 107(20):203001, 2011. `doi:10.1103/PhysRevLett.107.203001`.

[73] E Peik, B Lipphardt, H Schnatz, T Schneider, Chr Tamm, and Savely G Karshenboim. Limit on the present temporal variation of the fine structure constant. *Physical Review Letters*, 93(17):170801, 2004. `doi:10.1103/PhysRevLett.93.170801`.

[74] RM Godun, PBR Nisbet-Jones, JM Jones, SA King, LAM Johnson, HS Margolis, K Szymaniec, SN Lea, K Bongs, and P Gill. Frequency ratio of two optical clock transitions in yb+ 171 and constraints on the time variation of fundamental constants. *Physical review letters*, 113(21):210801, 2014. `doi:10.1103/PhysRevLett.113.210801.`

[75] HS Margolis. Optical frequency standards and clocks. *Contemporary Physics*, 51(1):37–58, 2010. `doi:10.1080/00107510903257616`.

[76] TL Nicholson, MJ Martin, JR Williams, BJ Bloom, M Bishof, MD Swallows, SL Campbell, and J Ye. Comparison of two independent sr optical clocks with 1× 10- 17 stability at 10 3 s. *Physical review letters*, 109(23):230801, 2012. `doi:10.1103/PhysRevLett.109.230801`.

[77] SA Diddams, Th Udem, JC Bergquist, EA Curtis, RE Drullinger, L Hollberg, WM Itano, WD Lee, CW Oates, KR Vogel, et al. An optical clock based on a single trapped 199hg+ ion. *Science*, 293(5531):825–828, 2001. `doi:10.1126/science.1061171`.

[78] Thomas Kessler, Christian Hagemann, C Grebing, T Legero, Uwe Sterr, Fritz Riehle, MJ Martin, L Chen, and J Ye. A sub-40-mhz-linewidth laser based on a silicon single-crystal optical cavity. *Nature Photonics*, 6(10):687, 2012. `doi:10.1038/nphoton.2012.217`.

[79] Ross Hutson, Sara Campbell, Edward Marti, Akihisa Goban, Wei Zhang, John Robinson, Lindsay Sonderhouse, and Jun Ye. A fermi-

degenerate three-dimensional optical lattice clock. *Bulletin of the American Physical Society*, 2017. `doi:10.1126/science.aam5538`.

[80] Warren S Warren, Herschel Rabitz, and Mohammed Dahleh. Coherent control of quantum dynamics: the dream is alive. *Science*, 259(5101):1581–1589, 1993. `doi:10.1126/science.259.5101.1581`.

[81] Jun Ye. Absolute measurement of a long, arbitrary distance to less than an optical fringe. *Optics letters*, 29(10):1153–1155, 2004. `doi:10.1364/OL.29.001153`.

[82] Tilo Steinmetz, Tobias Wilken, Constanza Araujo-Hauck, Ronald Holzwarth, Theodor W Hänsch, Luca Pasquini, Antonio Manescau, Sandro D'odorico, Michael T Murphy, Thomas Kentischer, et al. Laser frequency combs for astronomical observations. *Science*, 321(5894):1335–1337, 2008. `doi:10.1126/science.1161030`.

[83] GG Paulus, F Grasbon, H Walther, P Villoresi, M Nisoli, S Stagira, E Priori, and S De Silvestri. Absolute-phase phenomena in photoionization with few-cycle laser pulses. *Nature*, 414(6860):182–184, 2001. `doi:10.1038/35102520`.

[84] John D Jost, John L Hall, and Jun Ye. Continuously tunable, precise, single frequency optical signal generator. *Optics express*, 10(12):515–520, 2002. `doi:10.1364/oe.10.000515`.

[85] TR Schibli, K Minoshima, F-L Hong, H Inaba, Y Bitou, A Onae, and H Matsumoto. Phase-locked widely tunable optical single-frequency generator based on a femtosecond comb. *Optics letters*, 30(17):2323–2325, 2005. `doi:10.1364/ol.30.002323`.

[86] Erik Benkler, Felix Rohde, and Harald R Telle. Endless frequency shifting of optical frequency comb lines. *Optics express*, 21(5):5793–5802, 2013. `doi:10.1364/oe.21.005793`.

[87] R Holzwarth, A Yu Nevsky, M Zimmermann, Th Udem, TW Hänsch, J Von Zanthier, H Walther, JC Knight, WJ Wadsworth, P St J Russell, et al. Absolute frequency measurement of iodine lines with a femtosecond optical synthesizer. *Applied Physics B*, 73(3):269–271, 2001. `doi:10.1007/s003400100633`.

[88] Feng-Lei Hong, Atsushi Onae, Jie Jiang, Ruixiang Guo, Hajime Inaba, Kaoru Minoshima, Thomas R Schibli, Hirokazu Matsumoto, and Ken'ichi Nakagawa. Absolute frequency measurement of an acetylene-stabilized laser at 1542 nm. *Optics letters*, 28(23):2324–2326, 2003. `doi:10.1364/ol.28.002324`.

[89] A Czajkowski, AJ Alcock, JE Bernard, AA Madej, M Corrigan, and S Chepurov. Studies of saturated absorption and measurements of optical frequency for lines in the ν 1+ ν 3 and ν 1+ 2ν 4 bands of ammonia at 1.5 μm. *Optics express*, 17(11):9258–9269, 2009. `doi:10.1364/OE.17.009258`.

[90] A Gambetta, E Fasci, A Castrillo, M Marangoni, G Galzerano, G Casa, P Laporta, and L Gianfrani. Frequency metrology in the near-infrared spectrum of h217o and h218o molecules: testing a new inversion method for retrieval of energy levels. *New Journal of Physics*, 12(10):103006, 2010. `doi:10.1088/1367-2630/12/10/103006`.

[91] Anne Amy-Klein, Hélene Vigué, and Christian Chardonnet. Absolute frequency measurement of 12 c 16 o 2 laser lines with a femtosecond laser comb and new determination of the 12 c 16 o 2 molecular constants and frequency grid. *Journal of Molecular Spectroscopy*, 228(1):206–212, 2004. `doi:10.1016/j.jms.2004.07.005`.

[92] Wei-Jo Ting, Chun-Hung Chang, Shih-En Chen, Hsuan-Chen Chen, Jow-Tsong Shy, Brian J Drouin, and Adam M Daly. Precision frequency measurement of n 2 o transitions near 4.5 μm and above 150 μm. *JOSA B*, 31(8):1954–1963, 2014. `doi:10.15278/isms.2014.tb06`.

[93] David A Long, G-W Truong, Joseph T Hodges, and CE Miller. Absolute 12 c 16 o 2 transition frequencies at the khz-level from 1.6 to 7.8 μm. *Journal of Quantitative Spectroscopy and Radiative Transfer*, 130:112–115, 2013. `doi:10.1016/j.jqsrt.2013.07.001`.

[94] D Mondelain, T Sala, S Kassi, D Romanini, M Marangoni, and A Campargue. Broadband and highly sensitive comb-assisted cavity ring down spectroscopy of co near 1.57 μm with sub-mhz frequency accuracy. *Journal of Quantitative Spectroscopy and Radiative Transfer*, 154:35–43, 2015. `doi:10.1016/j.jqsrt.2014.11.021`.

[95] Mikołaj Zaborowski, Piotr Wcisło, Franck Thibault, Szymon Wójtewicz, Agata Cygan, Grzegorz Kowzan, Piotr Masłowski, Daniel Lisak, and Roman Ciuryło. Crds measurements and ab initio calculations of collisional effects in pure d2. In *ASA-HITRAN 2016 Conference*, 2016.

[96] Livio Gianfrani. Linking the thermodynamic temperature to an optical frequency: recent advances in doppler broadening thermometry. *Phil. Trans. R. Soc. A*, 374(2064):20150047, 2016. `doi:10.1098/rsta.2015.0047`.

[97] D Gatti, A Gambetta, A Castrillo, G Galzerano, P Laporta, L Gianfrani, and M Marangoni. High-precision molecular interrogation by direct referencing of a quantum-cascade-laser to a near-infrared frequency comb. *Optics express*, 19(18):17520–17527, 2011. doi:10.1364/OE.19.017520.

[98] Markku Vainio, Mikko Merimaa, and Lauri Halonen. Frequency-comb-referenced molecular spectroscopy in the mid-infrared region. *Optics letters*, 36(21):4122–4124, 2011. doi:10.1364/ol.36.004122.

[99] Titus Gherman and Daniele Romanini. Mode–locked cavity–enhanced absorption spectroscopy. *Optics Express*, 10(19):1033–1042, 2002. doi:10.1364/oe.10.001033.

[100] Nicolas Bourbeau Hébert, Sarah K Scholten, Richard T White, Jérôme Genest, Andre N Luiten, and James D Anstie. A quantitative mode-resolved frequency comb spectrometer. *Optics express*, 23(11):13991–14001, 2015. doi:10.1364/oe.23.013991.

[101] Aleksandra Foltynowicz, Ticijana Ban, Piotr Masłowski, Florian Adler, and Jun Ye. Quantum-noise-limited optical frequency comb spectroscopy. *Physical review letters*, 107(23):233002, 2011. doi:10.1103/physrevlett.107.233002.

[102] Piotr Maslowski, Kevin F Lee, Alexandra C Johansson, Amir Khodabakhsh, Grzegorz Kowzan, Lucile Rutkowski, Andrew A Mills, Christian Mohr, Jie Jiang, Martin E Fermann, et al. Surpassing the path-limited resolution of fourier-transform spectrometry with frequency combs. *Physical Review A*, 93(2):021802, 2016. doi:10.1103/physreva.93.021802.

[103] Ian Coddington, Nathan Newbury, and William Swann. Dual-comb spectroscopy. *Optica*, 3(4):414–426, 2016. doi:10.1364/optica.3.000414.

[104] Lucile Rutkowski and Jérôme Morville. Continuous vernier filtering of an optical frequency comb for broadband cavity-enhanced molecular spectroscopy. *Journal of Quantitative Spectroscopy and Radiative Transfer*, 187:204–214, 2017. doi:10.1016/j.jqsrt.2016.09.021.

[105] Orazio Svelto and David C Hanna. *Principles of lasers*, volume 4. Springer, 1998. doi:10.1007/978-1-4615-7667-9.

[106] Herwig Kogelnik and Tingye Li. Laser beams and resonators. *Proceedings of the IEEE*, 54(10):1312–1329, 1966. doi:10.1364/ao.5.001550.

[107] Christina J Hood, HJ Kimble, and Jun Ye. Characterization of high-finesse mirrors: Loss, phase shifts, and mode structure in an optical cavity. *Physical Review A*, 64(3):033804, 2001. doi:10.1103/physreva.64.033804.

[108] Daniele Romanini, Irène Ventrillard, Guillaume Méjean, Jérôme Morville, and Erik Kerstel. *Introduction to Cavity Enhanced Absorption Spectroscopy*, pages 1–60. Springer Berlin Heidelberg, Berlin, Heidelberg, 2014. doi:10.1007/978-3-642-40003-2_1.

[109] DA Jackson. The spherical fabry-perot interferometer as an instrument of high resolving power for use with external or with internal atomic beams. In *Proceedings of the Royal Society of London A: Mathematical, Physical and Engineering Sciences*, volume 263, pages 289–308. The Royal Society, 1961. doi:10.1098/rspa.1961.0161.

[110] Dana Z Anderson, Josef C Frisch, and Carl S Masser. Mirror reflectometer based on optical cavity decay time. *Applied optics*, 23(8):1238–1245, 1984. doi:10.1364/ao.23.001238.

[111] Jérôme Morville, Daniele Romanini, Marc Chenevier, and Alexander Kachanov. Effects of laser phase noise on the injection of a high-finesse cavity. *Applied optics*, 41(33):6980–6990, 2002. doi:10.1364/ao.41.006980.

[112] Joshua B Paul, Larry Lapson, and James G Anderson. Ultrasensitive absorption spectroscopy with a high-finesse optical cavity and off-axis alignment. *Applied optics*, 40(27):4904–4910, 2001. doi:10.1364/ao.40.004904.

[113] B Dahmani, L Hollberg, and R Drullinger. Frequency stabilization of semiconductor lasers by resonant optical feedback. *Optics Letters*, 12(11):876–878, 1987. doi:10.1364/ol.12.000876.

[114] J Morville, S Kassi, M Chenevier, and D Romanini. Fast, low-noise, mode-by-mode, cavity-enhanced absorption spectroscopy by diode-laser self-locking. *Applied Physics B: Lasers and Optics*, 80(8):1027–1038, 2005. doi:10.1007/s00340-005-1828-z.

[115] J Morville, D Romanini, AA Kachanov, and M Chenevier. Two schemes for trace detection using cavity ringdown spectroscopy. *Applied Physics B: Lasers and Optics*, 78(3):465–476, 2004. doi:10.1007/s00340-003-1363-8.

[116] P Gorrotxategi-Carbajo, E Fasci, I Ventrillard, M Carras, G Maisons, and D Romanini. Optical-feedback cavity-enhanced absorption spectroscopy with a quantum-cascade laser yields the lowest formalde-

hyde detection limit. *Applied Physics B*, 110(3):309–314, 2013. doi:10.1007/s00340-013-5340-6.

[117] Eric D Black. An introduction to pound–drever–hall laser frequency stabilization. *American Journal of Physics*, 69(1):79–87, 2001. doi:10.1119/1.1286663.

[118] Jun Ye, Long-Sheng Ma, and John L Hall. Ultrasensitive detections in atomic and molecular physics: demonstration in molecular overtone spectroscopy. *JOSA B*, 15(1):6–15, 1998. doi:10.1364/josab.15.000006.

[119] Douglas S Baer, Joshua B Paul, Manish Gupta, and Anthony O'Keefe. Sensitive absorption measurements in the near-infrared region using off-axis integrated-cavity-output spectroscopy. *Applied Physics B: Lasers and Optics*, 75(2):261–265, 2002. doi:10.1117/12.451461.

[120] Yu A Bakhirkin, AA Kosterev, RF Curl, FK Tittel, DA Yarekha, L Hvozdara, M Giovannini, and Jérôme Faist. Sub-ppbv nitric oxide concentration measurements using cw thermoelectrically cooled quantum cascade laser-based integrated cavity output spectroscopy. *Applied Physics B: Lasers and Optics*, 82(1):149–154, 2006. doi:10.1007/s00340-005-2058-0.

[121] J Landsberg, D Romanini, and E Kerstel. Very high finesse optical-feedback cavity-enhanced absorption spectrometer for low concentration water vapor isotope analyses. *Optics letters*, 39(7):1795–1798, 2014. doi:10.1364/ol.39.001795.

[122] V Motto-Ros, M Durand, and J Morville. Extensive characterization of the optical feedback cavity enhanced absorption spectroscopy (of-ceas) technique: ringdown-time calibration of the absorption scale. *Applied Physics B*, 91(1):203–211, 2008. doi:10.1007/s00340-008-2950-5.

[123] DJ Hamilton and AJ Orr-Ewing. A quantum cascade laser-based optical feedback cavity-enhanced absorption spectrometer for the simultaneous measurement of ch 4 and n 2 o in air. *Applied Physics B: Lasers and Optics*, 102(4):879–890, 2011. doi:10.1007/s00340-010-4259-4.

[124] Isak Silander, Thomas Hausmaninger, and Ove Axner. Model for in-coupling of etalons into signal strengths extracted from spectral line shape fitting and methodology for predicting the optimum scanning range—demonstration of doppler-broadened, noise-immune, cavity-enhanced optical heterodyne molecular spectroscopy down to 9× 10-14 cm- 1. *JOSA B*, 32(10):2104–2114, 2015. doi:10.1364/JOSAB.32.002104.

[125] Matthew S Taubman, Tanya L Myers, Bret D Cannon, and Richard M Williams. Stabilization, injection and control of quantum cascade lasers, and their application to chemical sensing in the infrared. *Spectrochimica Acta Part A: Molecular and Biomolecular Spectroscopy*, 60(14):3457–3468, 2004. `doi:10.1016/j.saa.2003.12.057`.

[126] Michael J Thorpe and Jun Ye. Cavity-enhanced direct frequency comb spectroscopy. *Applied Physics B: Lasers and Optics*, 91(3):397–414, 2008. `doi:10.1007/s00340-008-3019-1`.

[127] Birgitta Bernhardt, Akira Ozawa, Patrick Jacquet, Marion Jacquey, Yohei Kobayashi, Thomas Udem, Ronald Holzwarth, Guy Guelachvili, Theodor W Hänsch, and Nathalie Picqué. Cavity-enhanced dual-comb spectroscopy. *Nature Photonics*, 4(1):55–57, 2010. `doi:10.1038/nphoton.2009.217`.

[128] Anthony O'Keefe and David AG Deacon. Cavity ring-down optical spectrometer for absorption measurements using pulsed laser sources. *Review of Scientific Instruments*, 59(12):2544–2551, 1988. `doi:10.1063/1.1139895`.

[129] Kevin K Lehmann and Daniele Romanini. The superposition principle and cavity ring-down spectroscopy. *The Journal of chemical physics*, 105(23):10263–10277, 1996. `doi:10.1063/1.472955`.

[130] D Romanini, AA Kachanov, and F Stoeckel. Cavity ring-down spectroscopy: broad band absolute absorption measurements. *Chemical physics letters*, 270(5-6):546–550, 1997. `doi:10.1016/s0009-2614(97)00407-7`.

[131] Samir Kassi and Alain Campargue. Cavity ring down spectroscopy with 5× 10- 13 cm- 1 sensitivity. *The Journal of chemical physics*, 137(23):234201, 2012. `doi:10.1063/1.4769974`.

[132] S Kassi, D Romanini, A Campargue, and B Bussery-Honvault. Very high sensitivity cw-cavity ring down spectroscopy: Application to the o 2 band near 1.58 μm. *Chemical physics letters*, 409(4):281–287, 2005. `doi:10.1016/j.cplett.2005.05.033`.

[133] BA Paldus, CC Harb, TG Spence, B Wilke, J Xie, JS Harris, and RN Zare. Cavity-locked ring-down spectroscopy. *Journal of Applied Physics*, 83(8):3991–3997, 1998. `doi:10.1063/1.367155`.

[134] TG Spence, CC Harb, BA Paldus, RN Zare, B Willke, and RL Byer. A laser-locked cavity ring-down spectrometer employing an analog detection scheme. *Review of Scientific Instruments*, 71(2):347–353, 2000. `doi:10.1063/1.1150206`.

[135] G-W Truong, Kevin O Douglass, Stephen E Maxwell, Roger D van Zee, David F Plusquellic, Joseph T Hodges, and David A Long. Frequency-agile, rapid scanning spectroscopy. *Nature photonics*, 7(7):532–534, 2013. `doi:10.1038/nphoton.2013.98`.

[136] David A Long, Adam J Fleisher, S Wójtewicz, and Joseph T Hodges. Quantum-noise-limited cavity ring-down spectroscopy. *Applied Physics B*, 115(2):149–153, 2014. `doi:10.1007/s00340-014-5808-z`.

[137] Johannes Burkart, Daniele Romanini, and Samir Kassi. Optical feedback frequency stabilized cavity ring-down spectroscopy. *Optics letters*, 39(16):4695–4698, 2014. `doi:10.1364/ol.39.004695`.

[138] G Giusfredi, S Bartalini, S Borri, P Cancio, I Galli, D Mazzotti, and P De Natale. Saturated-absorption cavity ring-down spectroscopy. *Physical review letters*, 104(11):110801, 2010. `doi:10.1103/PhysRevLett.104.110801`.

[139] Iacopo Galli, Saverio Bartalini, Riccardo Ballerini, Marco Barucci, Pablo Cancio, Marco De Pas, Giovanni Giusfredi, Davide Mazzotti, Naota Akikusa, and Paolo De Natale. Spectroscopic detection of radiocarbon dioxide at parts-per-quadrillion sensitivity. *Optica*, 3(4):385–388, 2016. `doi:10.1364/OPTICA.3.000385`.

[140] Joseph T Hodges, Howard P Layer, William W Miller, and Gregory E Scace. Frequency-stabilized single-mode cavity ring-down apparatus for high-resolution absorption spectroscopy. *Review of Scientific Instruments*, 75(4):849–863, 2004. `doi:10.1063/1.1666984`.

[141] A Cygan, D Lisak, P Masłowski, K Bielska, S Wójtewicz, J Domysławska, RS Trawiński, R Ciuryło, H Abe, and JT Hodges. Pound-drever-hall-locked, frequency-stabilized cavity ring-down spectrometer. *Review of Scientific Instruments*, 82(6):063107, 2011. `doi:10.1063/1.3595680`.

[142] David A Long, Agata Cygan, Roger D van Zee, Mitchio Okumura, CE Miller, D Lisak, and Joseph T Hodges. Frequency-stabilized cavity ring-down spectroscopy. *Chemical Physics Letters*, 536:1–8, 2012. `doi:10.1016/j.cplett.2012.03.035`.

[143] G-W Truong, David A Long, A Cygan, D Lisak, Roger D van Zee, and Joseph T Hodges. Comb-linked, cavity ring-down spectroscopy for measurements of molecular transition frequencies at the khz-level. *The Journal of chemical physics*, 138(9):094201, 2013. `doi:10.1063/1.4792372`.

[144] Davide Gatti, Tommaso Sala, Riccardo Gotti, Lorenzo Cocola, Luca Poletto, Marco Prevedelli, Paolo Laporta, and Marco Marangoni. Comb-locked cavity ring-down spectrometer. *The Journal of chemical physics*, 142(7):074201, 2015. doi:10.1063/1.4907939.

[145] Johannes Burkart, Tommaso Sala, Daniele Romanini, Marco Marangoni, Alain Campargue, and Samir Kassi. Communication: Saturated co2 absorption near 1.6 μ m for kilohertz-accuracy transition frequencies, 2015. doi:10.1063/1.4921557.

[146] Davide Gatti, Riccardo Gotti, Tommaso Sala, Nicola Coluccelli, Michele Belmonte, Marco Prevedelli, Paolo Laporta, and Marco Marangoni. Wide-bandwidth pound–drever–hall locking through a single-sideband modulator. *Optics letters*, 40(22):5176–5179, 2015. doi:10.1364/ol.40.005176.

[147] Ch Salomon, D Hils, and JL Hall. Laser stabilization at the millihertz level. *JOSA B*, 5(8):1576–1587, 1988. doi:10.1364/josab.5.001576.

[148] Adrien Schoof, Jan Grünert, Stephan Ritter, and Andreas Hemmerich. Reducing the linewidth of a diode laser below 30 hz by stabilization to a reference cavity with a finesse above 10 5. *Optics letters*, 26(20):1562–1564, 2001. doi:10.1364/ol.26.001562.

[149] Gianni Di Domenico, Stéphane Schilt, and Pierre Thomann. Simple approach to the relation between laser frequency noise and laser line shape. *Applied optics*, 49(25):4801–4807, 2010. doi:10.1364/AO.49.004801.

[150] Aleksandra Foltynowicz. *Fiber-laser-based noise-immune cavity-enhanced optical heterodyne molecular spectrometry*. PhD thesis, Umeå University, 2009.

[151] Weiguang Ma, Aleksandra Foltynowicz, and Ove Axner. Theoretical description of doppler-broadened noise-immune cavity-enhanced optical heterodyne molecular spectroscopy under optically saturated conditions. *JOSA B*, 25(7):1144–1155, 2008. doi:10.1364/josab.25.001144.

[152] Davide Gatti, Riccardo Gotti, Alessio Gambetta, Michele Belmonte, Gianluca Galzerano, Paolo Laporta, and Marco Marangoni. Comb-locked lamb-dip spectrometer. *Scientific reports*, 6, 2016. doi:10.1038/srep27183.

[153] Mitsuhiro Kusaba and Jes Henningsen. The ν 1+ ν 3 and the ν 1+ ν 2+ ν 4 1+ ν 5- 1 combination bands of 13 c 2 h 2. linestrengths, broadening parameters, and pressure shifts. *Journal of molecular Spectroscopy*, 209(2):216–227, 2001. doi:10.1006/jmsp.2001.8426.

[154] A Czajkowski, AA Madej, and P Dubé. Development and study of a 1.5 μm optical frequency standard referenced to the p (16) saturated absorption line in the (ν 1+ ν 3) overtone band of 13 c 2 h 2. *Optics communications*, 234(1):259–268, 2004. `doi:10.1016/j.optcom.2004.01.026`.

[155] Long-Sheng Ma, Jun Ye, Pierre Dubé, and John L Hall. Ultrasensitive frequency-modulation spectroscopy enhanced by a high-finesse optical cavity: theory and application to overtone transitions of c 2 h 2 and c 2 hd. *JOSA B*, 16(12):2255–2268, 1999. `doi:10.1364/JOSAB.16.002255`.

[156] Riccardo Gotti, Luigi Moretti, Davide Gatti, Antonio Castrillo, Gianluca Galzerano, Paolo Laporta, Livio Gianfrani, and Marco Marangoni. Cavity-ring-down doppler-broadening primary thermometry. *Physical Review A*, 97(1):012512, 2018. `doi:10.1103/physreva.97.012512`.

[157] Riccardo Gotti, Davide Gatti, Piotr Masłowski, Marco Lamperti, Michele Belmonte, Paolo Laporta, and Marco Marangoni. Conjugating precision and acquisition time in a doppler broadening regime by interleaved frequency-agile rapid-scanning cavity ring-down spectroscopy. *The Journal of Chemical Physics*, 147(13):134201, 2017. `doi:10.1063/1.4999056`.

[158] Haifeng Huang and Kevin K Lehmann. Effects of linear birefringence and polarization-dependent loss of supermirrors in cavity ring-down spectroscopy. *Applied optics*, 47(21):3817–3827, 2008. `doi:10.1364/ao.47.003817`.

[159] Johannes Burkart, Tommaso Sala, Samir Kassi, Daniele Romanini, and Marco Marangoni. Optical phase cloning by an integrated dual-parallel mach–zehnder modulator. *Optics letters*, 40(5):816–819, 2015. `doi:10.1364/ol.40.000816`.

[160] Christophe Daussy, Mickael Guinet, Anne Amy-Klein, Khelifa Djerroud, Yves Hermier, Stephan Briaudeau, Ch J Bordé, and Christian Chardonnet. Direct determination of the boltzmann constant by an optical method. *Physical review letters*, 98(25):250801, 2007. `doi:10.1103/physrevlett.98.250801`.

[161] CF Cheng, J Wang, YR Sun, Y Tan, P Kang, and SM Hu. Doppler broadening thermometry based on cavity ring-down spectroscopy. *Metrologia*, 52(5):S385, 2015. `doi:10.15278/isms.2016.te08`.

[162] A Cygan, D Lisak, S Wójtewicz, J Domysławska, Joseph T Hodges, RS Trawiński, and R Ciuryło. High-signal-to-noise-ratio laser technique for accurate measurements of spectral line parameters. *Physical Review A*, 85(2):022508, 2012. `doi:10.1103/physreva.85.022508`.

[163] Pasquale Amodio, Luigi Moretti, Antonio Castrillo, and Livio Gianfrani. Line-narrowing effects in the near-infrared spectrum of water and precision determination of spectroscopic parameters. *The Journal of chemical physics*, 140(4):044310, 2014. `doi:10.1063/1.4862482`.

[164] L Moretti, A Castrillo, E Fasci, MD De Vizia, G Casa, G Galzerano, A Merlone, P Laporta, and L Gianfrani. Determination of the boltzmann constant by means of precision measurements of h 2 o 18 line shapes at 1.39 μ m. *Physical review letters*, 111(6):060803, 2013. `doi:doi.org/10.1103/PhysRevLett.111.060803`.

[165] G Larcher, X Landsheere, M Schwell, and H Tran. Spectral shape parameters of pure co2 transitions near 1.6 μm by tunable diode laser spectroscopy. *Journal of Quantitative Spectroscopy and Radiative Transfer*, 164:82–88, 2015. `doi:10.1016/j.jqsrt.2015.05.013`.

[166] V Malathy Devi, D Chris Benner, LR Brown, CE Miller, and RA Toth. Line mixing and speed dependence in co 2 at 6227.9 cm- 1: constrained multispectrum analysis of intensities and line shapes in the 30013-00001 band. *Journal of Molecular Spectroscopy*, 245(1):52–80, 2007. `doi:10.1016/j.jms.2007.05.015`.

[167] David A Long, S Wójtewicz, Charles E Miller, and Joseph T Hodges. Frequency-agile, rapid scanning cavity ring-down spectroscopy (fars-crds) measurements of the (30012)-(00001) near-infrared carbon dioxide band. *Journal of Quantitative Spectroscopy and Radiative Transfer*, 161:35–40, 2015. `doi:10.1016/j.jqsrt.2015.03.031`.

[168] Norbert Wiener. Generalized harmonic analysis. *Acta Math.*, 55:117–258, 1930. `doi:10.1007/BF02546511`.

[169] Pasquale Maddaloni, Marco Bellini, and Paolo De Natale. *Laser-based measurements for time and frequency domain applications: a handbook*. CRC Press, 2013.

[170] Arthur L Schawlow and Charles H Townes. Infrared and optical masers. *Physical Review*, 112(6):1940, 1958. `doi:10.1103/PhysRev.112.1940`.

[171] Melvin Lax. Classical noise. v. noise in self-sustained oscillators. *Phys. Rev.*, 160:290–307, Aug 1967. `doi:10.1103/PhysRev.160.290`.

[172] David W Allan. Statistics of atomic frequency standards. *Proceedings of the IEEE*, 54(2):221–230, 1966. `doi:10.1109/PROC.1966.4634`.

[173] PO Werle, R Mücke, and F Slemr. The limits of signal averaging in atmospheric trace-gas monitoring by tunable diode-laser absorption spectroscopy (tdlas). *Applied Physics B: Lasers and Optics*, 57(2):131–139, 1993. `doi:10.1007/bf00425997`.

[174] Robert V Pound. Electronic frequency stabilization of microwave oscillators. *Review of Scientific Instruments*, 17(11):490–505, 1946. `doi:10.1063/1.1770414`.

[175] RWP Drever, John L Hall, FV Kowalski, J_ Hough, GM Ford, AJ Munley, and H Ward. Laser phase and frequency stabilization using an optical resonator. *Applied Physics B*, 31(2):97–105, 1983. `doi:10.1007/bf00702605`.